DC Magnetron Sputter Deposition of Molybdenum Oxide Thin Films from Metallic Mo and Ceramic MoO$_x$ Targets: Synthesis, Structure and Property Relations

Dipl.-Ing. Julia Pachlhofer

Being a thesis in partial fulfilment of the requirements for the degree of a
Doktor der montanistischen Wissenschaften (Dr. mont.)
at the Montanuniversität Leoben.

Chair of Functional Materials and Materials Systems
Department of Physical Metallurgy and Materials Testing
Montanuniversität Leoben, 8700 Leoben, Austria
Leoben, 2016

This work has been supported by The Austrian Industrial Research Promotion Fund (FFG) within the FFG Competence Headquarters project E^{2}SPUTTERTECH.

Affidavit

I declare in lieu of oath that I wrote this thesis and performed the associated research myself, using only literature cited in this volume.

Date	Signature

Acknowledgements

I would like to express my sincere gratitude to Christian Mitterer for providing me with the opportunity to write this thesis at the Chair of Functional Materials and Materials Systems, for his supervision, the patience and the confidence he placed in me.

An equally big thank you is due to my co-supervisor Robert Franz, who always took the time to listen, discuss and show the path forward.

Many thanks go to my past and present colleagues in the Thin Film Group for the great support, interesting discussions as well as chatty coffee breaks and the pleasurable working atmosphere.

I would like to thank our office ladies - Hilde, Angelika, Eva-Maria and Regina - for helping with all bureaucratic stuff all the time.

Many thanks go to my partners in industry (PLANSEE SE, Reutte), Jörg Winkler, Enrico Franzke, Harald Köstenbauer, and Christian Linke, for their valuable contributions to my research. Additionally, I would like to thank Michaela Zabernig for dealing with my often challenging SEM samples, Dominik Lorenz for helping with optical measurements, and Jürgen Knittl and Thomas Leiter for great support manufacturing my sputter targets. Although I was not a permanent member of your working group, I felt very welcome every time I visited you and thank you for the insight that with enough sweets and coffee anything can be handled :-)

I am also grateful to my project partners from JKU Linz, Aitana Tarazaga Martín-Luengo, Alberta Bonanni and Reinhold Koch. It was a pleasure to do research with you. Thank you Aitana for the patience with my XPS and resistivity samples.

I would like to thank my student workers Lisa and Juliane as well as my diploma student Christoph for their contributions to my thesis.

A special thanks goes to all my friends I found in Leoben for the great times we had, have and hopefully will have in future, especially to Tamara, Leni, Marion, Sabrina and Christoph, who always have a sympathetic ear for me and on whom I can rely on.

Last but not least … möchte ich mich besonders bei meiner Familie bedanken. Ohne eure Unterstützung in jeglicher Art und Weise in den letzten Jahren wäre diese Arbeit nicht möglich gewesen. Danke, dass ihr mir immer die Möglichkeit gegeben habt, meinen Weg zu gehen und dass ihr mir immer ein sicherer Hafen seid.

Abstract

Due to their unique optical, electrical and chemical properties, oxide-based thin film materials are widely used in industrial applications ranging from hard coatings via diffusion barriers to thin films for opto-electronic applications. With changes in stoichiometry or by alloying or doping the base materials, it is possible to tune the material properties to the desired level. In the current work, the microstructure-property relationships in correlation with synthesis conditions of molybdenum oxide thin films deposited by dc magnetron sputter deposition were investigated. On the one hand, molybdenum oxide films were synthesised reactively in varying oxygen/argon atmosphere in a laboratory-scale deposition system (equipped with circular planar Mo targets) as well as in an industrial-scale deposition plant (equipped with a rotatable Mo target). The character of the films varied between non-transparent electrical conductive and transparent insulating, depending on the used oxygen partial pressure during deposition. On the other hand, molybdenum oxide films were synthesised by non-reactive dc magnetron sputter deposition from circular planar ceramic molybdenum oxide targets developed by powder-metallurgical methods within this work with compositions ranging from $MoO_{2.5}$ to $MoO_{2.8}$ as an alternative synthesis process. These films exhibited a high optical absorbance and low reflectance character with a semi-conductive behaviour. All synthesised films were dominated by Mo^{4+} (MoO_2), an intermediate oxidation state Mo^{5+}, and Mo^{6+} (MoO_3) depending on the synthesis conditions. In general, a successful upscaling for reactively sputtered molybdenum oxide films with tuneable properties depending on the used oxygen partial pressure during deposition from laboratory- to industrial-scale could be demonstrated. Moreover, the use of oxide targets in dc magnetron sputter deposition of molybdenum oxide films offers an efficient and reliable alternative to the use of metal targets and, hence, enables the usage of such films for a wide range of optical and electrical applications.

Table of Contents

1 INTRODUCTION 1

2 THE MOLYBDENUM-OXYGEN SYSTEM 3

3 SINTERING 9

3.1 Fundamentals of Sintering 9

3.2 Hot Pressing 11

3.3 Spark Plasma Sintering 12

3.3.1 Fundamentals of Spark Plasma Sintering 12

3.3.2 Synthesis of MoO_x Targets by SPS 13

4 THIN FILM FORMATION 18

4.1 Magnetron Sputter Deposition 18

4.2 Reactive Sputter Deposition 21

4.3 Thin Film Nucleation and Growth 22

5 THERMAL STABILITY OF MoO_2 AND MoO_3 POWDERS 27

5.1 Introduction 27

5.2 Experimental details 30

5.3 Results and Discussion 31

5.3.1 Virgin powders 31

5.3.2 Thermal stability 34

5.3.3 Heat-treated powders 36

5.4 Conclusions 39

6 STRUCTURE EVOLUTION IN REACTIVELY SPUTTERED MOLYBDENUM OXIDE THIN FILMS 40

6.1 Introduction 40

6.2 Experimental methods 41

6.3 Results 43

6.4 Discussion 48

6.5 Conclusions 49

7 INDUSTRIAL-SCALE SPUTTER DEPOSITION OF MOLYBDENUM OXIDE THIN FILMS: MICROSTRUCTURE EVOLUTION AND PROPERTIES 51

7.1 Introduction 51

7.2 Experimental details 52

7.3 Results 54

7.4 Discussion 61

7.5 Conclusions 64

8 NON-REACTIVE DC MAGNETRON SPUTTER DEPOSITION OF MoO_x THIN FILMS FROM CERAMIC MOLYBDENUM OXIDE TARGETS 65

8.1 Introduction 65

8.2 Experimental Details 66

8.3 Results and Discussion 68

8.4 Conclusions 75

9 SUMMARY AND CONCLUSIONS 76

9.1 Reactive dc magnetron sputter deposition 76

9.2 Non-reactive dc magnetron sputter deposition 77

9.3 Outlook 77

10 REFERENCES 79

11 LIST OF PUBLICATIONS 88

ABBREVIATIONS

Al	…	*Aluminium*
Al_2O_3	…	*Aluminium Oxide*
Ar	…	*Argon*
AZO	…	*Aluminium doped Zinc Oxide*
dc	…	*Direct Current*
FAST	…	*Field-Assisted Sintering Technique*
HP	…	*Hot Pressing*
ITO	…	*Tin doped Indium Oxide*
Mo	…	*Molybdenum*
MoO_2	…	*Molybdenum Dioxide*
MoO_3	…	*Molybdenum Trioxide*
MoO_x	…	*Molybdenum Oxide*
MSD	…	*Magnetron Sputter Deposition*
N_2	…	*Nitrogen*
O, O_2	…	*Oxygen*
$p(O_2)$	…	*Oxygen Partial Pressure*
PVD	…	*Physical Vapour Deposition*
SPS	…	*Spark Plasma Sintering*
SZM	…	*Structure Zone Model*
TCO	…	*Transparent Conductive Oxide*
T_m	…	*Melting Temperature*
T_s	…	*Substrate Temperature*

1 INTRODUCTION

The field of opto-electronics as used for solar cells, electrochromic glasses, and displays has experienced a considerable boom in recent years. As electronic displays find their way into our everyday life, special applications become smaller and smaller and their structure therefore more and more sophisticated. Attuned properties like excellent electrical conductivity and high optical transparency are needed for example in electrode materials for flat-panel displays. Nowadays, such aligned properties are realised by a certain group of metal oxides [1], the so-called transparent conductive oxides (TCO). The best known TCO materials are aluminium doped zinc oxide (AZO) [2,3] and tin doped indium oxide (ITO[1]) [4]. In particular, ITO has proved to be successful in industry but its major drawback is the high world market price due to its limited availability. Moreover, to keep up with the rapid developments in the high-tech sector, material systems need to be easily adaptable to changing technological needs.

The properties of oxides can often be tuned by alloying or doping the base materials or by changing their stoichiometry. This work focuses on the binary Mo-O system as an alternative material system to ITO. Properties of molybdenum oxides (MoO_x) strongly depend on their oxidation state. MoO_x phases are known to have broad-ranging optical and electrical properties, which are extending from the lowest oxidation state (MoO_2; Mo^{4+}) with non-transparent appearance and metallic-like electrical conductivity, to the highest oxidation state (MoO_3; Mo^{6+}) with transparent appearance and electrically insulating behaviour. Additionally, several MoO_x like Magnéli phases between the stable oxides MoO_2 and MoO_3 with varying optical and electrical properties were reported [5-8]. In particular, MoO_3 thin films have already proved to be successful in industrial applications like electrochromic [9] and photochromic glasses [9-10], gas sensors [11], and photovoltaics [12]. In contrast, the field of possible industrial applications for lower oxidised MoO_x remains largely unexplored up to now [13-16].

Several different deposition techniques are available to synthesise such material systems, e.g. printing [17], sol-gel [18-20], chemical vapour deposition [18,21,22], and physical vapour deposition techniques, especially magnetron sputter deposition (MSD) [18,23,24]. A common

---

[1] Although in literature often the denomination indium-doped tin oxide is used, it should be stated here that ITO is in fact a tin-doped indium oxide.

MSD process for synthesising oxide thin films is reactive sputtering, in which a reactive gas (e.g. O_2) is added to the working gas during deposition [25]. Varying the partial pressure of this reactive gas leads to varying stoichiometry of the synthesised films and as a consequence to versatile and tuneable properties [26]. The growth of the films is based on the formation of chemical compounds between the adsorbed reactive gas molecules on the substrate and the impinging target atoms. Coincidentally, compounds will be formed on the target surface. These compounds of lower conductivity affect the sputter behaviour towards lower sputter and deposition rates and is called target poisoning [27].

Typically MoO_x films are synthesised by reactive sputtering from a Mo target in O_2/Ar atmosphere. *Section 6 and 7* deal with the microstructural evolution, structure-property relationships, and versatile optical and electrical properties depending on varying oxygen partial pressure used during deposition. Reactive sputtering needs an accurate process control to achieve homogeneous film properties, which requires sophisticated and expensive process control. Consequently, *Section 5 and 8* deal with the development of MoO_x targets and the synthesis of MoO_x films from these targets in a non-reactive process as an alternative to fully reactive sputter processes with Mo targets.

2 THE MOLYBDENUM-OXYGEN SYSTEM

In literature, an experimentally derived phase diagram by *Chang and Phillips* (Figure 2.1) [28] as well as a calculated one by *Zhang et al.* (Figure 2.2) [29] are available for the binary system Mo-O. The phase diagrams show two thermodynamically stable oxides: molybdenum dioxide (MoO_2) and molybdenum trioxide (MoO_3). While the phase boundaries in both diagrams are in good agreement, the calculated phase diagram covers an extended temperature region from 200 up to 2700 °C. A eutectic point between Mo and MoO_2 is shown at 2200 °C. The eutectic composition reported in literature differs between 23 at.% O (experimentally derived by *Okamoto* [30]) and 15 at.% O (calculated by *Zhang et al.* [29]). *Chang and Phillips* [28] predicted a two-liquid region between Mo and MoO_2 at temperatures above 2200 °C.

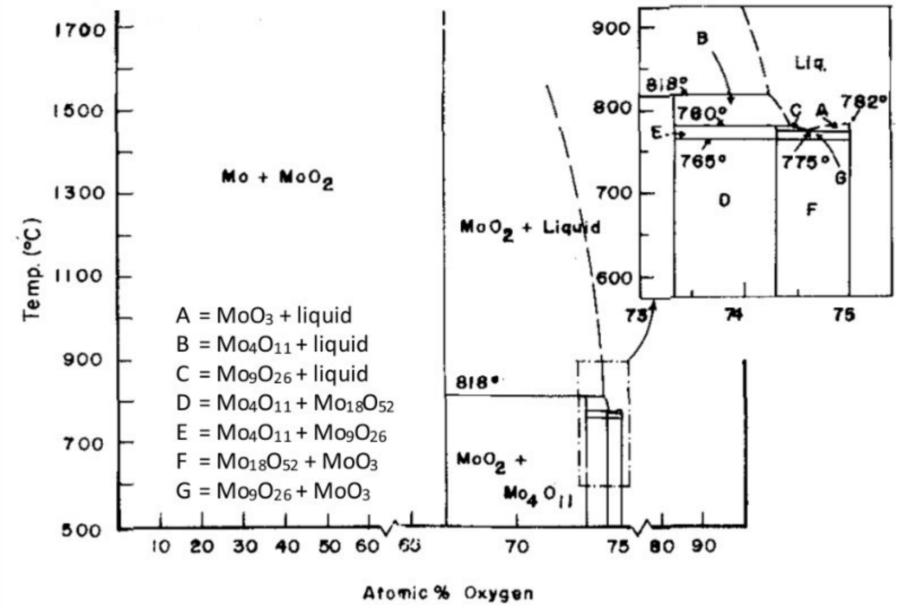

Figure 2.1: Experimentally derived phase diagram of the binary Mo-O system by *Chang and Phillips* [28].

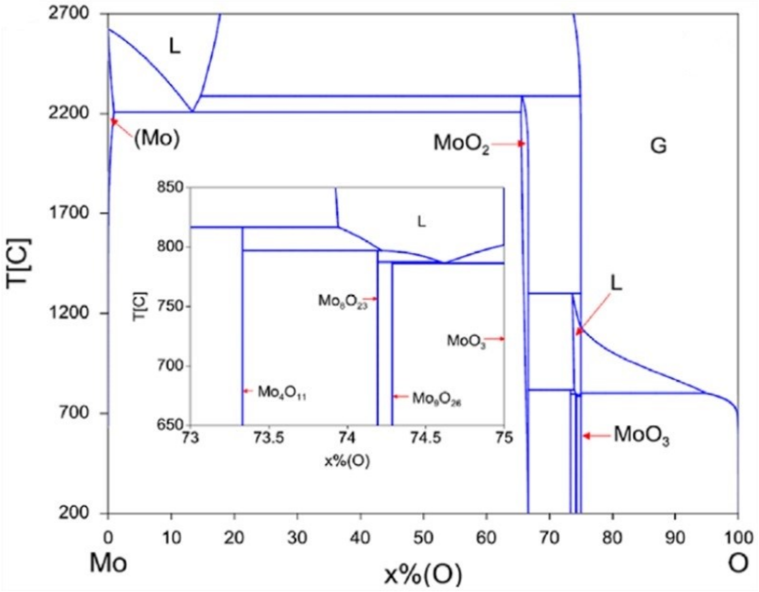

Figure 2.2: Calculated phase diagram of the binary Mo-O system by *Zhang et al.* [29].

According to the phase diagrams shown in Figure 2.1 and Figure 2.2, no oxide phase exists between Mo and MoO_2. However, *Schönberg* reported the observation of Mo_3O [31], but its existence is disputed. It could not be prepared in a pure state [31] and it could not be synthesised by other researchers [28]. Therefore, MoO_2 with an oxygen content of 66.7 at.% represents the lowest Mo oxidation state (Mo^{4+}) of all molybdenum oxides (MoO_x). Its monoclinic crystal structure [8,32,33] is based on a deformed rutile lattice consisting of MoO_6 octahedra sharing edges and corners (Figure 2.3).

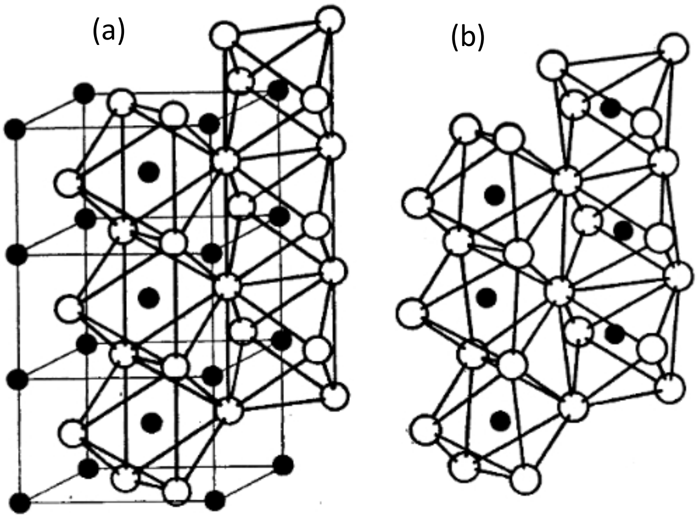

Figure 2.3: Schematic representation of a) the ideal rutile structure and b) the MoO_2 structure [33].

The Mo atoms form direct metal-metal bonds in alternating metal-metal doublets [8,32], which causes the distortion of the crystal. Furthermore, this chemical bond structure leads to the metal-like electrical conductivity of MoO_2 with a resistivity of about 10^{-4} to 10^{-5} Ωcm [8], which is similar to metallic Mo as shown in Table 2.1. MoO_2 has a non-transparent reddish-brown to reddish-purple appearance [5,7].

The MoO_x with the highest Mo oxidation state MoO_3 (Mo^{6+}) exists in two modifications: orthorhombic α-MoO_3 and monoclinic β-MoO_3 [34], where the former is the thermodynamically stable one [34]. Analogously to MoO_2, the thermodynamically stable α-MoO_3 consists of heavily distorted MoO_6 octahedra [5,35], the sole difference being that they form a layered two-level structure (Figure 2.4). These layers are connected by shared octahedral edges and form zig-zag rows in [001] direction [5,35].

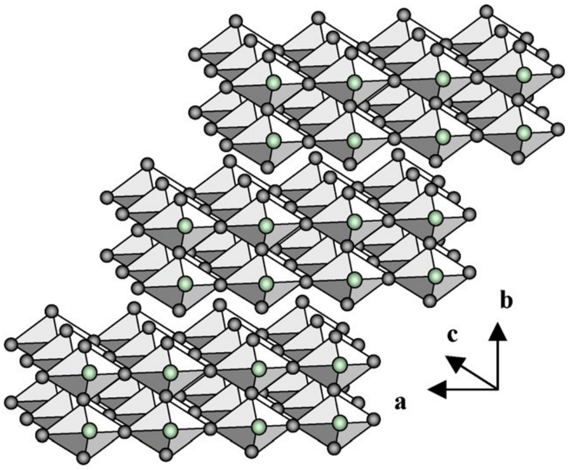

Figure 2.4: Schematic representation of the layered structure of α-MoO_3 [36].

All metal-oxygen bonding orbitals are filled and the energy states in the metal d-conduction band remain empty resulting in a diamagnetic insulating behaviour [37]. The visual appearance of both modifications is transparent with a slight yellowish tinge [32,37].

Beside the thermodynamically stable oxides MoO_2 and MoO_3, several intermediate oxidation states, referred to as Magnéli phases, are reported in literature. *Magnéli* first described their existence in 1953 [33] and further investigations were done by *Kihlborg* in 1959 [6]. Selected properties of the different MoO_x phases are listed in Table 2.1.

Table 2.1: Selected properties of the different MoO_x phases [6,8,38,39, *Section 5*]. Metallic Mo is included as a reference. (m…metallic, sc…semiconducting, in…insulating)

Oxide		**Crystal structure**	**$T_{Formation}$ [°C]**	**Density [g/cm³]**	**Resistivity [Ωcm]**
Mo		*cubic*		*10.22*	*$5.03 \cdot 10^{-6}$ (m)*
MoO_2		monoclinic		6.47	$8.8 \cdot 10^{-5}$ (m)
Mo_4O_{11}	η-oxide	monoclinic	< 615	4.14	10^{-5} to 0.2 (m)
	γ-oxide	orthorhombic	> 615	4.18	0.25 (sc)
$Mo_{17}O_{47}$	κ-oxide	orthorhombic	< 560	4.72	< 0.05 (m → sc)
Mo_5O_{14}	θ-oxide	tetragonal	470 – 530		
Mo_8O_{23}	β-oxide	monoclinic	650 – 780	4.32	1.2 (sc)
Mo_9O_{26}	ζ-oxide	triclinic	600 – 750	4.74	250 (sc)
	β'-oxide	monoclinic	750 – 780	4.26	3.7 (sc)
MoO_3	α-MoO_3	orthorhombic		4.69	$1.7 \cdot 10^{9}$ (in)
	β-MoO_3	monoclinic			10^{10} (in)

The Magnéli phase oxides are defined as oxygen-deficient oxides, e.g. Mo_nO_{3n-1} [33] and therefore only exist at an exact oxygen content, whereas MoO_2 and MoO_3 have narrow homogeneity regions of $MoO_{1.9-2.08}$ and $MoO_{2.95-3.0}$ [40], respectively. With increasing oxygen content, the following Magnéli phases are present in the binary Mo-O system: Mo_4O_{11} (two polymorphs), $Mo_{17}O_{47}$, Mo_5O_{14}, Mo_8O_{23} and Mo_9O_{26} (two polymorphs) [6]. Their thermal stability regions are illustrated in Figure 2.5. Mo_5O_{14} seems to be a metastable phase [41].

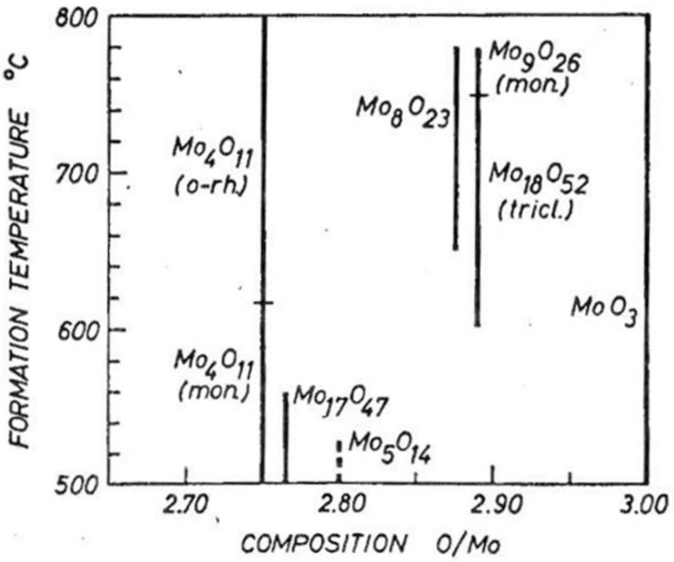

Figure 2.5: Formation diagram of the molybdenum oxides (except MoO_2) [5].

Mo_4O_{11} and Mo_9O_{26} exist in two modifications depending on the ambient temperature [6]. The transformation of Mo_4O_{11} from the monoclinic η-polymorph to the orthorhombic γ-polymorph and vice versa takes place between 550 and 655 °C [6]. The change from triclinic Mo_9O_{26} (ζ-oxide) to monoclinic Mo_9O_{26} (β'-oxide) occurs between 760 and 780 °C [6]. The transformation temperature, decomposition temperature as well as reaction equations are listed in Table 2.2.

Table 2.2: Thermal stability of Magnéli phase molybdenum oxides [6,38, *Section 5*].

Oxide	Transformation temperature [°C]	Decomposition temperature [°C]	Reaction equation
Mo_4O_{11}	550 - 655		$\eta\text{-}Mo_4O_{11} \leftrightarrow \gamma\text{-}Mo_4O_{11}$
		815 - 820	$\gamma\text{-}Mo_4O_{11} \rightarrow MoO_2 + 3\ MoO_3$ (gas.)
$Mo_{17}O_{47}$		630	$Mo_{17}O_{47} \rightarrow \gamma\text{-}Mo_4O_{11} + Mo_8O_{23}$
Mo_5O_{14}		530	$Mo_5O_{14} \rightarrow Mo_{17}O_{47} + MoO_3$
Mo_8O_{23}		785	$Mo_8O_{23} \rightarrow \gamma\text{-}Mo_4O_{11} + MoO_3$
$\zeta\text{-}Mo_9O_{26}$	760 - 780		$\zeta\text{-}Mo_9O_{26} \rightarrow \beta'\text{-}Mo_9O_{26}$
		550	$\zeta\text{-}Mo_9O_{26} \rightarrow \eta\text{-}Mo_4O_{11} + MoO_3$
$\beta'\text{-}Mo_9O_{26}$		785 - 800	$\beta'\text{-}Mo_9O_{26} \rightarrow \gamma\text{-}Mo_4O_{11} + MoO_3$

Further details about structure and properties of all the different MoO_x phases can be found in chemistry handbooks, e.g. by *Gmelin* [42].

In *Section 5* of this work, different MoO_x powders were investigated with a focus on the thermal stability of different MoO_x phases in order to evaluate their suitability for the production of sputter targets and to determine possible process parameter ranges. Two powders of each oxide, MoO_2 and MoO_3, were analysed with respect to their phase purity and its effect on thermal stability and sintering behaviour.

3 SINTERING

3.1 Fundamentals of Sintering

Sintering is defined as a process where a solid mass of material is compacted and formed by heat and/or pressure with shrinkage of the densified body and without reaching the melting point of the main component of sintering material. By the choice of material-dependent parameters like chemical composition, particle size, shape and distribution as well as agglomeration grade, many properties of the sintered body can be controlled. Furthermore, process parameters like temperature, time, atmosphere, pressure, and heating and cooling rates are crucial for the properties and quality of the component to be sintered.

The driving force for densification of the solid is the reduction of surface area, which is equivalent to the reduction of surface free energy. Figure 3.1 schematically shows three spherical crystalline particles in contact with possible diffusion paths [43]. The non-densifying mechanisms 1, 2, and 3 describe microstructural changes causing neck growth between the particles but no shrinkage. Path 1 describes surface diffusion, path 2 lattice bulk diffusion from the surface and path 3 vapour transport due to vaporisation of material at the surface and subsequent condensation at the neck. The densifying mechanisms 4, 5, and 6 illustrate the removal of material from the grain boundary region causing the particle centres to approach one another. These mechanisms consequently lead to shrinkage. Path 4 describes grain boundary diffusion, path 5 lattice bulk diffusion from the grain boundary and path 6 describes plastic flow by dislocation motion. During sintering all mechanisms are active at the same time. Depending on temperature, particle size, sintering atmosphere, agglomeration, etc., the process with the highest rate is dominant.

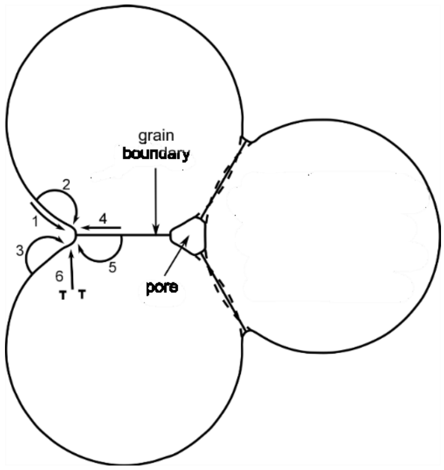

Figure 3.1: Schematic illustration of the six possible paths for material transport: (1) surface diffusion, (2) lattice bulk diffusion (from the surface), (3) vapour transport, (4) grain boundary diffusion, (5) lattice bulk diffusion (from grain boundary), and (6) plastic flow (modified from [43]).

The sintering process itself can be categorised into three stages based on the changes in pore size and shape and material transport due to diffusion [44]. The initial stage is dominated by neck growth and a few percent of shrinkage (Figure 3.2a). The intermediate stage is characterised by forming continuous pore channels along three-grain edges (Figure 3.2b). The main densification happens in this intermediate stage. The final stage begins when the pore phase situated at the three-grain edges starts to pinch off and forms individual pores at triple points (Figure 3.2c). Its character is shaped by grain coarsening at the expense of pores and smaller grains and by grain growth due to grain boundary diffusion.

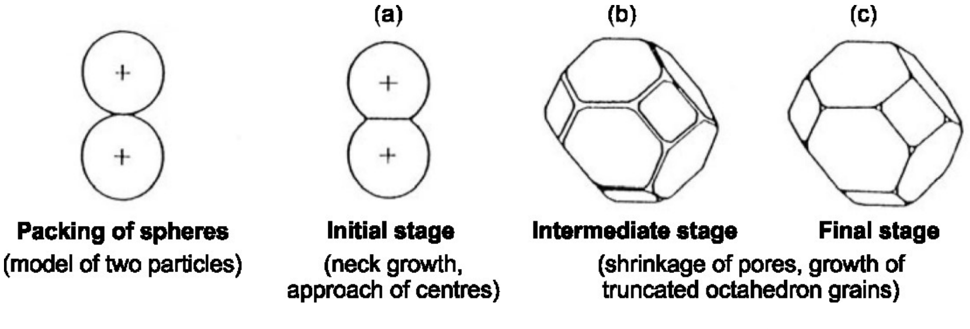

Figure 3.2: Sinter stages and evolution of the pore size and shape (modified from [45]).

Based on the combination of temperature, pressure and time, the sintering process can be adjusted to obtain dense sintered bodies with desired grain size and properties.

3.2 Hot Pressing

Hot pressing (HP) is a powder metallurgical process to compact material by the simultaneous application of heat and pressure. In this work, the expression HP is used for the conventional hot pressing process using inductive heating (Figure 3.3). The sinter material is placed in a steel or graphite die and pressure is applied by one or two punches. The die is positioned within an induction coil, which generates the heat. Pressure and inductive power are independent. A good thermal conductivity of the die is important. Most of the heat has to be transported into the die by thermal conductivity and therefore uniform heating is difficult. Furthermore, very high heating rates are problematic because they result in high temperature differences between the surface and core of the sinter body, which can lead to a disintegration of the die due to excessive thermal stresses.

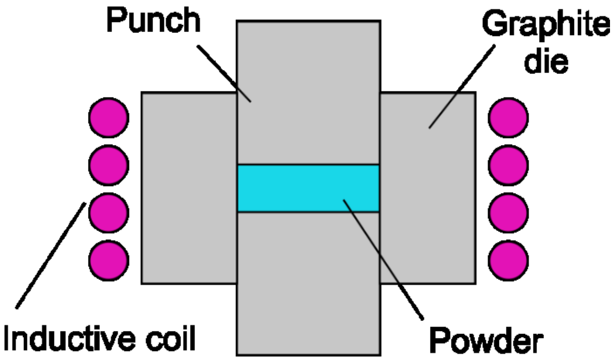

Figure 3.3: Schematic of a hot pressing apparatus.

For full densification, typically a process duration of a few hours is needed, which can raise the manufacturing costs significantly. To reduce costs, several alternative powder metallurgical processes are available allowing shorter process times and lower temperatures. One of these processes is spark plasma sintering, which is described in section 3.3 and was used for the development of sputter targets within this work.

3.3 Spark Plasma Sintering

3.3.1 Fundamentals of Spark Plasma Sintering

Spark plasma sintering (SPS[2]), also known as field-assisted sintering technique (FAST), is characterised by low voltages, high currents, high heating rates and the use of uniaxial pressure [46–50]. SPS is similar to hot pressing but heat generation and transport to the sintering material are different. Figure 3.4 illustrates a schematic of an SPS apparatus. The process is typically controlled by temperature measurement using either thermocouples or pyrometers. The good electrical conductivity of the used die material (usually graphite) enables the application of low voltages (usually below 10 V) and high currents (usually up to 10 kA), which results in efficient Joule heating. The compact apparatus geometry allows heating rates of up to 1000 °C/min and cooling rates in the range of 150 °C/min [51,52]. Reaching high sintering temperatures very fast can enhance the densification rate, while coarsening mechanisms will be retarded. Further densification is improved by the simultaneous application of uniaxial mechanical pressure.

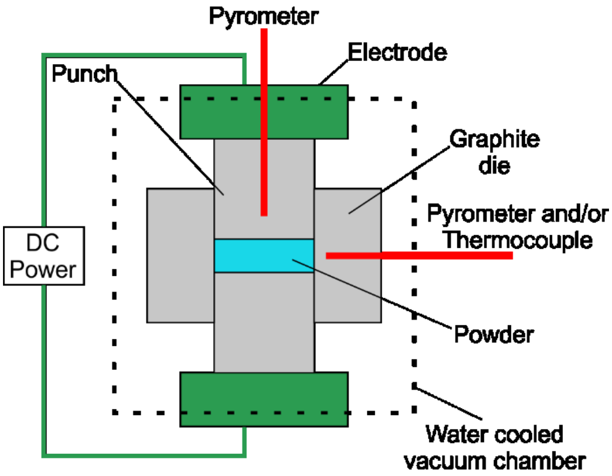

Figure 3.4: Schematic of an SPS apparatus.

The tool material and the sample material itself determine whether the sample or the die is heated (Figure 3.5) [53]. In the case of electrically conductive sinter material, the dc current directly passes through the sample and the die (Figure 3.5a). The usage of an electrically

---

[2] Although the term spark plasma sintering is commonly used, the term is misleading since neither a spark nor a plasma is present in the process.

insulating die forces the current to go through the sintering material and therefore the highest possible current density can be achieved (Figure 3.5b). It is also possible to sinter non-conductive materials. Then the process behaves like a rapid HP cycle (Figure 3.5c) [54,55].

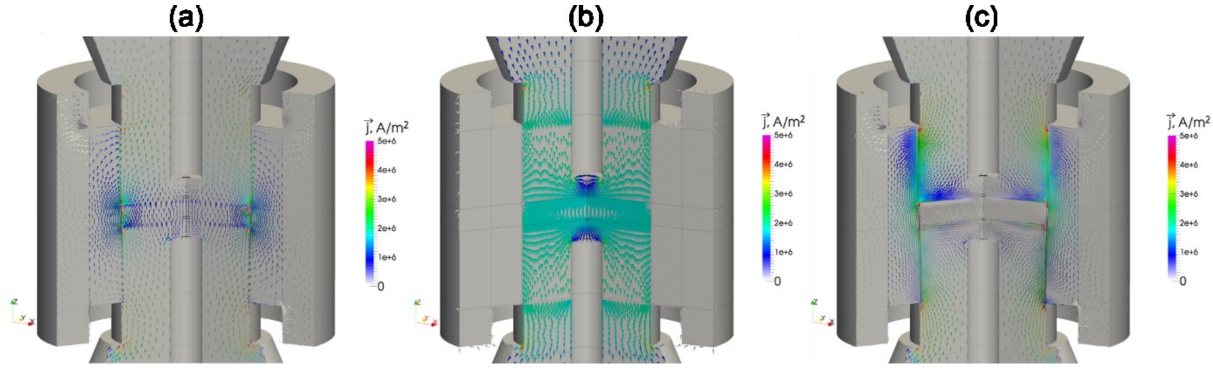

Figure 3.5: Finite element simulation showing the flow of the electric current depending on different sinter and die materials: a) conducive powder and die, b) conductive powder, insulating die, and c) non-conductive powder, conductive die [53].

A detailed review about SPS and possible influencing factors and occurring mechanisms has been published by *Guillon et al.* [53].

3.3.2 Synthesis of MoO_x Targets by SPS

The sintering materials used in this work for the development of sputter targets were mixtures of electrically conductive MoO_2 and insulating MoO_3 powders. The current path and temperature evolution in this compound material can be explained by Figure 3.5. When the composite powder starts to sinter, the current flows through the graphite die similar to a HP process (Figure 3.5c). Once first electrical paths are constructed, the current starts to flow through the sintering material (Figure 3.5a). At this point, the subsequent process route depends on whether the compound powder fully reacts to a homogenous single-phase material. In this case, the process is assumed to proceed as illustrated in Figure 3.5b (conductive powder and insulating die). In contrast, if the compact powder does not fully react to a single-phase material, then local hot spots can be formed within the percolating current paths characterised by high local current densities and over-heating [50]. The temperature within these hot spots can exceed the average process temperature significantly, which can lead to local reaction zones [56]. Such reaction zones for MoO_x, where different sub-oxides are formed, are shown in Figure 3.6.

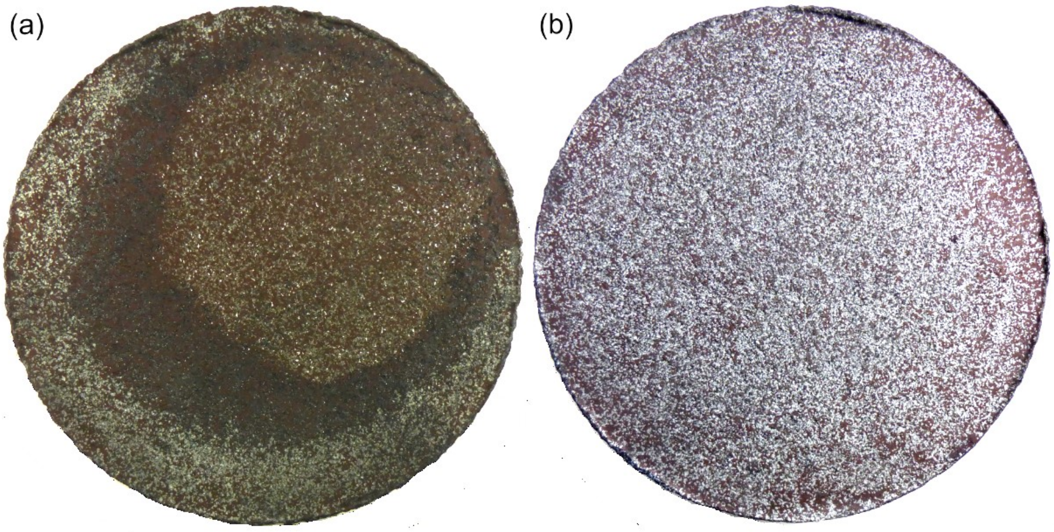

Figure 3.6: Photograph of sintered MoO_x targets (∅ 100 mm) with a) reaction zones due to hot spots and b) without reaction zones [own work].

These hot spots and accordingly such reaction zones are difficult to control due to numerous influencing factors like different powder parameters (particle size, distribution, agglomeration) as well as process parameters (heating rate, time, maximum temperature). This is exemplified by two experiments with the same powder mixture and the same process parameters yielding two different results, one target with visible reaction zones and one without (Figure 3.6). The appearance of hot spots and resulting discontinuities can also be noticed in the data sets of the sinter curves in Figure 3.7, where sinter curves with and without hot spots are compared. Such hot spots appear as fluctuations of temperature and current signal in Figure 3.7a, while they are not visible when no hot spots are present (Figure 3.7b).

(a) Sinter curve with "hot spots"

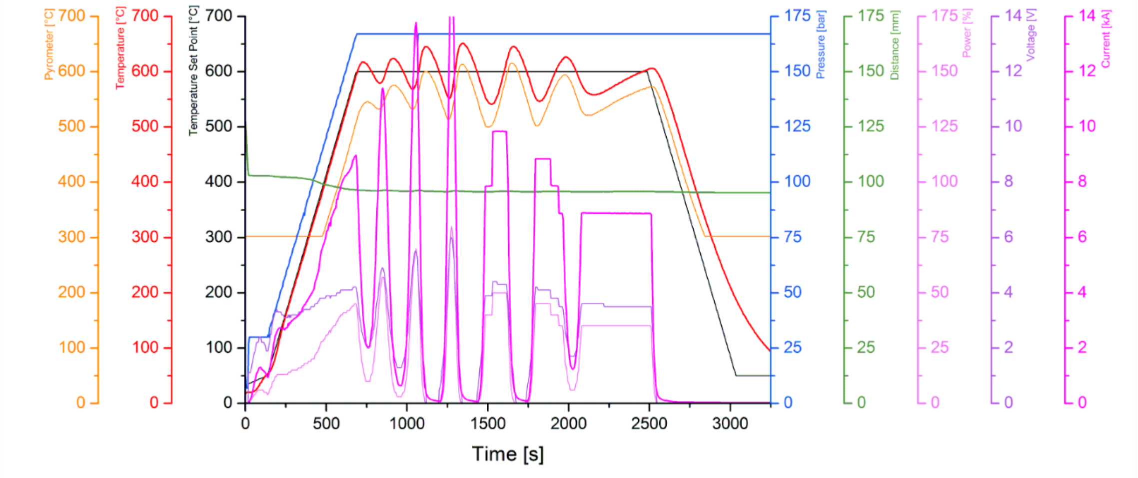

(b) Sinter curve without "hot spots"

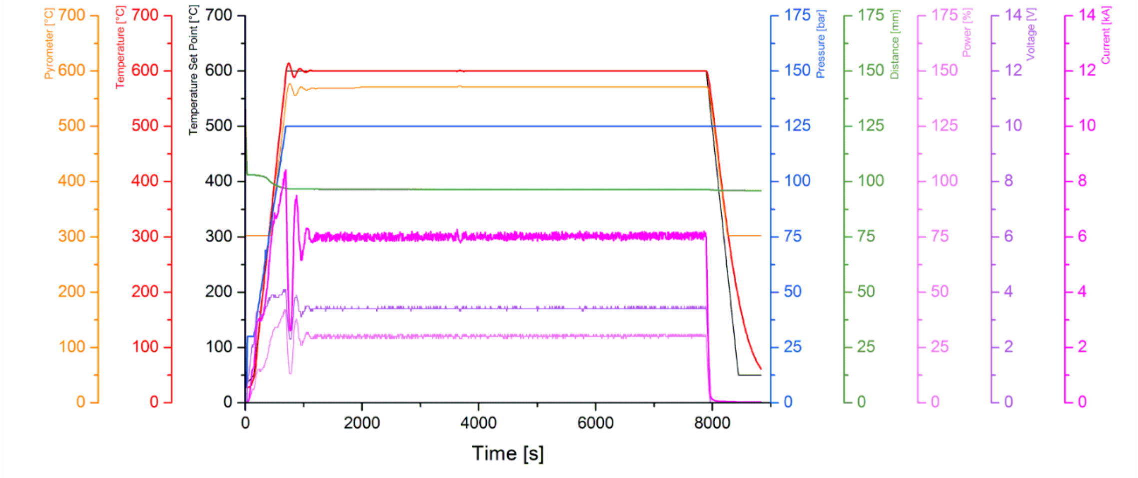

Figure 3.7: Typical sinter parameters recorded during manufacturing of the targets shown in Figure 3.6 including the process parameters temperature, pressure, punch distance, voltage and current of processes a) with hot spots and b) without hot spots.

Such sinter curves also provide information about the state of the densification process by evaluating the recorded punch distance. If the distance curve still decreases at the end of the time, the sinter body has not reached the theoretical density yet. Another special feature observed beside the hot spots and resulting reaction zones was that single-phase MoO_2 powder was not densified by either of the used processes, HP or SPS. According to the patent of *McHugh et al.* [57], a sinter active phase is needed in a small amount to enhance the densification process, which in this work is realised by a dual-phase MoO_2 powder consisting of MoO_2 and small amounts of Mo_4O_{11}. Figure 3.8a shows a sintered but not densified single-phase MoO_2 target, whereas Figure 3.8b represents a fully densified dual-phase MoO_2 target with a relative density of ~85%. The same sinter parameters were used for both targets.

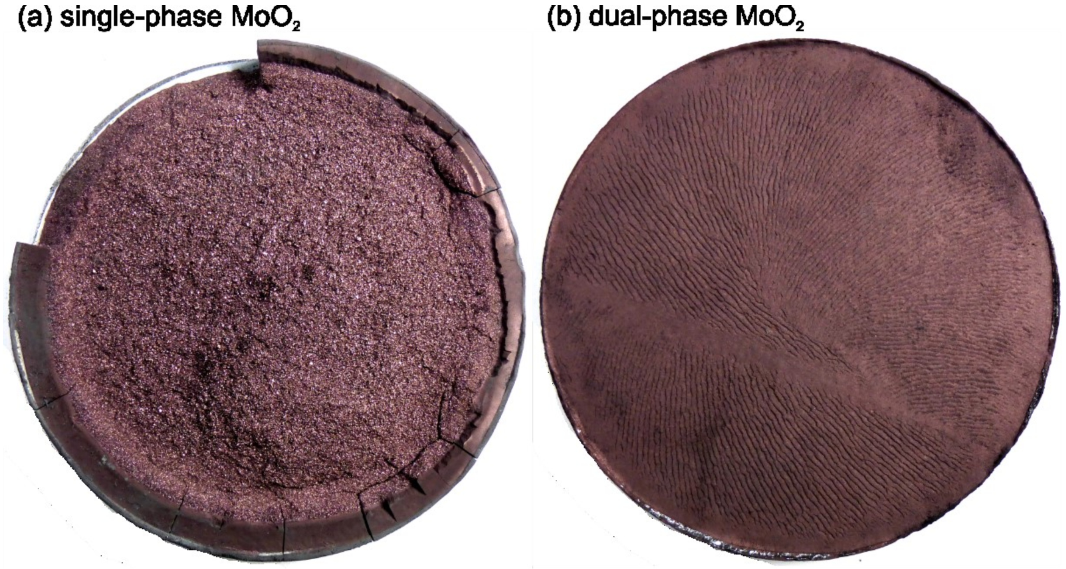

Figure 3.8: Photograph of sintered MoO_2 targets (∅ 100 mm): a) not compacted single-phase MoO_2 powder and b) compacted dual-phase MoO_2 powder [own work].

Within this work several different powder mixtures were used for the development of MoO_x targets as documented in Table 3. According to the patent of *McHugh et al.* the relative density of the MoO_x targets increases by ~10% with increasing content of MoO_3 powder within the mixture [57]. Subsequently, the flexural strength R_{bb} decreases significantly with increasing content of MoO_3 powder within the mixture.

Table 3.1: Different MoO_x mixtures developed and sintered within this work.

MoO_x	**MoO_2**	**MoO_3**	**theo. Density**	**Bending Test**	
				F_{max}	**R_{bb}**
	[wt.%]	[wt.%]	[%]	[N]	[MPa]
MoO_2	100	0	87	630	70
$MoO_{2.5}$	50	50	87	315	36
$MoO_{2.6}$	40	60	86	225	24
$MoO_{2.7}$	30	70	88	165	18
$MoO_{2.8}$	20	80	90	118	13
$MoO_{2.9}$	10	90	92	113	13
MoO_3	0	100	94	123	14

While *Section 5* provides a detailed overview of the properties of the MoO_x powders used for sintering, *Section 8* reports on sputter tests using the MoO_x targets summarised in Table 3.1 and their possible usage to synthesise MoO_x thin films as an alternative to fully reactive sputter deposition processes using Mo targets.

4 THIN FILM FORMATION

4.1 Magnetron Sputter Deposition

Magnetron sputter deposition (MSD) is a technique within the versatile family of physical vapour deposition (PVD) methods. The transfer of the solid target material into a gaseous phase is effectuated by energy and momentum transfer due to bombardment with incident inert gas ions, usually Ar^+ [58]. In general, the sputter deposition process can be divided into three steps (Figure 4.1) [23]:

- (I) transition of the solid material into the vapour phase,
- (II) transportation of the vapour from the source to the substrate,
- (III) condensation of the vapour at the substrate surface and the formation of the film.

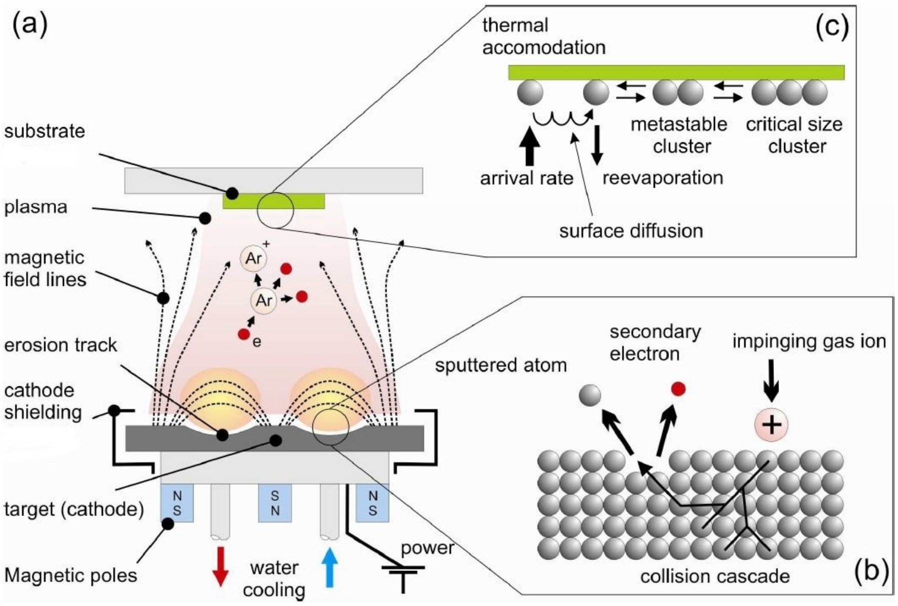

Figure 4.1: a) Schematic of an unbalanced magnetron sputtering system showing b) the collision cascade during sputtering and c) the nucleation process at the sample surface (modified from [59]).

The inert working gas is ionised by igniting a glow discharge between the cathode (often referred to as target) and the anode (chamber wall, sometimes also substrate holder). The impinging gas ions from the plasma cloud transfer their impulse to the target atoms, which causes further collisions within a collision cascade (Figure 4.1b). If the transferred energy is higher than the surface binding energy of the atoms, they can escape from the target surface, from the vapour phase and subsequently can condense at the substrate surface after transfer through the plasma cloud. (Figure 4.1c). In MSD the deposition rate can be enhanced by applying a magnetic field behind the target. The arrangement of the magnetic field lines is illustrated in Figure 4.1a. The electrons are trapped near the target surface in a torus shape, resulting in a high-density plasma and a distinct erosion zone. In the widely used unbalanced magnetron configuration, the magnetic field is strengthened at the outer diameter of the target area which allows some electrons to escape from the target-near region towards the substrate; there, the subsequent ionisation of inert gas atoms can be used to enhance film growth.

The films discussed in this work were synthesised in three different deposition systems due to their versatile settings and resulting deposition possibilites. For *Section 6,* a self-constructed laboratory-scale sputter deposition device as schematically shown in Figure 4.2 was used. The vacuum chamber is equipped with three circular planar targets (∅ 50 mm) and a rotatable substrate holder mounted opposite to the targets.

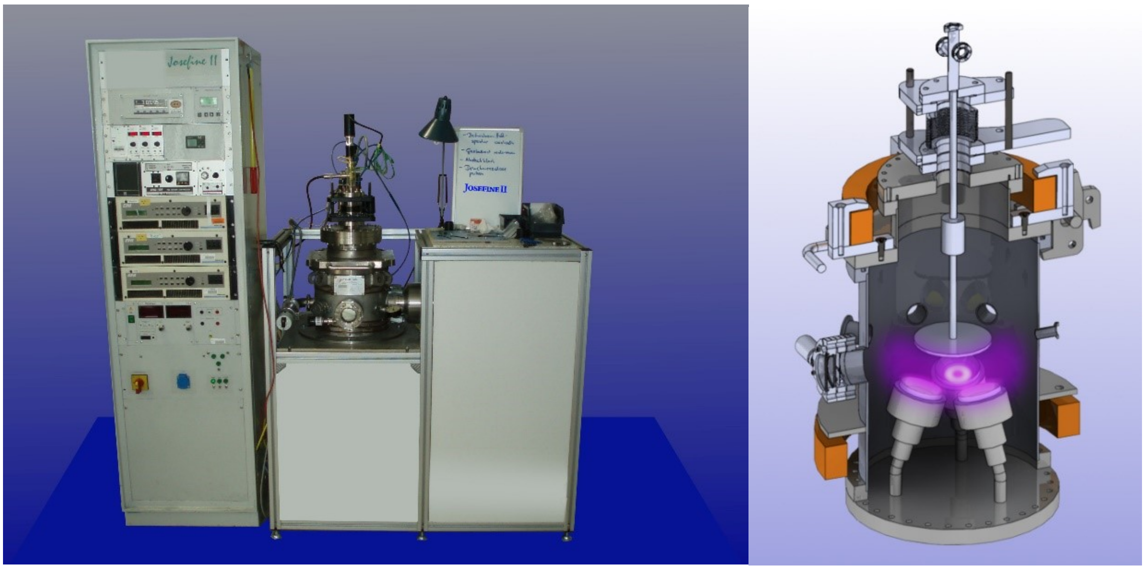

Figure 4.2: Laboratory-scale deposition plant with three targets used for film synthesis in *Section 6* (own working group).

The deposition plant used in *Section 7* is an industrial-scale in-line sputter deposition system (FHR.Line.600-V) with two chambers, a load-lock system and a deposition chamber equipped with a cylindrical rotatable target (∅ 160 mm × 600 mm). The substrate holder is mounted vertically and can be operated statically or dynamically in front of the target. An image of the sputter device with opened deposition chamber is shown in Figure 4.3.

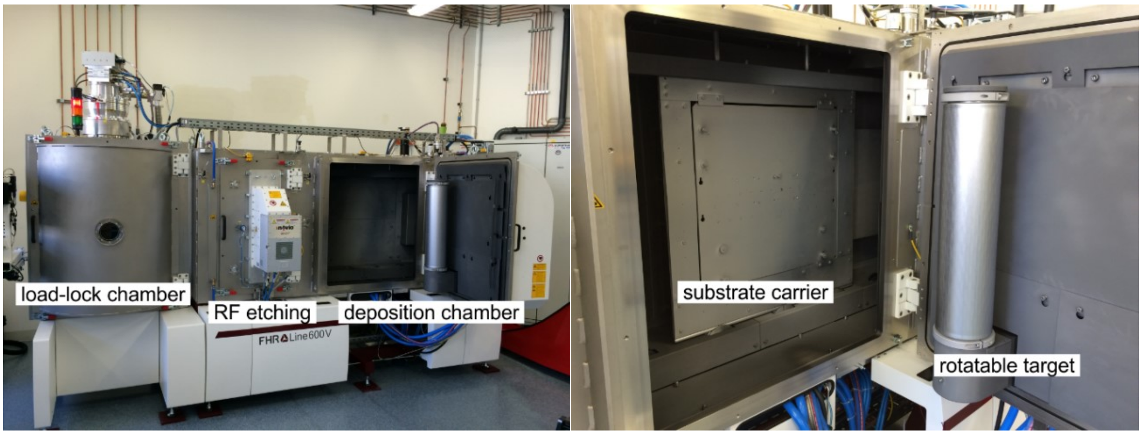

Figure 4.3: Industrial-scale in-line sputter device with cylindrical rotatable target used for film synthesis in *Section 7* (own work).

The films discussed in *Section 8* were synthesised in an AJA (ATC-1800 UHV) laboratory-scale deposition device shown in Figure 4.4. The setup is similar to the sputter device in *Section 6* but equipped with four circular planar targets (∅ 76 mm).

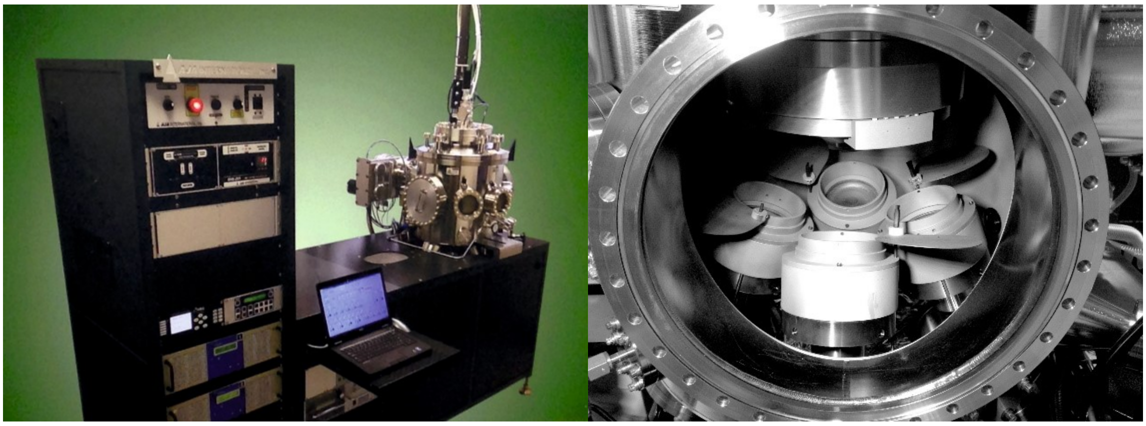

Figure 4.4: Laboratory-scale deposition plant with four targets used for film synthesis in *Section 8* (own working group).

4.2 Reactive Sputter Deposition

In general, alloys or compounds can be synthesised by either sputtering from compound targets, co-sputtering from single element targets or sputtering in the presence of a reactive gas (e.g. N_2, O_2) [60]. The latter case is dominated by three different possible reactions [60,61]:

(I) the compound is formed at the target surface and those are sputtered,

(II) the compound is formed in the gas phase,

(III) the reactive gas is adsorbed on the substrate surface and subsequently reacts with the impinging target atoms.

The third reaction pathway is observed most often. Compounds formed on the target surface will affect the sputter behaviour, the so-called target poisoning, which results in a lower deposition rate [27]. By adjusting the partial pressure of the reactive gas during the deposition process, the stoichiometry and properties of the synthesised films can be tuned [26]. The MoO_x films discussed in this work - besides sputtering from compound targets - were sputtered from a metallic Mo target in O_2/Ar atmospheres of varying compositions. By shifting the process gas composition from pure argon to pure oxygen, the synthesised MoO_x films varied from metallic Mo via MoO_2 dominated films to MoO_3 films with different optical and electrical properties. As mentioned before, target poisoning will affect the deposition rate as well as the discharge voltage due to oxides with reduced conductivity covering the target surface. Generally, there is a sharp transition between the metallic mode and the poisoned mode as illustrated by the example of Al_2O_3 in Figure 4.5a and b. At low oxygen partial pressure $p(O_2)$, the introduced oxygen is consumed in the growing film and the overall pressure stays constant and no or just minor oxide reaction layers are formed at the target surface. In this regime the discharge voltage remains unaffected showing the same value as in the case without O_2. At a certain point, when $p(O_2)$ is further increased, not enough Al atoms are available to bind all the oxygen and the target surface becomes covered by a continuous oxide layer of lower conductance. As a consequence, the pressure rises and the discharge voltage decreases. If $p(O_2)$ is now reduced, the covered target surface will be slowly sputter cleaned again. Since this typically happens at a lower $p(O_2)$, an hysteresis effect can be observed [27,62]. Compared to the Al_2O_3 example, the discharge voltage of the deposited MoO_x films increases significantly before it drops to a low value at high $p(O_2)$ (Figure 4.5c). Since the lower oxidised MoO_2 is electrically conductive, the deposition rate increases up to a $p(O_2)$ where the onset of MoO_3 film formation occurs. There, the deposition rate decreases significantly due to the insulating behaviour of the MoO_3 layer covering the target surface (Figure 4.5c).

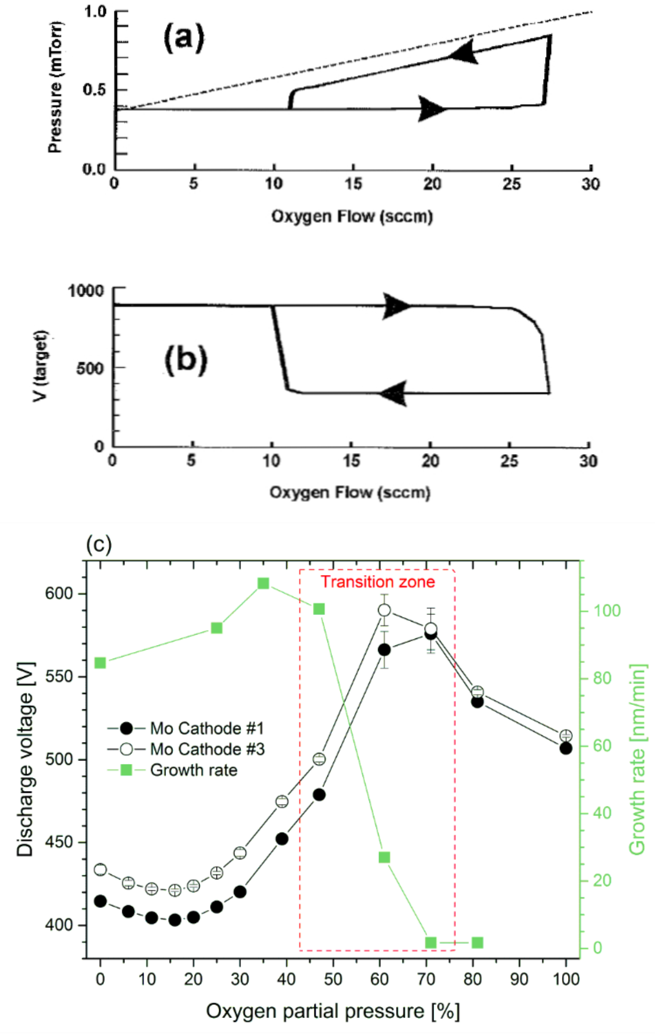

Figure 4.5: a) Pressure and b) discharge voltage hysteresis curve for an Al target [27] and c) discharge voltage and film growth rate for Mo target, both sputtered in oxygen containing atmosphere (own work).

4.3 Thin Film Nucleation and Growth

As soon as the sputtered atoms condense from the vapour phase at the substrate surface and are adsorbed, they diffuse along the surface until they reach an energetically attractive place or until they are desorbed again. Nucleation starts at favourable low energy sites like lattice defects, atomic steps or scratches on the surface. Substrate temperature, the intensity of interactions between species and substrate and the kinetic energy of the species control their atomic movement. Once a critical value of a metastable cluster size is reached, a stable nucleus of adsorbed particles is formed and continuous film growth starts [23,60]. Succeeding film growth can be distinguished into three modes illustrated in Figure 4.6 [23,60]:

(I) *Island growth (Volmer-Weber):* the binding energy between deposited atoms is stronger than to the substrate (3D growth mode) [23,60],

(II) *Layer-by-layer growth (Frank-van der Merwe):* the binding energy between deposited atoms and substrate surface is stronger than between the deposited atoms (2D growth mode) [23,60],

(III) *Stranski-Krastanov growth:* combination of mode (I) and (II), where one or more monolayers are formed until further layer growth becomes unfavourable and island growth occurs [23,60].

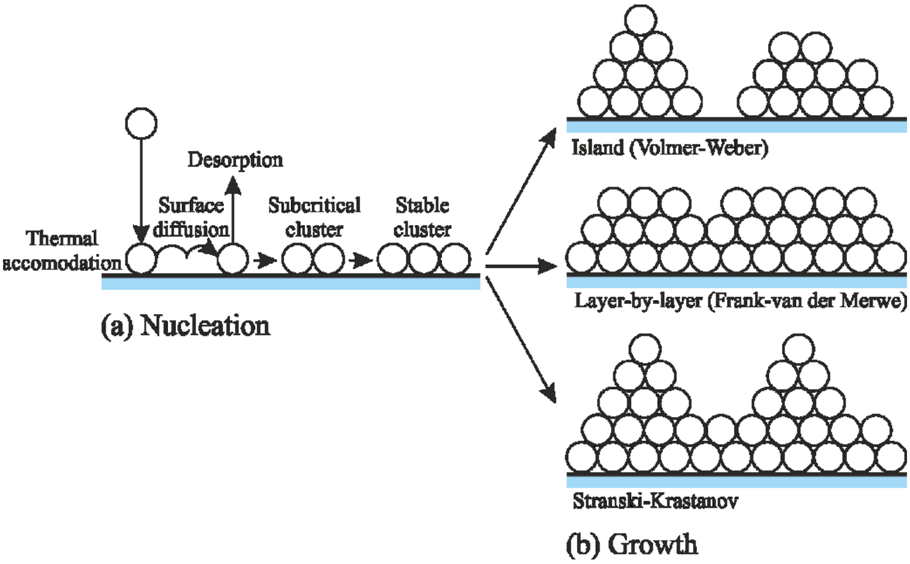

Figure 4.6: a) Nucleation process and b) the three film growth modes [63].

Deposition parameter like substrate temperature, the resulting film thickness and structural evolution are combined and illustrated in so-called structure zone models (SZMs). *Movchan and Demchishin* [64] were the first who investigated thick films grown by evaporation and related their structure to the homologous temperature (T_s/T_m), with T_s as substrate temperature and T_m as melting temperature of the film. The SZM after *Movchan and Demchishin* distinguishes three characteristic zones [64] (Figure 4.7). Later, *Thornton* [65] extended their model by adding the inert process gas pressure and therefore introduced a fourth zone, the transition zone T between zone I and II (Figure 4.8).

(I) Zone I: characterised by porous columnar structure due to shadowing effects and low surface mobility of the condensed atoms.

(II) Zone T: surface diffusion occurs and competitive growth results in a typical V-shaped film morphology transforming into columnar grains at higher film thickness.

(III) Zone II: characterised by dominating surface and beginning bulk diffusion, which leads to dense films consisting of columnar crystals.

(IV) Zone III: bulk diffusion dominates, resulting in a recrystallised structure with equiaxed grains and further densification.

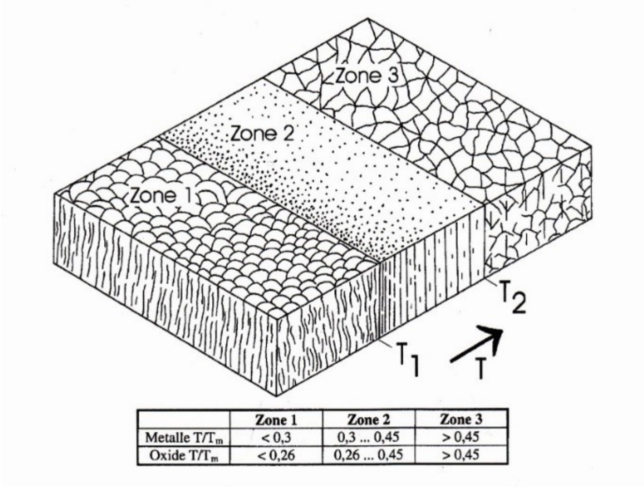

	Zone 1	Zone 2	Zone 3
Metalle T/T_m	< 0,3	0,3 ... 0,45	> 0,45
Oxide T/T_m	< 0,26	0,26 ... 0,45	> 0,45

Figure 4.7: Structure zone model after *Movchan and Demchishin* [64].

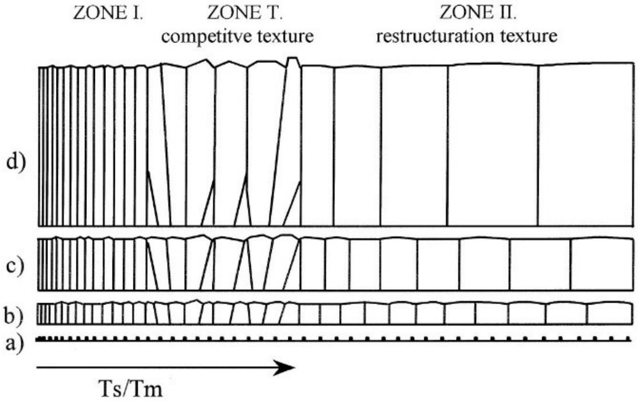

Figure 4.8: Structure zone model after *Thornton* [65].

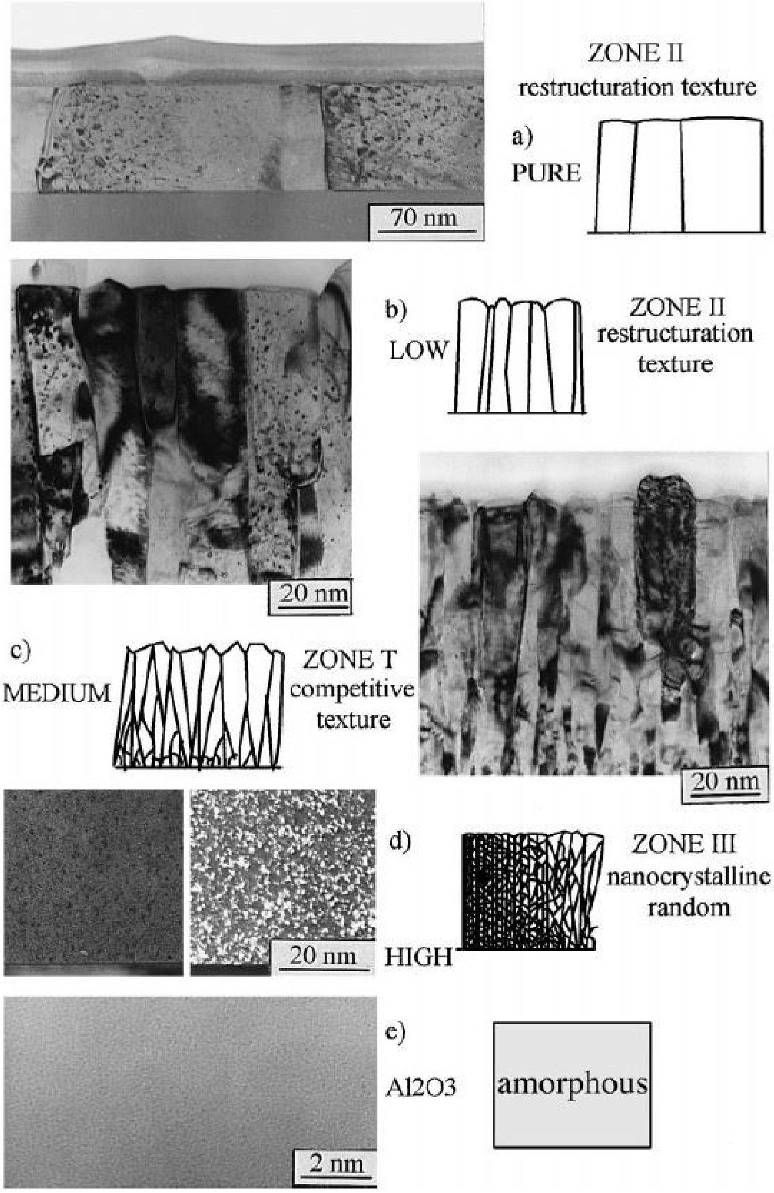

Figure 4.9: Structure zone model from *Barna and Adamik* [66].

For reactive sputtering the SZM adaption from *Barna and Adamik* [66], where impurity concentration is included as a parameter, is of special interest for this work. *Barna and Adamik* reported the changes in structure and orientation by means of the Al-O system with increasing oxygen content as impurity (Figure 4.9). A low level of oxygen concentration does not significantly affect the grain growth in the coalescence stage and of the growing crystals the structure resembles zone II. But the texture is generally less pronounced than in the impurity-free case due to decreased atom mobility at the contaminated grain boundaries. A medium level of oxygen concentration limits grain growth already in the coalescence stage.

The first crystals are randomly oriented and therefore competitive growth will occur. This structure can be compared to zone T of the basic SZM. A high level of oxygen concentration periodically blocks the growth of the crystals due to the formation of an oxidised surface covering layer. This continuous layer prevents crystal growth and causes permanent re-nucleation. The MoO_x films synthesised within this work are assumed to evolve after the SZM of *Barna and Adamik* and are discussed in detail in *Section 7*.

5 THERMAL STABILITY OF MoO_2 AND MoO_3 POWDERS

5.1 Introduction

In the phase diagrams of the binary system Mo-O as shown in Figure 5.1, two thermodynamically stable oxides were reported: molybdenum dioxide (MoO_2) and molybdenum trioxide (MoO_3). The experimentally derived phase diagram in Figure 5.1a is in good agreement with the theoretically calculated one in Figure 5.1b. The latter, however, illustrates an extended temperature region from 200 to 2700 °C. There, a eutectic point between Mo and MoO_2 can be noticed at 2200 °C. The composition reported in literature differs between experimentally derived (23 at.% O [30]) and theoretically calculated (15 at.% O [29]). At even higher temperatures, there is also a two-liquid region between Mo and MoO_2 visible which was already predicted by *Chang and Phillips* [28].

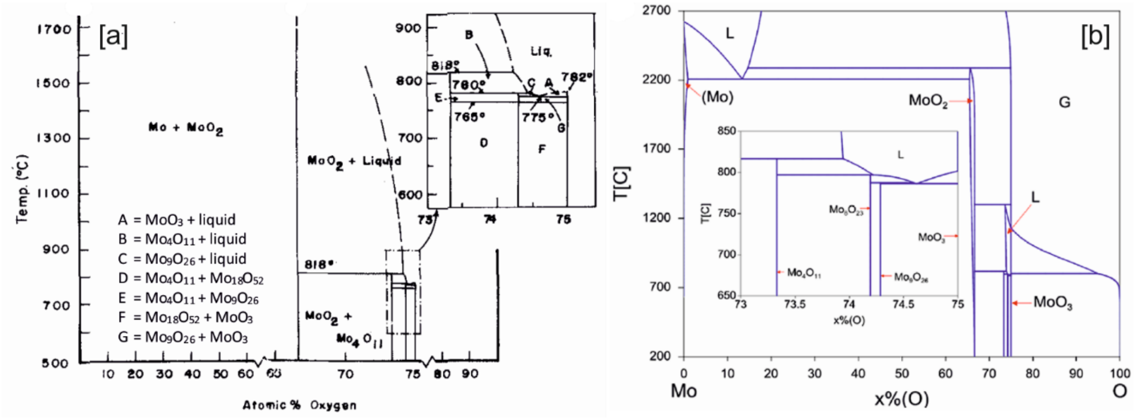

Figure 5.1: Phase diagrams of the binary Mo-O system: a) experimentally derived [28] and b) theoretically calculated [29].

With an oxygen content of 66.7 at.%, MoO_2 represents the lowest oxidation state of all molybdenum oxides (MoO_x). Its monoclinic crystal structure (see Table 5.1) is based on a deformed rutile lattice that consists of MoO_6 octahedra sharing edges and corners. The distortion of the crystal is caused by the Mo atoms which form direct metal-metal bonds in alternating metal-metal doublets [8,32]. This chemical bonding structure gives reason for the metal-like electrical conductivity of MoO_2, which is comparable to Mo as shown in Table 5.1. The visual appearance of MoO_2 is opaque with a reddish-brown to reddish-purple colouring [5,7].

The highest Mo oxidation state of 6+ is present in MoO_3 which has two modifications: the orthorhombic α-MoO_3 and the monoclinic β-MoO_3 (see Table 5.1). Similar to MoO_2, the thermodynamically stable α-polymorph of MoO_3 [34] consists of heavily distorted MoO_6 octahedra, but in this case they form a layered structure of two levels, each of which are mutually connected by shared octahedral edges. As a consequence, zig-zag rows are formed in [001] direction [5,35]. All metal-oxygen bonding orbitals in MoO_3 are filled and the energy states in the metal d-conduction band remain empty, resulting in a diamagnetic insulating behaviour [37]. Both MoO_3 modifications are transparent with a slightly yellowish visual appearance [32,38].

Table 5.1: Selected properties of the different MoO_x phases [6,8,39,41]. Metallic Mo is included as a reference. (m…metallic, sc…semiconducting, in…insulating)

Oxide		**Crystal structure**	**$T_{Formation}$ [°C]**	**Density [g/cm³]**	**Resistivity [Ωcm]**
Mo		*cubic*		*10.22*	*$5.03 \cdot 10^{-6}$ (m)*
MoO_2		monoclinic		6.47	$8.8 \cdot 10^{-5}$ (m)
Mo_4O_{11}	η-oxide	monoclinic	< 615	4.14	10^{-5} to 0.2 (m)
	γ-oxide	orthorhombic	> 615	4.18	0.25 (sc)
$Mo_{17}O_{47}$	κ-oxide	orthorhombic	< 560	4.72	< 0.05 (m → sc)
Mo_5O_{14}	θ-oxide	tetragonal	470 – 530		
Mo_8O_{23}	β-oxide	monoclinic	650 – 780	4.32	1.2 (sc)
Mo_9O_{26}	ζ-oxide	triclinic	600 – 750	4.74	250 (sc)
	β'-oxide	monoclinic	750 – 780	4.26	3.7 (sc)
MoO_3	α-MoO_3	orthorhombic		4.69	$1.7 \cdot 10^9$ (in)
	β-MoO_3	monoclinic			10^{10} (in)

Beside the stable oxides MoO_2 and MoO_3, several other MoO_x are reported in literature. *Schönberg* discussed the existence of a Mo_3O oxide with an oxygen content below the one of MoO_2, even though this was not prepared in a pure and stable state [31]. Despite the effort of many researchers to reproduce *Schönberg's* results, it remains uncertain whether such an oxide exists or not [28].

However, between the thermodynamically stable oxides MoO_2 and MoO_3 a series of metastable MoO_x phases with intermediate oxidation states exists, which are typically referred to as Magnéli phases. These oxides were first described by *Magnéli* in 1953, who studied the structure of the oxides in the system Mo-O by means of X-ray diffraction [33], and further investigations were done by *Kihlborg* in 1959 [6]. In contrast to MoO_2 and MoO_3 with narrow homogeneity regions of $MoO_{1.9\text{-}2.08}$ and $MoO_{2.95\text{-}3.0}$ [40], respectively, the Magnéli phase oxides only exist at an exact oxygen content. Arranged with increasing oxygen content, the following molybdenum oxide Magnéli phases are present in the binary Mo-O system: Mo_4O_{11}, $Mo_{17}O_{47}$, Mo_5O_{14}, Mo_8O_{23} and Mo_9O_{26}. Selected properties of these oxides are summarised in Table 5.1, whereas their stability ranges are indicated in Table 5.2. As can be noticed, Mo_4O_{11} and Mo_9O_{26} exist in two different modifications depending on the temperature [6]. The transformation of Mo_4O_{11} from the monoclinic η-polymorph to the orthorhombic γ-polymorph is a slow process lasting several weeks at temperatures between 550 and 655 °C [6]. Contrarily, the transformation from triclinic Mo_9O_{26} (ζ-oxide or so-called $Mo_{18}O_{52}$) to monoclinic Mo_9O_{26} (β'-oxide) takes place within two hours at 780 °C [6]. Both are transformations from a low temperature phase to a high temperature phase. The decomposition temperatures and reactions of the Magnéli phases are shown in Table 5.2. Further details about the structure of the MoO_x can be found in the chemistry handbooks, e.g. by Gmelin [42].

Table 5.2: Thermal stability of molybdenum Magnéli phase oxides [6,39].

Oxide	Transformation temperature [°C]	Decomposition temperature [°C]	Reaction equation
Mo_4O_{11}	550 - 655		$\eta\text{-}Mo_4O_{11} \leftrightarrow \gamma\text{-}Mo_4O_{11}$
		815 - 820	$\gamma\text{-}Mo_4O_{11} \rightarrow MoO_2 + 3\ MoO_3$ (gas.)
$Mo_{17}O_{47}$		630	$Mo_{17}O_{47} \rightarrow \gamma\text{-}Mo_4O_{11} + Mo_8O_{23}$
Mo_5O_{14}		530	$Mo_5O_{14} \rightarrow Mo_{17}O_{47} + MoO_3$
Mo_8O_{23}		785	$Mo_8O_{23} \rightarrow \gamma\text{-}Mo_4O_{11} + MoO_3$
$\zeta\text{-}Mo_9O_{26}$	760 - 780		$\zeta\text{-}Mo_9O_{26} \rightarrow \beta'\text{-}Mo_9O_{26}$
		550	$\zeta\text{-}Mo_9O_{26} \rightarrow \eta\text{-}Mo_4O_{11} + MoO_3$
$\beta'\text{-}Mo_9O_{26}$		785 - 800	$\beta'\text{-}Mo_9O_{26} \rightarrow \gamma\text{-}Mo_4O_{11} + MoO_3$

In terms of applications, MoO_x are often used as thin films for display technology, electrochromic glasses or solar cells for example. There, their wide range of electrical and optical properties depending on their oxidation state is exploited. State-of-the-art for synthesising such thin films is reactive magnetron sputter deposition and related techniques, where a metallic molybdenum target is reactively sputtered in a mixture of argon and oxygen gas atmosphere.

This study was done in order to investigate the possibility of producing sputter targets made of MoO_x powders for sputtering in pure argon atmosphere without additional oxygen in the gas. Therefore, the influence of phase purity of the powders on the thermal stability of various MoO_x is of interest for the sinter behaviour. The potential sinter possibility of this material gives new options for producing sputter targets and therefore for synthesising molybdenum oxide thin films non-reactively with tuneable optical and electrical properties for many different applications.

5.2 Experimental details

Four commercially available MoO_x powders from different manufacturers were used for the current study: two MoO_2 and two MoO_3 powders. In each case, one of the powders was phase-pure MoO_x, whereas the second powder contained a minor fraction of an additional MoO_x. In the further course of this work, the powders consisting of one MoO_x phase are referred to as single-phase MoO_2 and MoO_3 powders, while the other two are referred to as dual-phase MoO_2 and MoO_3 powders.

The particle size distribution of all powders was determined by laser diffraction according to the DIN ISO 13320-1 standard. For analysing the grain shape and agglomeration size before and after heat treatment, secondary electron images of the powders were taken with a Zeiss NTS Ultra-plus scanning electron microscope (SEM) with an acceleration voltage of 20 kV. The chemical composition of the powders was measured by energy dispersive X-ray spectroscopy (EDS) with an Octane Plus silicon drift detector, which is connected to the SEM. The identification of the different MoO_x phases and, hence, the characterisation of the phase purity was conducted by X-ray diffraction measurements (XRD) with a Bruker-AXS D8 Advance diffractometer, in Bragg-Brentano mode using Cu-K_α radiation and an energy-dispersive SolX detector from Bruker-AXS. References for the different phases were taken from the

International Centre for Diffraction Data (ICDD) database [67]. In addition, the virgin powders as well as the heat-treated ones were analysed by Raman spectroscopy to complement the XRD measurements. The spectra were recorded with a HORIBA Jobin Yvon LabRam-HR800 confocal spectrometer, employing a Nd:YAG laser with a wavelength of 532.2 nm at a power level of 3.5 mW at the measurement spot.

The phase stability of the powders at elevated temperatures was investigated by differential scanning calorimetry (DSC) and thermogravimetric analysis (TGA) with a SETSYS EVO 2400 device. Dynamical heating with a heating and cooling rate of ±10 K/min up to a maximum temperature just below the melting point (MoO_3: 795 °C) or decomposition temperature (MoO_2: 1100 °C) of the powders was performed in inert argon atmosphere (gas flow: 50 ml/min). To verify whether the chemical reactions during the heat treatment were completed or not, a rerun of each DSC/TGA measurement with the same powder sample and identical parameters was conducted.

5.3 Results and Discussion

5.3.1 Virgin powders

Prior to the heat treatment, all powders were characterised concerning their chemical composition, crystal structure, particle size, agglomeration size, and particle shape in their virgin state. Figure 5.2 shows XRD diffractograms of the different powders. Comparing the patterns of the two MoO_2 powders, a significant difference can be observed. One powder only shows peaks belonging to monoclinic MoO_2 and is therefore labelled as single-phase MoO_2. In contrast, the diffractogram of the dual-phase MoO_2 powder indicates a significant amount of Mo_4O_{11} in addition to the dominating MoO_2 phase. The diffractograms of the MoO_3 powders show a similar situation. The pattern of the single-phase MoO_3 powder reveals only the presence of the orthorhombic α-MoO_3 phase, whereas in the dual-phase MoO_3 powder a minor content of Mo_9O_{26} can be identified.

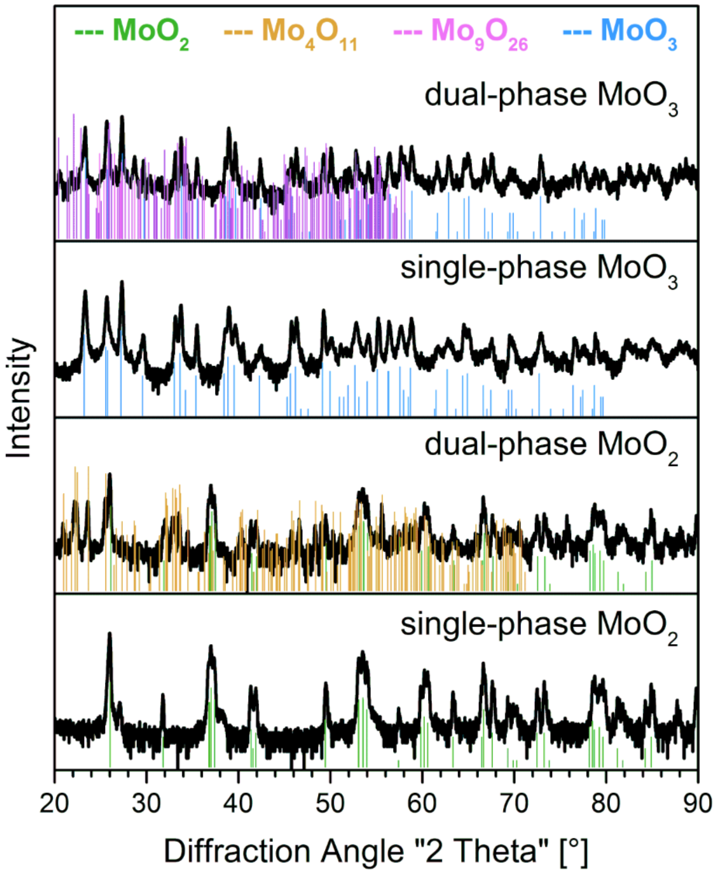

Figure 5.2: XRD diffractograms of the different MoO_x powders.

The Raman spectra of the different powders shown in Figure 5.3 generally confirm the phase structure obtained by the XRD measurements. The Raman spectra from the two MoO_3 powders, however, reveal the presence of orthorhombic MoO_3 with only very minor differences between both powders. The phase identification by XRD and Raman spectroscopy is also corroborated by the analysis of the chemical composition using EDS. Both MoO_2 powders consist of about 36 at.% Mo and 64 at.% O confirming the Mo/O ratio present in MoO_2. Apparently, the quantity of Mo_4O_{11} in the dual-phase MoO_2 powder is without significant influence on its overall chemical composition. In the case of the MoO_3 powder, the single-phase and the dual-phase powders have chemical compositions of about 24 at.% Mo and 76 at.% O as well as about 27 at.% Mo and 73 at.% O, respectively, which are in good agreement with stoichiometric MoO_3.

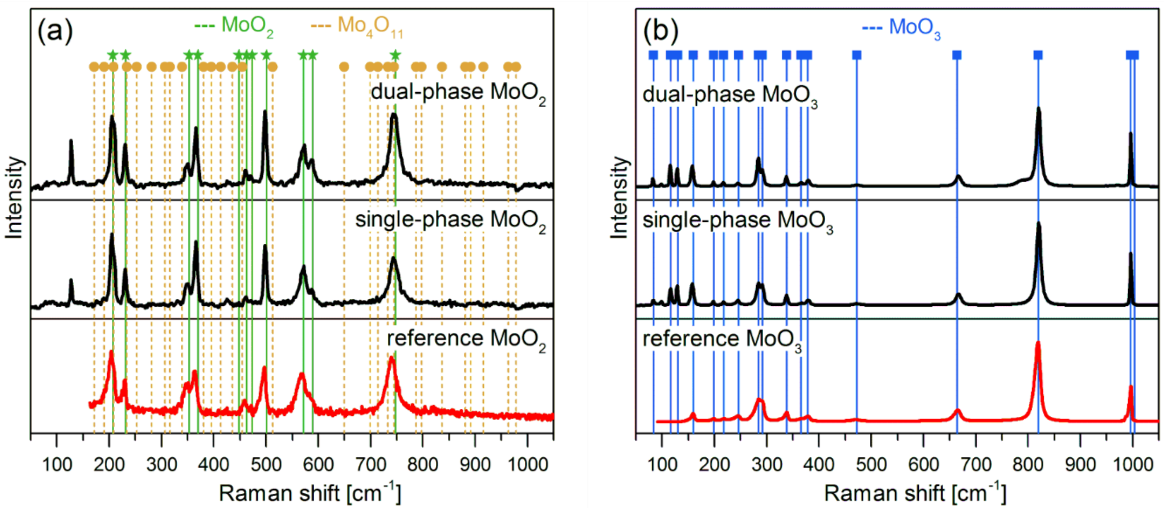

Figure 5.3: Raman spectra of the different MoO_x powders. Reference spectra of monoclinic MoO_2 and orthorhombic MoO_3 from the database in reference [68] are included as well.

Important aspects of powders are their particle size distribution and the shape of individual particles, which are presented in Figures 5.4 and 5.5, respectively. The single-phase MoO_2 powder shows a bimodal particle size distribution of 3 and 50 µm and homogenously distributed agglomerations in size and shape. As can be seen in Figure 5.5a, the particles are plate-shaped. The dual-phase MoO_2 powder, however, has a monomodal particle size distribution of about 7 µm and an agglomeration size of about 100 to 200 µm, as evidenced by the SEM images in Figure 5.5b. The powder consists of finely dispersed plate-shaped particles. Both MoO_3 powders revealed monomodal particle size distributions with preferred particle sizes of 1 µm in the case of single-phase MoO_3 and 27 µm in the case of the dual-phase MoO_3 (Figure 5.4). Even though the single-phase MoO_3 powder is the finest grained powder within this work, it shows an agglomeration size of 100 to 200 µm (see Figure 5.5c). In contrast, the dual-phase MoO_3 powder agglomerates non-uniformly in size and shape and the particle shape appears to be irregular (Figure 5.5d).

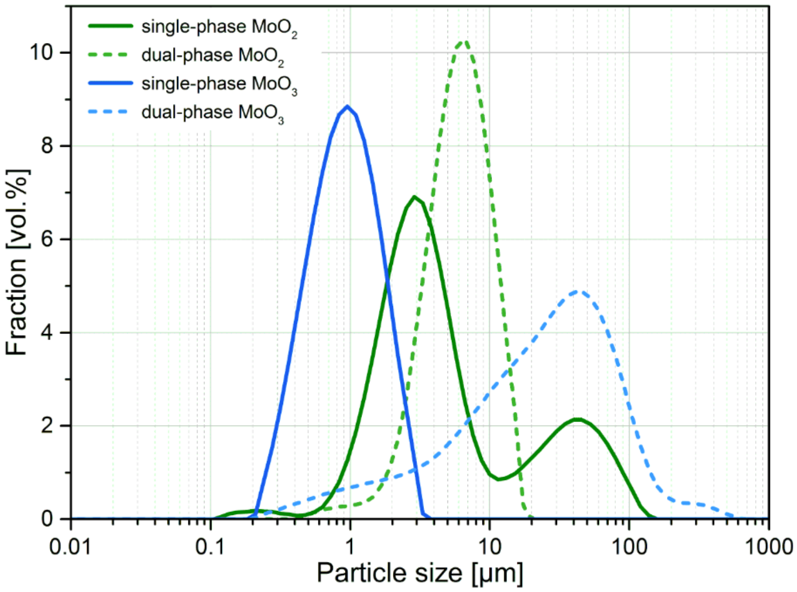

Figure 5.4: Particle size distributions of the different MoO_x powders.

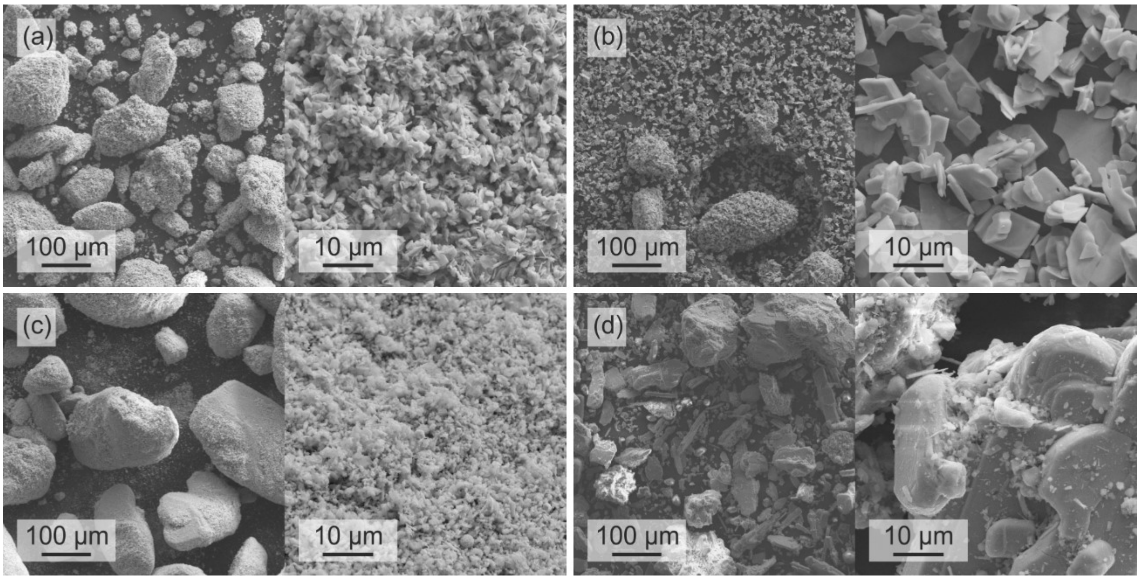

Figure 5.5: Secondary electron SEM images of a) single-phase MoO_2, b) dual-phase MoO_2, c) single-phase MoO_3 and d) dual-phase MoO_3.

5.3.2 Thermal stability

The DSC/TGA measurements reveal information about the thermal stability of the different MoO_x powders. As shown in Figure 5.6a, both the heat flow and the mass signal of the single-phase MoO_2 powder remain constant up to the maximum test temperature of 1050 °C. Such a behaviour can be expected due to the facts that this powder was phase-pure and that the maximum temperature was below the decomposition temperature of MoO_2, which is at about 1100 °C. In contrast, the heat flow signal from the dual-phase MoO_2 powder shows a well-defined peak at 830 °C (Figure 5.6b). With further increasing temperature, the mass of the analysed sample decreased by about 26% before it stabilised again at 1000 °C. According to the information provided in Table 5.2, the observed endothermic reaction is in agreement with the decomposition of γ-Mo_4O_{11} to MoO_2 and MoO_3 at about 820 °C. The mass loss is caused by the gaseous MoO_3 reaction product being removed from the sample volume.

Similar to the single-phase MoO_2 powder, the heat flow and the mass signal of the single-phase MoO_3 powder remained constant in the entire temperature range. The maximum testing temperature, however, was reduced to about 775 °C in order to prevent melting of the MoO_3 phase. The heat flow signal from the dual-phase MoO_3 powder shows an extended peak between 650 and 775 °C indicating one or several endothermic reactions. These reactions proceed without changes in the total mass and are, therefore, most likely phase change reactions. Possible reactions are ζ-Mo_9O_{26} → β'-Mo_9O_{26} at 760 - 780 °C and η-Mo_4O_{11} → γ-Mo_4O_{11} at 655 °C as already summarised in Table 5.2.

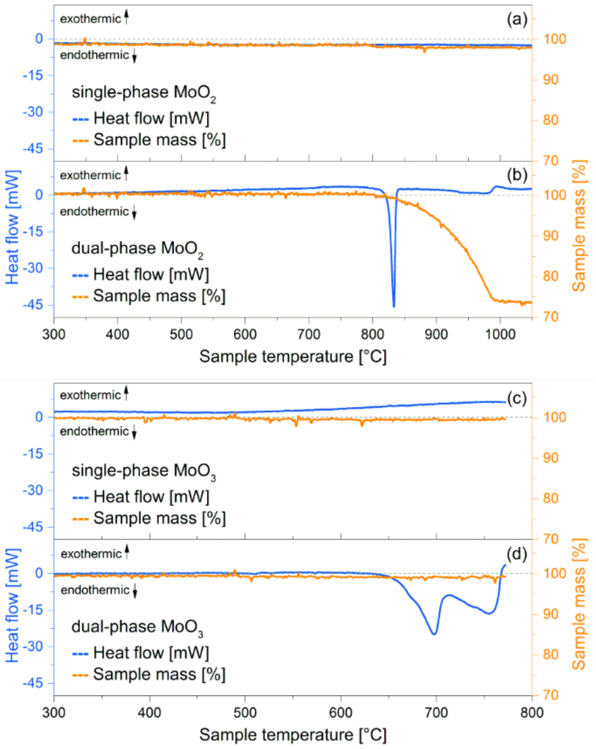

Figure 5.6: Heat flow and mass loss of a) single-phase MoO_2, b) dual-phase MoO_2, c) single-phase MoO_3 and d) dual-phase MoO_3, as determined by DSC/TGA.

5.3.3 Heat-treated powders

In order to identify possible changes in the structure and appearance of the MoO_x powders due to the heat treatment during the DSC/TGA measurements, the powders were analysed again. As shown in Figure 5.7, both heat-treated MoO_2 powders reveal identical XRD patterns and consist entirely of monoclinic MoO_2. This observation is confirmed by Raman spectroscopy, where spectra of the two powders resembling the reference spectrum of MoO_2 were recorded (Figure 5.8). In terms of chemical composition, only minor changes within the accuracy of the measurement were observed. The composition of the heat-treated single-phase and dual-phase MoO_2 powders are 34 at.% Mo and 66 at.% O and 36 at.% Mo and 64 at.% O, respectively.

The results regarding structure and chemical composition of the heat-treated dual-phase MoO_2 powder are in agreement with the previously discussed decomposition of the Mo_4O_{11} phase present in the virgin powder. Since this phase decomposed into solid MoO_2 and gaseous MoO_3, only monoclinic MoO_2 is present in the heat-treated powder.

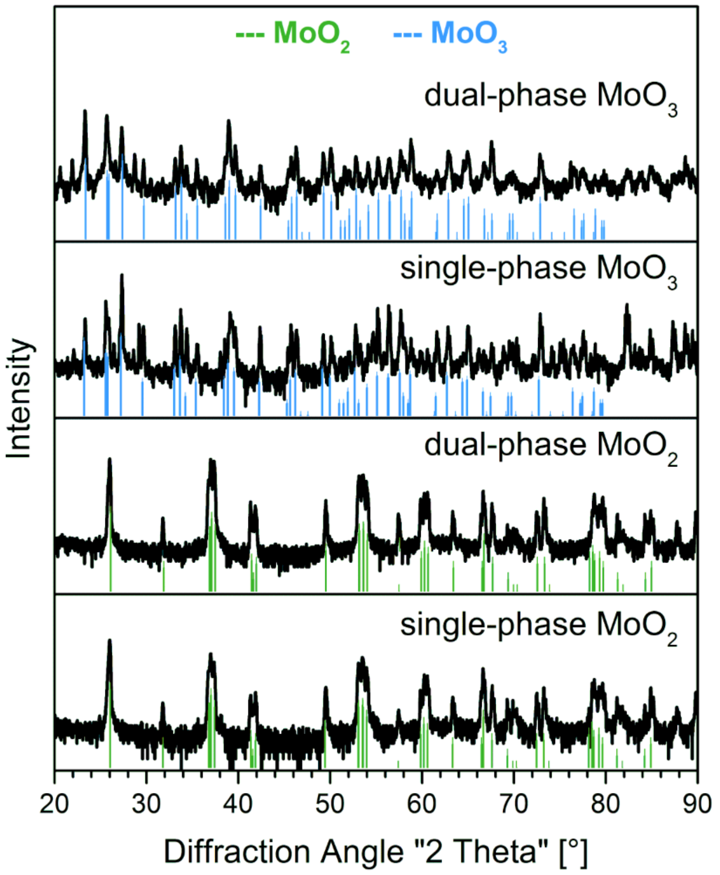

Figure 5.7: XRD diffractograms of the different MoO_x powders after heat treatment.

Similar to the MoO_2 powders, also the MoO_3 powders show similar XRD patterns and Raman spectra after the heat treatment (see Figures 5.7 and 5.8). The phase composition of single-phase MoO_3 powder is unaffected by the annealing up to 775 °C and it still consists of orthorhombic MoO_3. This phase is also the main phase in the heat-treated dual-phase MoO_3 powder, but slight deviations in the XRD pattern and the Raman spectrum as compared to the single-phase MoO_3 powder and references from literature indicate the presence of minor additional MoO_x phases. These additional MoO_x phases are also responsible for the changes in the heat flow signal during DSC measurements. Since the sample mass does not change, the heat flow peaks indicate a phase transformation without any gaseous reaction. Hence, the chemical composition of both MoO_3 powders remained unaltered with 25 at.% Mo and 75 at.% O and 23 at.% Mo and 77 at.% O for the single-phase and dual-phase powder, respectively.

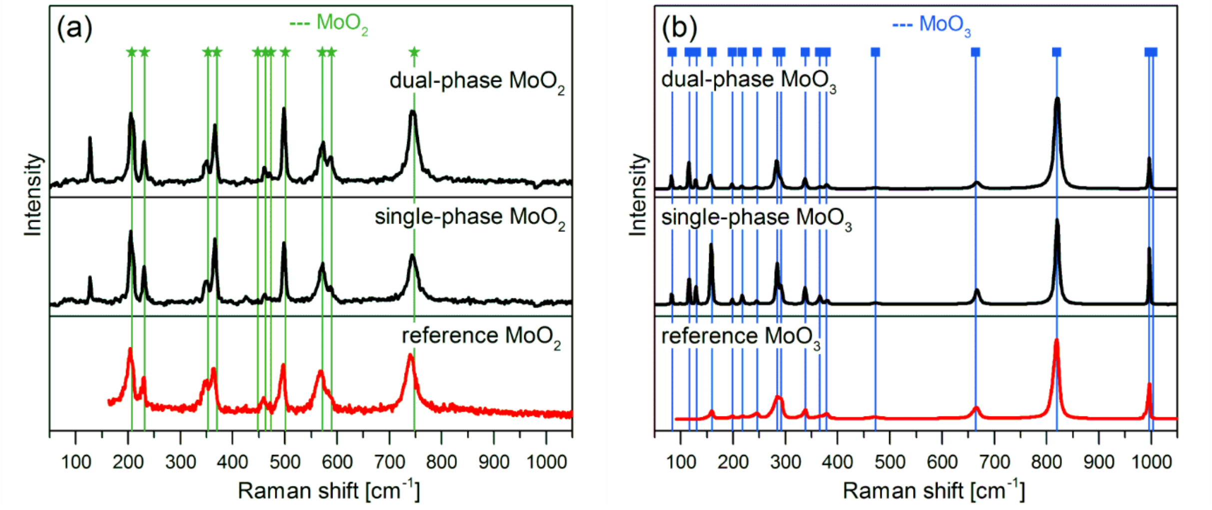

Figure 5.8: Raman spectra of the different MoO_x powders after heat treatment. Reference spectra of monoclinic MoO_2 and orthorhombic MoO_3 from database [68] are included as well.

Comparing the SEM images of the heat-treated MoO_2 powders shown in Figures 5.9a and b to the ones from the virgin powders (Figure 5.5) it can be noticed that no changes in the single-phase MoO_2 powder are apparent. The dual-phase MoO_2 powder, however, reveals slightly enlarged grains with rounded edges and corners as a result of the annealing treatment. It can be speculated that this change in shape is due to the decomposition reaction of Mo_4O_{11} to MoO_2 (the gaseous MoO_3 as a reaction product is without influence in this case). In contrast, significant changes in grain size and shape were observed in the case of the MoO_3 powders.

The dual-phase MoO_3 powder still consists of irregularly shaped grains, but their average size seems to be decreased. The opposite trend was observed for the single-phase MoO_3 powder. The once very fine-grained powder now shows plate- and rod-shaped particles with an average size of a few 10 µm, as evidenced by the SEM image in Figure 5.9c.

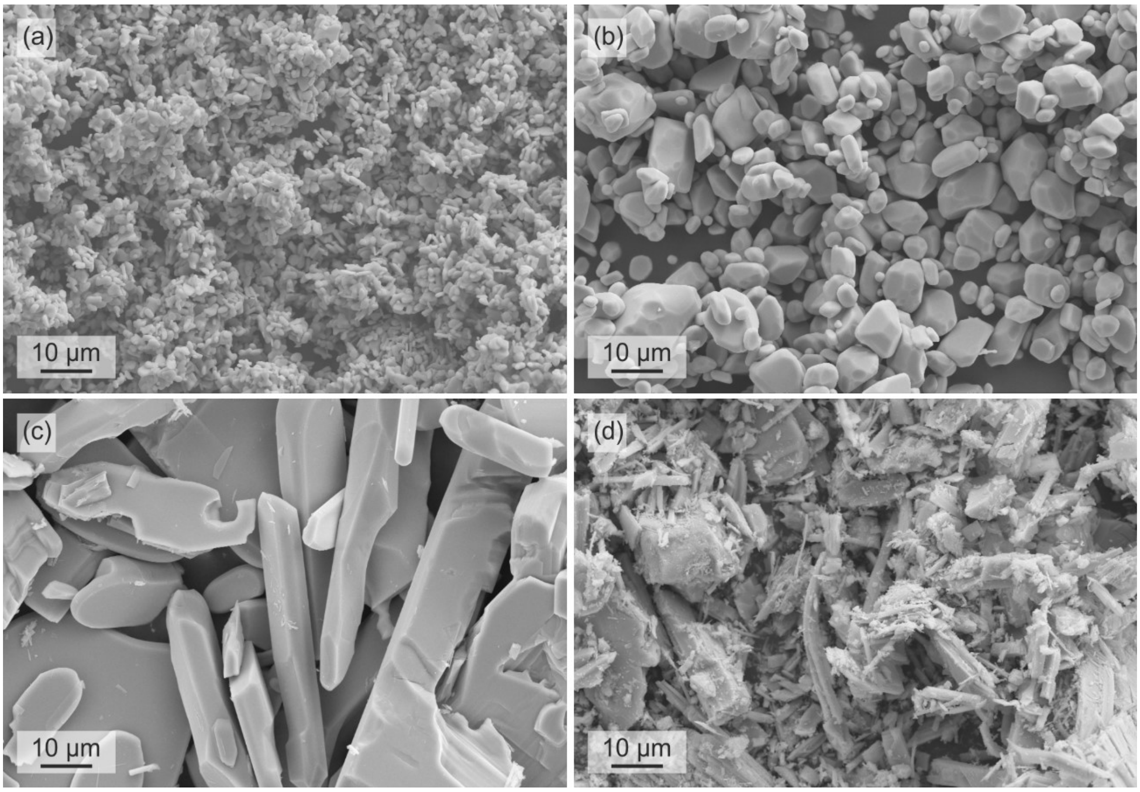

Figure 5.9: Secondary electron SEM images of the heat-treated a) single-phase MoO_2, b) dual-phase MoO_2, c) single-phase MoO_3 and d) dual-phase MoO_3.

The suitability of the MoO_x powders for sintering depends on the particles' ability to get compressed and to react with each other [69]. A first information on their suitability can be derived from the DSC measurements, in particular on the appearance of the powders after the associated heat treatment. While the single-phase MoO_2 powder does not show any tendency for agglomeration or sintering of the particles, the dual-phase MoO_2 indicates an early stage of sinter activity with changes in particle shape and size (Figure 5.9a and b). The same changes are true for the single-phase MoO_3, while the dual-phase MoO_3 is as irregular in particle size and shape as before the heat treatment. Finally, it can be concluded that in particular the change in appearance of the dual-phase MoO_2 and the single-phase MoO_3 provides first indications for a suitable sintering behaviour (see also Ref. [70]).

5.4 Conclusions

Within this work, different molybdenum oxide powders were investigated with respect to their powder characteristics and thermal stability. In addition, a survey of the present understanding of the molybdenum-oxygen binary system and the relevant MoO_x phases including their crystallographic structures and optical, electrical and mechanical properties is presented. Phase-pure and with other MoO_x phase contaminated MoO_2 and MoO_3 powders were investigated with respect to their particle shape and size distribution as well as their thermal stability. While single-phase MoO_2 and MoO_3 powders are stable up to 1050 and 775 °C, respectively, the Mo_4O_{11} and Mo_9O_{26} contaminations observed in the dual-phase powders undergo phase changes above 650 °C. The annealing experiments in combination with powder and phase characterisation of the different MoO_x powders provide first information for possible sinter applications, enabling manufacturing of MoO_x sputter targets for the non-reactive synthesis of functional thin films.

6 STRUCTURE EVOLUTION IN REACTIVELY SPUTTERED MOLYBDENUM OXIDE THIN FILMS

6.1 Introduction

Oxide thin films are used in a wide variety of industrial applications ranging from hard coatings to thin films in optical and electronic applications. Examples include Al_2O_3 used as a wear-resistant coating due to its high hardness and chemical inertness [71], TiO_2 due to photocatalytic properties [72] and transparent conductive oxide (TCO) materials like tin doped indium oxide (ITO) [4] or aluminium doped zinc oxide (AZO) [2,3]. By changing the stoichiometry or by alloying or doping the base materials, it is possible to tune the material properties according to the needs of the intended applications.

Different deposition techniques are employed to synthesise such thin film materials, e.g. chemical vapour deposition, sol-gel, printing, and physical vapour deposition techniques, in particular magnetron sputter deposition (MSD) [23]. MSD is a versatile deposition technique that can be used in direct current (dc), pulsed dc or radio frequency mode for the synthesis of a wide variety of materials including metals, nitrides, carbides, borides, sulfides or oxides. In the latter cases, reactive processes are frequently used, that means a reactive gas, for example oxygen, is added to the process gas during the deposition process [25]. The stoichiometry of the synthesised thin film can be tuned by varying the partial pressure of the reactive gas [26]. The chemical compound is typically formed by reactions between adsorbed reactive gas molecules on the substrate and impinging target atoms enabling the growth of the thin film. At the same time, compounds will also be formed on the target surface and, as a consequence, alter the sputter behaviour. If the target is in the so-called “poisoned” mode, then the sputter and deposition rates are typically lower [27].

The Mo-O system is known to contain two stable oxides, MoO_2 and MoO_3, as well as several Magnéli phases with intermediate Mo/O ratios [6]. All these oxides occur in different colours [5,7] and they cover a wide range of electrical and optical properties depending on their oxidation state. The properties of molybdenum oxides vary from a non-transparent appearance with metallic-like electrical conductivity (MoO_2) to transparent and electrically insulating behaviour (MoO_3). The electrical conductivity of the Magnéli phases ranges from a metallic to a semiconducting behaviour [8]. From the entire range of molybdenum oxides,

MoO_3 thin films are almost exclusively used in today's industrial applications like gas sensing [11], photovoltaic [12], electrochromic [9] and photochromic thin films [9,10]. The field of possible application for lower oxidised molybdenum oxide thin films remained largely unexplored so far.

This study was done in order to investigate the structure evolution in reactively sputtered molybdenum oxide thin films as a function of the oxygen partial pressure. The composition and structure of the synthesised films was analysed by electron probe microanalysis (EPMA) using wavelength-dispersive X-ray spectroscopy (WDS), X-ray diffraction (XRD) and Raman spectroscopy measurements. Details about the growth of molybdenum oxide thin films were obtained by scanning electron microscopy (SEM) top-view and cross-section imaging. The electrical resistivity and the optical appearance are discussed on the basis of changes of the film structure.

6.2 Experimental methods

The molybdenum oxide thin films were grown on (100)-oriented silicon (20 mm × 6 mm × 0.35 mm) and soda lime glass (20 mm × 6 mm × 1 mm) substrates by unbalanced dc-MSD. Prior to the deposition, the substrates were cleaned in ultrasonic baths of acetone and ethanol and dried with hot air. After mounting the samples on the rotatable substrate holder, the deposition chamber was evacuated to a base pressure below $1 \cdot 10^{-3}$ Pa and was baked out at 500 °C for 30 min. Subsequently, the temperature was decreased to 120 °C and the targets were sputter-cleaned in pure Ar atmosphere for five minutes, while a shutter shielded the substrates to prevent deposition of Mo on them in this stage. The MoO_x films were grown at a substrate temperature of 120 °C in reactive O_2/Ar atmosphere at an average pressure of $p_{tot} = 0.4$ Pa. To investigate the influence of the oxygen content on the structure and properties of the deposited films, the oxygen partial pressure $p(O_2)$ during deposition was varied between 0 and 100% of the total pressure as shown in Table 6.1. In order to facilitate a comparison with other deposition systems with different configurations of magnetrons, pumping speeds and process gas insertion among others, the oxygen partial pressure is given relative to the total pressure in this work. The total gas pressure in the vacuum chamber during the depositions was monitored with a compact full-range gauge (Pfeiffer PKR 251). The oxygen partial pressure, however, was calculated from gas flow - pressure calibration curves obtained prior to the depositions using a hot cathode ion gauge (Leybold Ionivac) since its accuracy of ±15% [73] is better in the pressure range of interest than the one of the full-range gauge with approximately ±30% [74].

Table 6.1: Variation of the relative oxygen partial pressure $p(O_2)$ during deposition with p_{tot} = 0.4 Pa.

$\mathbf{p(O_2)/p_{tot}}$ [%]	0	28	39	48	74	90	100
Ar Flow [sccm]	40	35	32	30	20	10	0
$\mathbf{O_2}$ **Flow** [sccm]	0	5	7.5	10	20	30	40

A constant direct current of 0.35 A was applied to each of the two Mo targets (diameter of 50 mm), which were mounted on magnetrons positioned opposite to the substrate holder [63]. The resulting discharge voltage as a function of the oxygen partial pressure is displayed in Figure 6.1a. The deposition time of 30 min was kept constant. An asymmetrically bi-polar pulsed dc bias voltage with a frequency of 250 kHz and negative and positive pulse durations of 3.5 µs (-50 V) and 0.5 µs (+37 V), respectively, was applied to the substrate holder.

For analysing the microstructure of the films, cross-section as well as top-view secondary electron images were taken with a Zeiss NTS Ultra-plus SEM with an acceleration voltage between 3 and 5 kV. The chemical composition of the different MoO_x films was measured by EPMA with an electron energy of 10 keV and a current of 100 nA. The identification of the crystalline oxide phases present in the films was conducted via XRD with a Bruker-AXS D8 Advance diffractometer. The measurements were done in grazing incidence mode with a fixed angle of incidence of 2° and a step of detector movement of 0.02° with an accumulation time period of 1.2 s. The diffractometer was operated at 40 mA tube current and 40 kV voltage. Cu-K_α radiation (wavelength: 0.154056 nm) and an energy-dispersive SolX detector from Bruker-AXS were used. References for phase identification were taken from the International Centre for Diffraction Data (ICDD) database [67]. To confirm the results of the XRD measurements, the films were also analysed by Raman spectroscopy with a HORIBA Jobin Yvon LabRam-HR800 confocal spectrometer equipped with a Nd:YAG laser (wavelength: 532.2 nm, power at the measuring spot: 3.5 mW). For qualitative analysis of the transparency, digital images of the coated glass substrates were taken. The electrical resistivity was measured by a Jandel four point probe. The biaxial stress measurements were carried out on a custom-built device using the reflection of two parallel laser beams to determine the curvature radius of the coated samples as described in [75]. The residual stress was then calculated by means of the modified *Stoney's* equation [76,77].

6.3 Results

Figure 6.1 shows the evolution of the discharge voltage, the growth rate and the oxygen content in the synthesised MoO_x films depending on the oxygen partial pressure during deposition. With oxygen partial pressure increasing from 0 to 50%, the discharge voltage rose by about 50% while the film growth rate increased from ~40 to ~90 nm/min resulting in a higher film thickness (Figure 6.2) as the deposition time was kept constant. At the same time, the oxygen content increased from ~7 to ~64 at.%, while the Mo content decreased accordingly. The oxygen content of approximately 7 at.% in the pure Mo films might originate from surface oxidation of the sample after deposition due to the time delay between deposition and EPMA measurement and an overestimation of oxygen content by the EPMA method in particular at low oxygen contents. A further increase of the oxygen partial pressure to values above 50% led to a slightly decreasing discharge voltage, a drastic decrease in the film growth rate to ~7 nm/min and a slight increase in the oxygen content up to ~75 at.%.

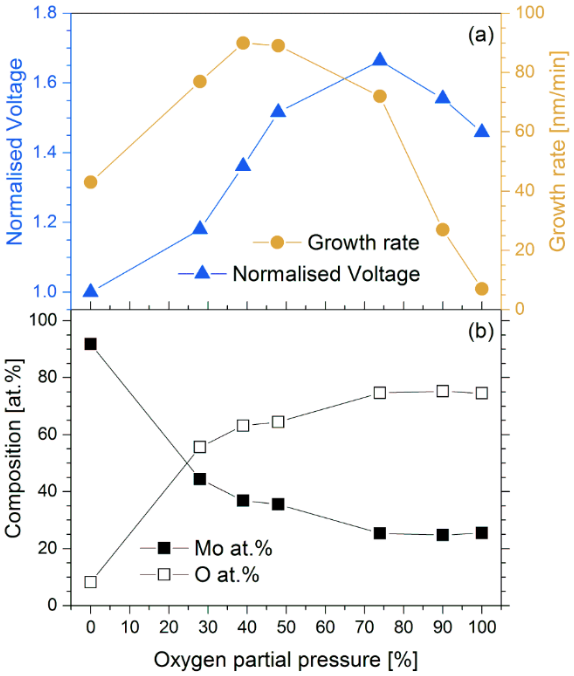

Figure 6.1: a) Discharge voltage (normalised to the initial value of 305 V) and film growth rate as well as b) chemical composition of the synthesised MoO_x thin films as a function of the oxygen partial pressure.

Figure 6.2 shows top-view and cross-section SEM images. The molybdenum film deposited in pure Ar atmosphere (Figure 6.2a) exhibits a well-defined structure with columnar grain growth in cross-section and flat, plate-like shaped grains in top view. The film with $p(O_2) = 28\%$ (Figure 6.2b) has a featureless structure, whereas islands and clusters are visible in the top-view of the film with $p(O_2) = 39\%$ (Figure 6.2c). For the latter, the onset of a columnar growth mode can be observed in the cross-section. In the case of the film with $p(O_2) = 48\%$ (Figure 6.2d), the cross-section image reveals a dense columnar structure. The surface micrograph of the film with $p(O_2) = 74\%$ (Figure 6.2e) illustrates the existence of differently shaped and horizontally aligned flat and flaky crystals. Some of them are needle-like pointing out of the surface and seem to consist of bundles of flat crystals growing in different directions. The cross-section image shows a columnar structure and, due to the vertically oriented crystals, a rough specimen surface. The two MoO_x films deposited at the highest oxygen partial pressures show very similar structures (Figures 6.2f and g). Their surfaces are characterised by flat and flaky grains with orientations parallel to the surface and their cross-sections appear dense and columnar.

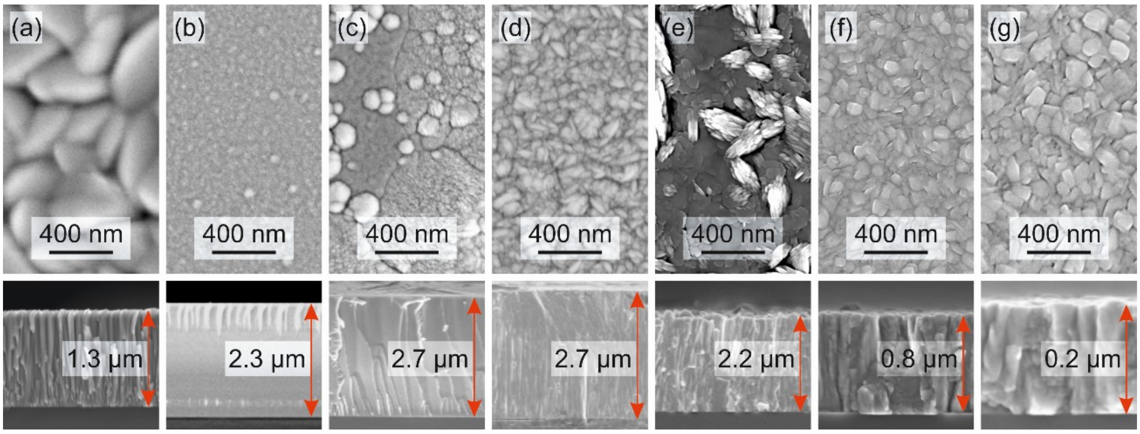

Figure 6.2: Top-view (upper row) and cross-section (lower row) secondary electron SEM images of the synthesised MoO_x thin films with varying oxygen partial pressure used during deposition: a) 0%, b) 28%, c) 39%, d) 48%, e) 74%, f) 90% and g) 100%.

The XRD diffractograms of the MoO_x films deposited on silicon substrates are shown in Figure 6.3 for increasing $p(O_2)$. The film deposited with $p(O_2) = 0\%$ shows the expected body-centred cubic structure of Mo. At low oxygen partial pressure ($p(O_2) = 28\%$), the film shows a nanocrystalline or even amorphous-like structure. With further increasing $p(O_2)$ up to

48%, a well-defined crystalline structure developed which is dominated by monoclinic MoO_2. In addition, there are traces of orthorhombic Mo_4O_{11} present in these films. Apparent peak shifts between the measured patterns and the reference peak positions are most likely related to residual compressive stresses in the films which are in the range of -100 to -1200 MPa. Exceeding the oxygen partial pressure to above 50% results in the formation of a structure dominated by orthorhombic α-MoO_3 with fractions of monoclinic β-MoO_3 as well as triclinic Mo_9O_{26} (tri-Mo_9O_{26}). Among these films, the MoO_x film deposited at $p(O_2)$ = 74% revealed a higher degree of crystallinity which can be understood by the higher film thickness.

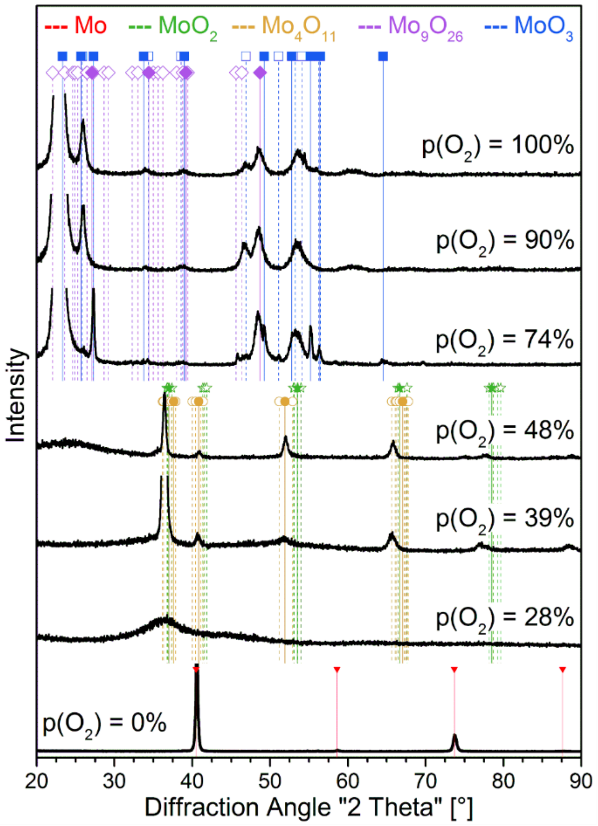

Figure 6.3: XRD diffractograms of the synthesised MoO_x thin films with varying oxygen partial pressure used during deposition (silicon substrates, reference peak positions according to [67]; solid symbols: high intensity peaks; open symbols: low intensity peaks).

To support the phase identification based on the XRD measurements, Raman spectra were recorded from all MoO_x films as shown in Figure 6.4. A spectrum of the film deposited at $p(O_2) = 0\%$ is not included since metallic Mo is not Raman active. Similar to the XRD observations, the synthesised MoO_x films can be divided into two groups depending on the used oxygen partial pressure during deposition. At $p(O_2)$ values of up to 48%, the films revealed broad bands of low intensity. Comparing these features with the reference spectrum of MoO_2, some similarities can be noticed. However, since the MoO_x films synthesised at low $p(O_2)$ are only weakly Raman active as seen in Figure 6.4 and present a nanocrystalline morphology, an unambiguous identification of MoO_2 phases by Raman spectroscopy is challenging. Well-defined peaks are visible in the Raman spectra of the MoO_x films deposited with oxygen partial pressures exceeding 50% (Figure 6.4). These films are dominated by MoO_3 and Mo_9O_{26}. Slight peak shifts with respect to the reference peak positions are most likely due to residual stresses present in the films.

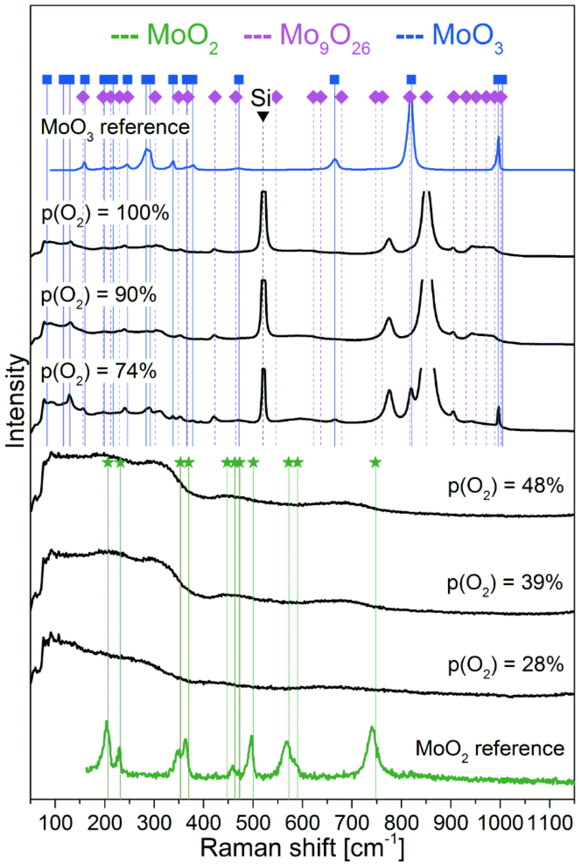

Figure 6.4: Raman spectra of the synthesised MoO_x thin films with varying oxygen partial pressure used during deposition (silicon substrates). Reference spectra of monoclinic MoO_2 and orthorhombic α-MoO_3 from database [68] are included as well as reference peak positions of MoO_2, α-MoO_3 and tri-Mo_9O_{26} from [38].

Subsequent to the structural characterisation of the MoO_x films, their optical appearance and electrical conductivity were analysed in order to evaluate their suitability for possible applications qualitatively. Figure 6.5 shows photographs of the different MoO_x films deposited on window glass where their transparency and reflectivity can roughly be estimated. Beside the metallic film deposited with $p(O_2) = 0\%$, again two groups of MoO_x films can be identified. Films deposited at low oxygen partial pressure ($p(O_2)$ = 28, 39 and 48%) show a metallic, dark and non-transparent appearance, whereas films deposited at high oxygen pressure ($p(O_2)$ = 74, 90 and 100%) are (semi-)transparent with a slight yellowish colouration.

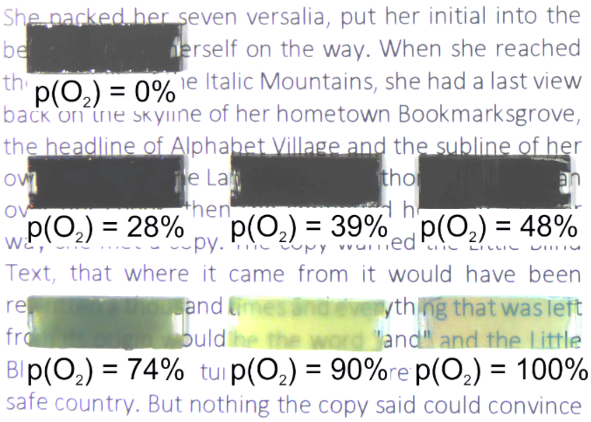

Figure 6.5: Optical appearance of the synthesised MoO_x thin films with varying oxygen partial pressure used during deposition.

In terms of electrical properties, the resistivity of the MoO_x films changed from electrical conductive to insulating as shown in Figure 6.6. The film deposited at $p(O_2) = 0\%$ showed a resistivity comparable to metallic Mo. With increasing oxygen partial pressure, the resistivity of the MoO_x films increased by two orders of magnitude and remained constant from 28 to 48% (variations are considered to be insignificant). At partial pressures above 50%, the films are marked as insulating since electrostatic charging effects due to their low conductivity inhibited the determination of reliable values of their resistivity.

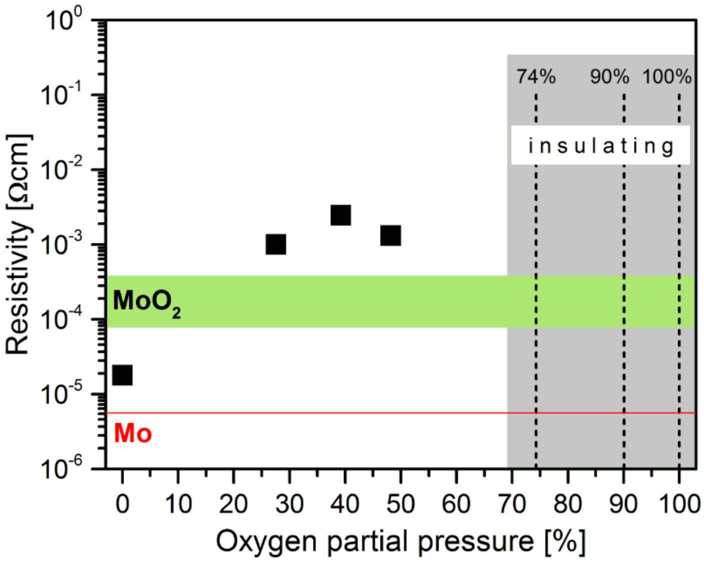

Figure 6.6: Electrical resistivity of the synthesised MoO_x thin films as a function of the oxygen partial pressure used during deposition. Reference values for Mo and MoO_2 are included [8,32,78].

6.4 Discussion

The variation of the oxygen partial pressure allows for studying the influence of the deposition conditions on the structure and properties of MoO_x films. The initial increase in the growth rate upon increasing the oxygen partial pressure up to 50% is due to the fact that more film forming species (Mo and O atoms and ions, as well as Mo and O containing molecules and molecular ions) are available, while the sputter rate of the Mo target remains largely constant. In contrast, the rise in the discharge voltage in this range of oxygen partial pressures indicates the formation of an oxide layer on the target surface, which is typically referred to as "target poisoning" [27]. It is apparent that the adsorption of oxygen to the target surface at oxygen partial pressure values below 50% causes a change in the electron emission, since a higher voltage is necessary to maintain the discharge, but the sputter and film growth rate remain unaffected [27].

The MoO_x films that are formed on the substrates in this regime have a MoO_2 dominated crystal structure, which is confirmed by the measured oxygen contents between 63 and 65 at.%. The reported homogeneity region of MoO_2 is $MoO_{1.9\text{-}2.08}$ [40] with oxygen contents between 63 and 69 at.%. The slight deviation indicates that amorphous phases with low oxygen content are present in these films. In the recorded XRD patterns of the films deposited with oxygen partial pressures up to 50% broad features appear at angles between 20 and 40° indicating the presence of additional amorphous phases.

Further increasing the oxygen partial pressure up to 100% results in a strong decrease of the growth rate. This evolution is caused by a second stage in target poisoning, where the sputter yield of the target and hence the growth rate are significantly reduced due to the formation of the oxide layer on the target's surface [27]. In addition, the sputter yield decreases because ions bombarding the target surface change from heavy Ar to light O ions [27]. The slight decrease in discharge voltage at p(O2) values between 74 and 100% indicates a slightly enhanced electron emission from the oxide layer formed in this stage of the target poisoning. The MoO_x films synthesised in this regime revealed a dominating phase with the structure of the Mo oxide with the highest oxidation state, i.e. MoO_3. The measured oxygen contents for these films are in agreement with the stability region of MoO_3 which is between 74 and 75 at.% of oxygen.

The separation of the deposited MoO_x films into two regimes continues when evaluating the optical and electrical properties. The films deposited at low oxygen partial pressures with MoO_2 structure are non-transparent and conductive as can be expected from literature [8]. However, their colour is black unlike the typically reported reddish-brown, reddish-purple colouring of MoO_2 [5] and their resistivity is one order of magnitude higher than reference values from literature (Figure 6.6). This might be caused by a high defect density present in the films hindering the motion of both, electrons and photons, through the material. In contrast, the films deposited at high oxygen partial pressure with MoO_3 dominated structure are (semi-)transparent with a yellowish colouring similar to [79]. The fact that a Si peak originating from the substrate was recorded in the Raman spectra from these films confirms their high transmittance. Resistivity values reported for MoO_3 are in the range from 10^7 and 10^{10} Ωcm [8]. Such high resistivity values are beyond the measurable range of the used four point probe and these films have therefore been labelled as insulating in Figure 6.6.

6.5 Conclusions

Within this work, molybdenum oxide thin films were deposited by reactive dc magnetron sputtering from molybdenum targets. The oxygen/argon process gas ratio was changed from pure argon to pure oxygen by varying the gas flow during deposition. The film growth rate decreased from 90 to 7 nm/min with increasing oxygen partial pressure. Films deposited at low oxygen partial pressures of up to 50% have a MoO_2 dominated structure and are non-transparent and electrically conducting. In contrast, the films deposited at higher oxygen partial pressures of up to 100% consist mainly of a MoO_3 phase structure. These films are transparent with a yellowish colouring and electrically insulating. In conclusion, structure and properties of the deposited molybdenum oxide thin films are tuneable by adjusting the oxygen/argon ratio in the process gas during deposition. This makes the films in the binary system Mo-O promising materials for a wide range of optical and electronic applications.

7 INDUSTRIAL-SCALE SPUTTER DEPOSITION OF MOLYBDENUM OXIDE THIN FILMS: MICROSTRUCTURE EVOLUTION AND PROPERTIES

7.1 Introduction

Technological progress in the field of display technologies and related areas like solar cells or electrochromic glasses has gained momentum in recent years. Electronic displays find their way into our everyday life and their structure becomes more and more complex. For the imaging process materials are needed which combine good electrical conductivity and high optical transparency. In particular, a certain group of metallic oxides show such a behaviour [1], the so-called transparent conductive oxides (TCO). TCOs are used, for example, as electrode materials in flat-panel displays which are based on thin film structures. Common TCO materials are aluminium doped zinc oxide (AZO) [2,3] and tin doped indium oxide (ITO) [4]. Especially ITO is well established in industry but it has one major disadvantage, the limited availability of indium and a therefore high world market price. In addition, the applications that make use of TCO materials get more and more complex, so that material systems that can be adapted to new requirements are needed.

The properties of oxides can often be tuned by changing their stoichiometry or by alloying or doping. In particular, depending on their oxidation state, molybdenum oxides (MoO_x) are known to have a wide range of electrical and optical properties, ranging from a non-transparent appearance with metallic-like electrical conductivity (MoO_2; Mo^{4+}) to a transparent and electrically insulating behaviour (MoO_3; Mo^{6+}). Additionally, several MoO_x like Magnolia phases between the most stable oxidation states 4+ and 6+ were reported [5–8]. Their electrical conductivity shows a behaviour ranging from metallic to semiconducting. While MoO_3 thin films are established in industrial applications like photovoltaics [12], gas sensors [11], or electrochromic [9] and photochromic glasses [9,10] the potential of thin films of MoO_x with lower oxidation states for industrial applications remains largely unexplored up to now [13–16].

To synthesize such thin film materials different deposition techniques can be used, e.g. sol-gel [18–20], printing [17], chemical vapour deposition [18,21,22] and physical vapour deposition techniques with magnetron sputter deposition (MSD) in particular [18,23,24]. The use of reactive processes in MSD is common, which means that a reactive gas, for example O_2, is added to the process gas during deposition [25]. Thereby, the growth of the films is enabled by the chemical compound typically formed by reactions between adsorbed reactive gas molecules on the substrate and impinging target atoms. Simultaneously, compounds will also be formed on the target surface, which in turn affects the sputter behaviour and results in the so-called poisoned mode, where the sputter and deposition rates are typically reduced [27]. Moreover, the stoichiometry and therefore the properties of the synthesized films can be tuned by varying the partial pressure of the reactive gas [26].

This study was done in order to investigate structure and properties of reactively sputter deposited molybdenum oxide thin films as a function of the oxygen partial pressure $p(O_2)$. The films were synthesized in an industrial-scale deposition plant to enable the evaluation of their suitability for industrial applications. Apart from analysing composition and structure of the films, the focus was on analysing the optical properties like transmittance, reflectance and absorbance as well as on electrical resistivity to determine the potential of molybdenum oxide thin films for display and other opto-electronic applications.

7.2 Experimental details

The MoO_x thin films were grown on (100)-oriented silicon (15 mm × 15 mm × 0.35 mm), soda lime glass (50 mm × 50 mm × 1 mm) and alkaline earth boro-aluminosilicate display glass (Corning Eagle XG, 50 mm × 50 mm × 0.7 mm) substrates by unbalanced dc MSD. The used deposition plant was an industrial-scale in-line sputter device (FHR.Line.600-V) with two chambers, i.e. a load-lock and a deposition chamber. Prior to the deposition, the substrates were cleaned in ultrasonic baths of acetone and ethanol and dried with hot air. After mounting the samples on the vertically positioned substrate carrier, the load-lock chamber was evacuated to a base pressure below $1 \cdot 10^{-4}$ Pa, while the deposition chamber was evacuated to a base pressure below $1 \cdot 10^{-5}$ Pa. After moving the substrate carrier into the deposition chamber, the substrates were first plasma etched for further cleaning. Subsequently, the substrate carrier was positioned in front of the cylindrical rotatable Mo target (diameter of 160 mm and length of 600 mm) at a target - substrate holder distance of about 75 mm. A constant power of 4 kW was applied to the target and the discharge voltage was recorded by the device's control software during deposition. The MoO_x films were grown without additional heating of the grounded substrate carrier in a reactive O_2/Ar atmosphere at an average total pressure of $p_{tot} = 0.1$ Pa. However, it should be noted that the substrates undergo a thermal ramp reaching 220-230 °C already after a deposition time of 6 min due to the energy delivered by the plasma to the substrates, as reported earlier [80]. To investigate the influence of the oxygen content on structure and properties of the deposited films, the oxygen partial pressure was varied between 0 and 100% during deposition, as shown in Table 7.1. The calculation of the oxygen partial pressure was done according to gas flow - pressure calibration curves recorded prior to the deposition runs using a Baratron MKS Type 627D capacitance manometer with an accuracy below 0.5% [81]. The deposition time was adjusted to synthesize films with a thickness of 3 ± 0.5 µm, which were used to investigate film growth and structure. In addition, films with a thickness of about 100 nm were deposited to analyse the optical and electrical properties.

Table 7.1: Variation of oxygen partial pressure $p(O_2)$ during deposition with $p_{tot} = 0.1$ Pa.

$p(O_2)/p_{tot}$ [%]	0	10	31	54	66	78	84	90	100
Ar flow [sccm]	100	80	60	40	30	20	15	10	0
O_2 flow [sccm]	0	20	40	60	70	80	85	90	100

Cross-section as well as top-view secondary electron images were taken with a Zeiss NTS Ultra-plus scanning electron microscope (SEM) with an acceleration voltage of 5 kV to analyse the coating structure. The chemical composition of the MoO_x films was measured with two different methods. On the one hand, elastic recoil detection analysis (ERDA) was performed using a 43 MeV Cl^{7+} ion beam. The angle between the sample normal and the incoming beam was 75°, the scattering angle was 31°. The analysed area was about 1.5 mm x 1.5 mm. The recoil ions have been detected with a Bragg Ionization Chamber using a full energy detection circuit for the ion energies and a fast timing circuit to obtain an atomic mass dependent signal to separate ion species. On the other hand, the films were analysed by electron probe microanalysis (EPMA) using wavelength-dispersive X-ray spectroscopy (WDS) with an electron energy of 10 keV and a current of 100 nA. The crystalline oxide phases present in the films were identified by X-ray diffraction (XRD) measurements with a Bruker-AXS D8 Advance diffractometer. The measurements were conducted in grazing incidence mode with a fixed angle of incidence of 2° and a step of detector movement of 0.02° with an accumulation time of 1.2 s. Cu-K_α radiation (wavelength: 0.154056 nm) and an energy-dispersive Sol-X detector from Bruker-AXS were used. The International Centre for Diffraction Data (ICDD) database was used as reference for phase identification [67]. Furthermore, Raman spectroscopy measurements were done with a HORIBA Jobin Yvon LabRam-HR800 confocal spectrometer equipped with a Nd:YAG laser (λ = 532.2 nm, 3.5 mW at the measuring spot) to confirm the results of the XRD measurements.

The X-ray photoelectron spectroscopy (XPS) measurements have been performed using a Theta Probe XPS system from Thermofisher and assessed by means of the Avantage software package provided by the manufacturer. A monochromatic Al-K_α X-ray beam (1486.6 eV) was used and operated at a voltage of 15 kV with an emission current of 6.7 mA (100 W). For all measurements, the maximum spot size of the X-ray beam of 400 µm in diameter was employed. The hemispherical analyser was operated in the constant analyser energy mode with constant pass energy of 50 eV (1.00 eV full width at half maximum on Ag $3d_{5/2}$). All spectra were acquired with an energy step size of 0.05 eV. In order to neutralize the charge build-up on the investigated surfaces, the XPS tool was equipped with a standard dual flood gun, which provides simultaneously a beam of low energy electrons, usually 2 eV, and a beam of low energy Ar-ions. Binding energies were calibrated to the common C 1*s* peak at 284.6 eV, which occurs due to the presence of adsorbed hydrocarbons at the sample surface. The base pressure of the ultra-high vacuum analysis chamber was held in the low range of 10^{-7} Pa prior to the analysis and, due to applied charge neutralization, in the low 10^{-5} Pa range during the data acquisition. All the samples have been measured as received, with no extra treatments for the sample preparation.

The reflectance and transmittance of the films deposited on soda lime glass substrates were measured using a Perkin Elmer Lambda 950 photo-spectrometer. The electrical properties of the films were measured in the van der Pauw geometry [82] at room temperature. The contacts on the samples were fabricated by direct gold wire bonding on their surface using a molten indium bonder. X-ray reflectivity was used for the absolute measurement of the thickness of the MoO_x films, employed for the resistivity calculations, and was performed using a Seifert XRD 3003 PTD-HR computer-controlled diffractometer.

7.3 Results

The evolution of the discharge voltage, the film growth rate and the chemical composition of the synthesized MoO_x films as a function of the oxygen partial pressure used during deposition are shown in Figure 7.1. With increasing $p(O_2)$ from 0 to ~70%, the discharge voltage rose from -375 to -600 V, while the film growth rate slightly increased from 275 to 350 nm/min. Simultaneously, the oxygen content increased from ~4 to ~75 at.%, while the Mo content decreased correspondingly. The comparison of EPMA/WDS (4 at.% O) and ERDA (0 at.% O) measurements indicates that EPMA overestimates the oxygen content in particular at low oxygen contents. The discharge voltage slightly decreased from -600 to -540 V with increasing oxygen partial pressure above 70%, while the film growth rate dropped to ~50 nm/min. The level of oxygen content was constant at ~75 at.%. In this compositional region, EPMA and ERDA measurements are in good agreement.

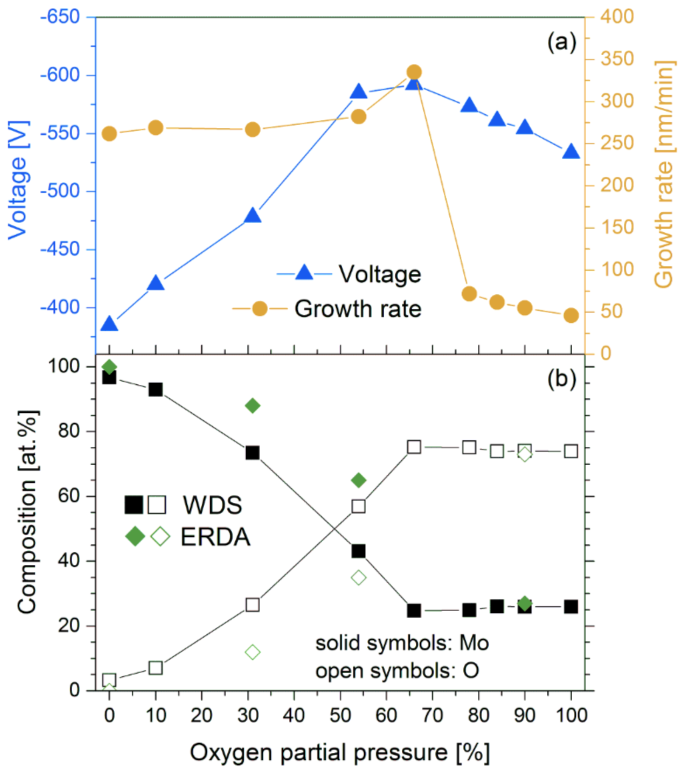

Figure 7.1: a) Discharge voltage and film growth rate as well as b) chemical composition of the synthesized MoO_x films as a function of the oxygen partial pressure.

In Figure 7.2 top-view as well as cross-section secondary electron SEM images of the synthesized MoO_x films as a function of the oxygen partial pressure used during deposition are presented. The Mo film deposited in pure Ar atmosphere (Figure 7.2a) as well as the MoO_x film deposited with $p(O_2)$ = 10% (Figure 7.2b) exhibit a well-defined columnar grain growth in cross-section and flat, elongated plate-like shaped grains in top view. The MoO_x films deposited with $p(O_2)$ = 31% and 54% (Figures 7.2c and d) show a featureless structure in cross-section, while the film with p(O_2) = 54% exhibits a grainy structure in top-view. The micrographs of the films with p(O_2) = 66% to 100% are similar (Figures 7.2e to i) with differently shaped and horizontally aligned flat and flaky crystals, where some of them form bundles of flat crystals growing in different directions and protrude like needles out of the surface. The cross-section images reveal a densely grown columnar structure. The structural sequence from crystalline via featureless amorphous to crystalline again is in good agreement with the structure zone model suggested by *Barna and Adamik* [66], where beside the temperature also impurities, in this case oxygen, affect film growth and microstructure evolution. Although the MoO_x films were deposited without external heating, the films with p(O_2) = 78 to 100% experienced enhanced temperatures as the deposition time was increased in order to compensate the lower film growth rate and to achieve a comparable film thickness. As a result of the longer exposure of the substrates to energetic particle bombardment and consequently higher substrate temperatures towards the later stage of the film growth process [80], the films deposited with p(O_2) = 78 to 100% show a structural evolution in cross-section from amorphous to crystalline (best seen in Figure 7.2e for p(O_2) = 66%). The high level of oxygen at considerably low substrate temperature results in a complete surface coverage of the formed nuclei, where their further growth is efficiently blocked causing continuous re-nucleation [66]. The amorphous region formed during the early film growth stage becomes smaller with increasing p(O_2), which also agrees well to the model suggested by *Barna and Adamik* [66].

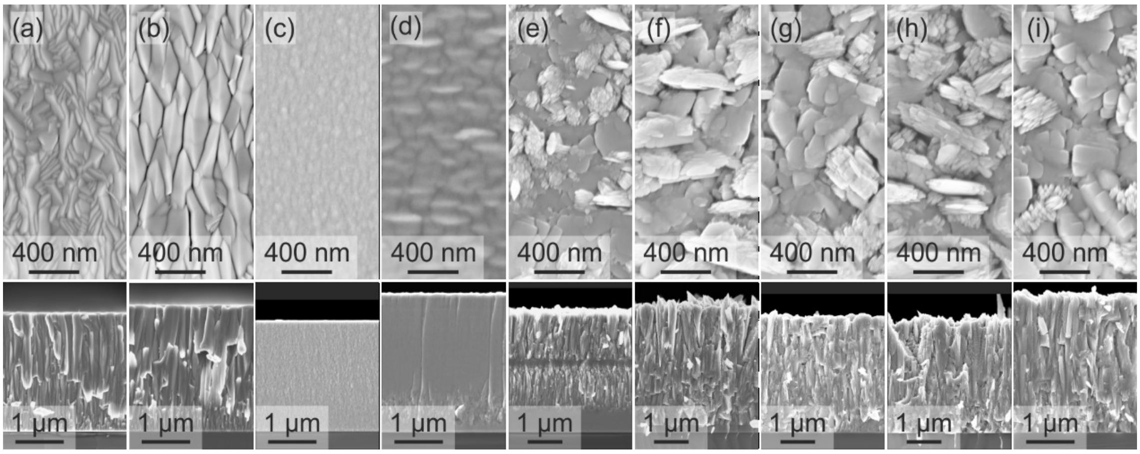

Figure 7.2: Top-view (upper row) and cross-section (lower row) secondary electron SEM images of the synthesized MoO_x films as a function of the oxygen partial pressure used during deposition: a) 0%, b) 10%, c) 31%, d) 54%, e) 66%, f) 78%, g) 84%, h) 90% and i) 100%.

The X-ray diffractograms of the MoO_x films grown with increasing oxygen partial pressure are illustrated in Figure 7.3a. The film with $p(O_2) = 0\%$ shows the expected body-centred cubic structure of metallic Mo. Further, also the film grown at $p(O_2) = 10\%$ exhibits a body-centred Mo phase, just with slightly broadened peaks; obviously the oxygen is incorporated within a Mo-based solid solution. The films with $p(O_2) = 31\%$ and 54% developed a less crystalline or even amorphous-like structure. Changing the oxygen partial pressure from 54% to 66% marks a turning point in terms of structure. These MoO_x films are dominated by the formation of an orthorhombic α-MoO_3 structure with fractions of monoclinic β-MoO_3 [34].

A validation of the phase identification based on the XRD measurements is supported by Raman spectroscopy of the MoO_x films as shown in Figure 7.3b. According to the XRD findings, the synthesized MoO_x films can be divided into two groups depending on the $p(O_2)$ used during deposition. The films with $p(O_2)$ up to 60% show broad bands of low intensity, which cannot be assigned unambiguously to specific MoO_x phases. These films are only weakly Raman active and present a nanocrystalline morphology. The MoO_x films deposited at $p(O_2) = 66\%$ and above show well-defined peaks in the Raman spectra. The films with $p(O_2) = 84$ to 100% fit well to the MoO_3 reference data. However, all the films of the second group show also small traces of triclinic Mo_9O_{26}.

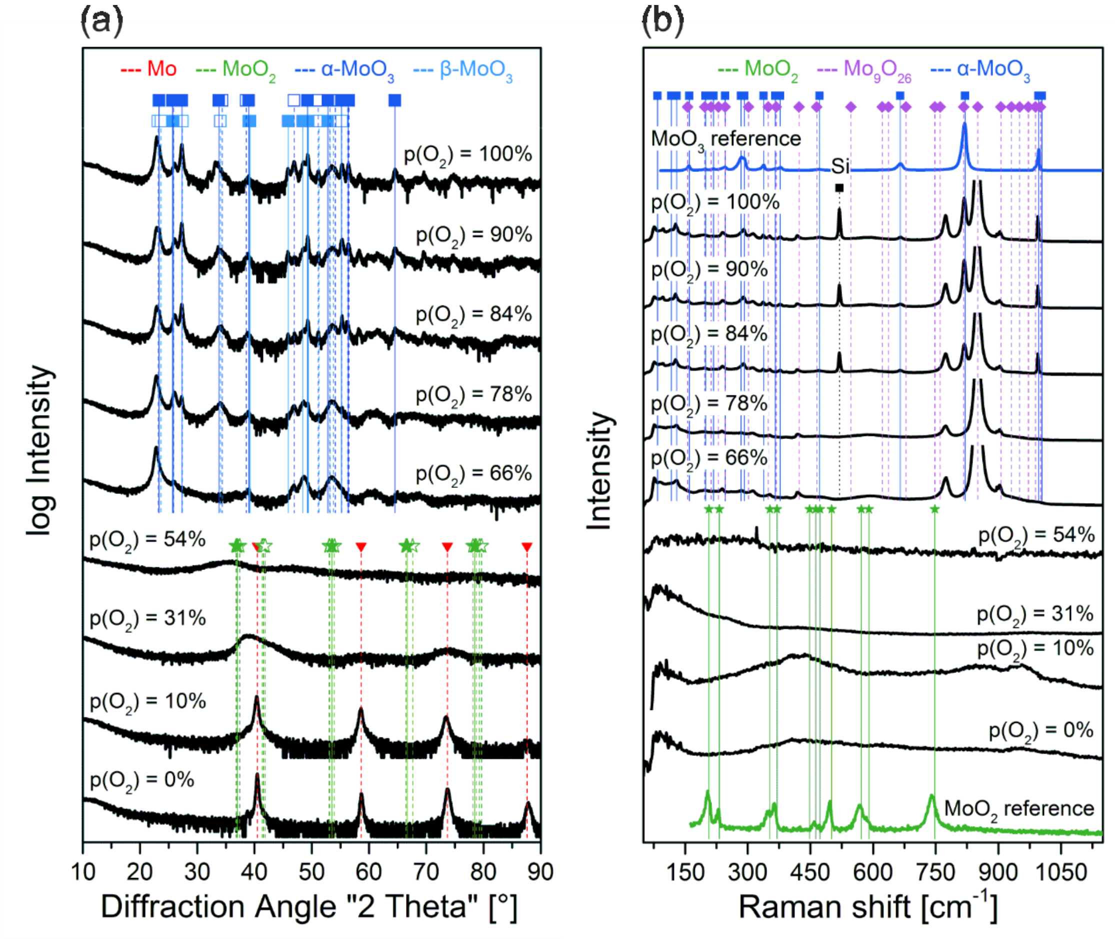

Figure 7.3: a) X-ray diffractograms and b) Raman spectra of the synthesized MoO_x films as a function of the oxygen partial pressure used during deposition (substrate: silicon). The XRD reference peak positions are according to Ref. [67] (solid symbols: high intensity peaks; open symbols: low intensity peaks). The Raman reference spectra of monoclinic MoO_2 and orthorhombic α-MoO_3 were taken from Ref. [68] and the reference peak positions of MoO_2, α-MoO_3 and Mo_9O_{26} from Ref. [38].

Further details on the bonding structure in the synthesized MoO_x films are provided by XPS as shown in Figure 7.4. Metallic bonds, as indicated by the slightly asymmetric Mo^0 peak in the Mo 3*d* core level spectra, can be found in films grown with $p(O_2)$ up to 66%. The oxidation state of MoO_2 (Mo^{4+}) exists up to $p(O_2) = 78\%$. An intermediate oxidation state, widely attributed in literature to Mo^{5+} [83–85], is present in all deposited MoO_x films, including also the pure Mo film due to native oxides and possible impurities originating from surface contamination taking place between deposition and measurements. In contrast, the Mo^{6+} state (MoO_3) is only present in the films deposited in O_2 containing atmosphere.

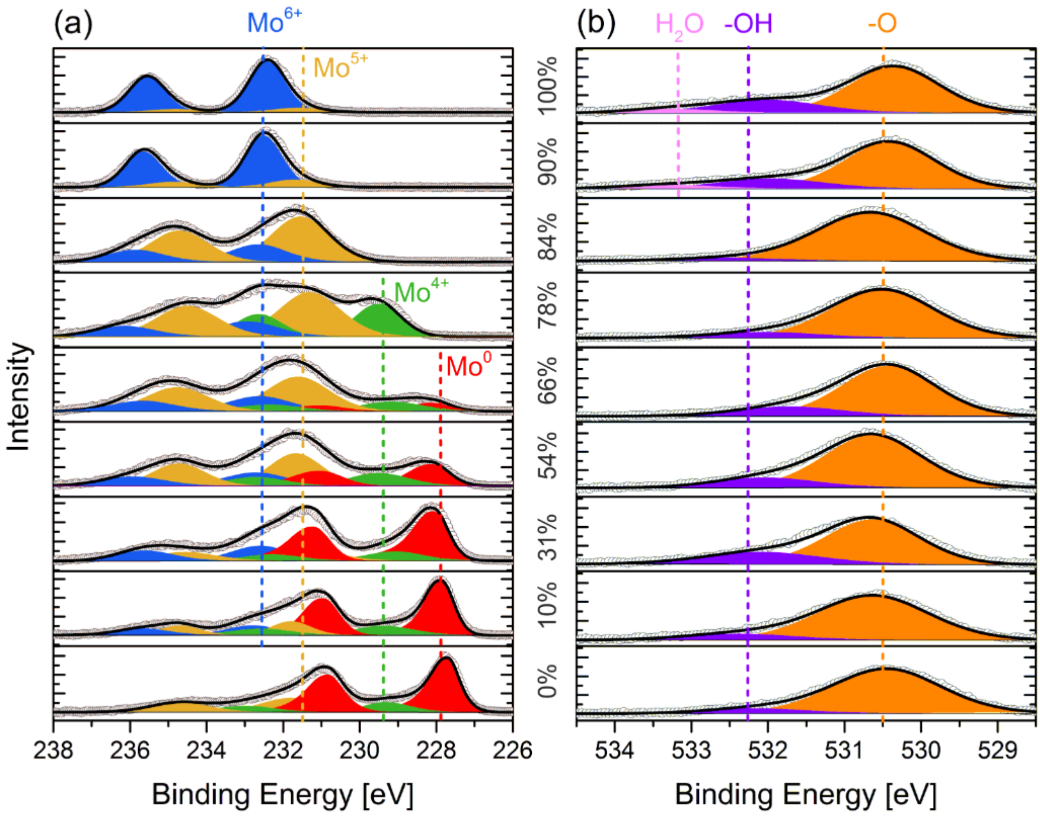

Figure 7.4: (a) XPS Mo 3*d* and (b) O 1*s* core-level spectra of the as-deposited MoO_x thin films as a function of the oxygen partial pressure. The assignment of the reference peak positions follows Refs. [83–86].

The normalized O 1*s* spectra show three different oxygen peaks (Figure 7.4b). The O-Mo bonding peak corresponds to the lower binding energy component. The energy separation between this main component and the Mo $3d_{5/2}$ peaks are included between 297.81 and 298.04 eV for Mo^{6+}, between 298.84 and 299.19 eV for Mo^{5+}, between 301.15 and 301.55 eV for Mo^{4+}, and between 302.33 and 302.76 eV for Mo^0. These values, which are not affected by any shift of the spectra due to charging effects, are used to identify the different oxidation states. A secondary oxygen peak with higher binding energy with respect to the O-Mo bonding peak is present in all the films investigated. This second oxygen peak can be attributed to chemisorbed -OH groups or to contributions from a defective oxide component inherent in these transition metal oxides surfaces [87,88]. Lastly, a third oxygen component at the highest binding energy values is found at the very surface of the films grown with $p(O_2)$ = 90 and 100% and it is assigned to adventitious oxygen from surface contamination.

In addition to the structural characterization of the synthesized MoO_x thin films, their optical properties reflectance, absorbance and transmittance have been analysed and are summarized in Figure 7.5. The metallic Mo film and the MoO_x films with $p(O_2)$ up to 31% exhibit the highest reflectance of about 55% (Figure 7.5a). On the other hand, the highest absorbance values between 50 and 80% are obtained for the films with $p(O_2)$ between 54 and 84% (Figure 7.5b). Furthermore, the two MoO_x thin films with the highest $p(O_2)$ of 90 and 100% show transmittance up to 50 and even 80%, whereas the transmittance values of the other films is 10% and below (Figure 7.5c).

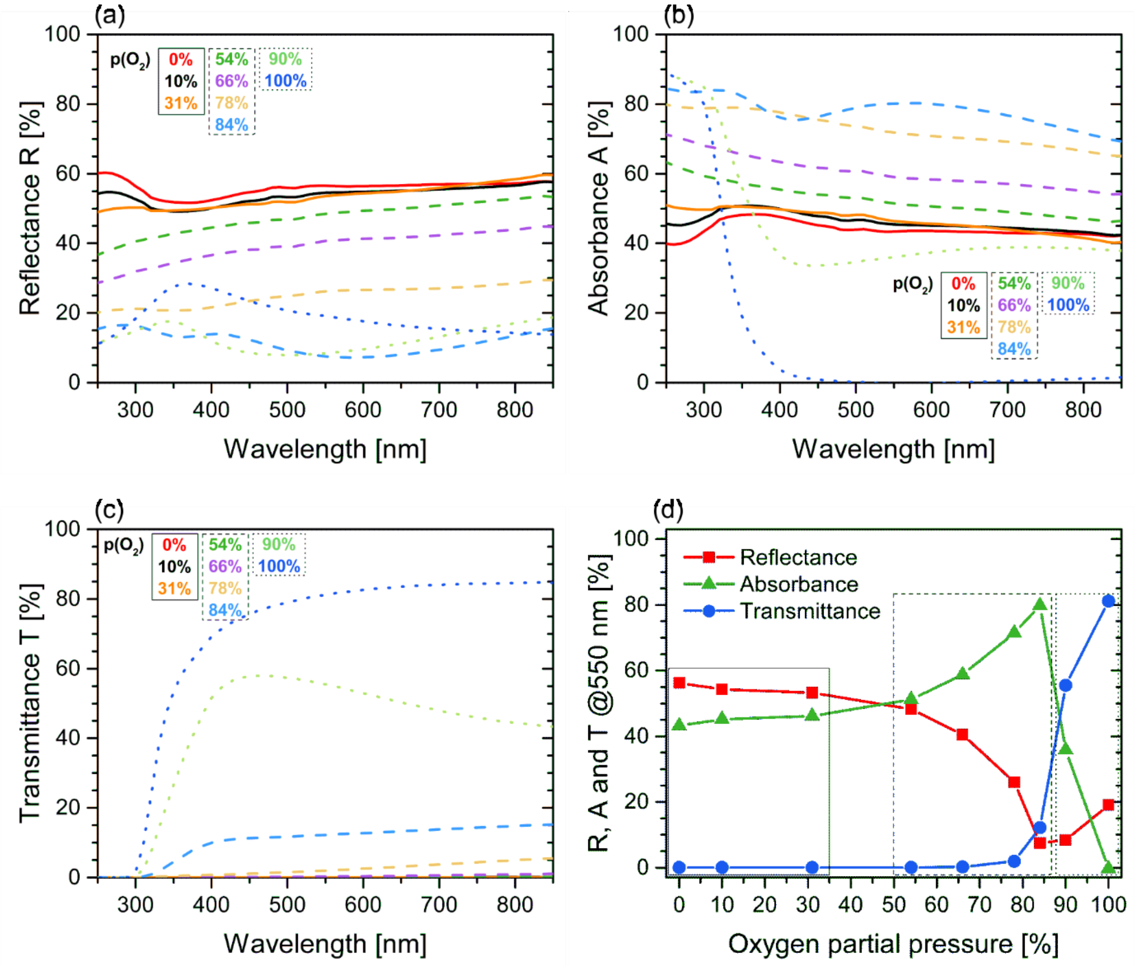

Figure 7.5: a) Reflectance R, b) absorbance A and c) transmittance T of ~100 nm thick MoO_x thin films as a function of the oxygen partial pressure. d) Overview of the optical properties determined at 550 nm, i.e. at the most pronounced sensitivity region of the human eye [89].

Measurements of the electrical resistivity of the samples indicated that the MoO_x films at room temperature change from electrically conductive to insulating for different $p(O_2)$ used during deposition, as illustrated in Figure 7.6. The resistivity value of the film deposited with $p(O_2) = 0\%$ is comparable to metallic Mo [8]. With increasing $p(O_2)$, the resistivity of the MoO_x films increases monotonically up to a value five orders of magnitude higher for the film deposited with p(O_2) = 90%, dominated by the Mo^{6+} cations, with respect to that obtained for the Mo and Mo dominated films. The sample grown at p(O_2) = 100% is characterized by an insulating behaviour, with values above 10^8 Ωcm, as expected for a fully oxidized MoO_3 thin film.[8]

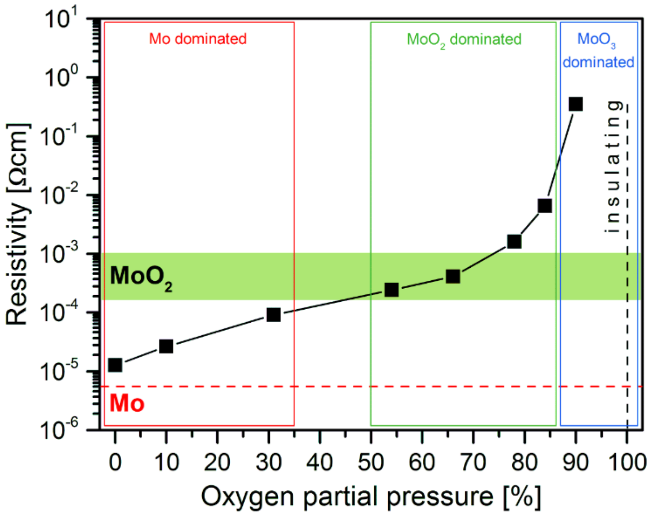

Figure 7.6: Electrical resistivity of the synthesized MoO_x thin films at room temperature as a function of the oxygen partial pressure used during deposition. Regions of different MoO_x based phases are indicated. Reference values of the electrical resistivity of Mo and MoO_2 from literature are also included [8,32,78].

7.4 Discussion

The evolution of chemical composition and microstructure of the deposited MoO_x films are comparable to a previous report [90], although two significantly different deposition systems were used. In our previous work [90], MoO_x films were synthesized using a lab-scale deposition system with two planar circular magnetrons (∅ 50 mm), whereas in this work an industrial-scale deposition plant with a cylindrical rotatable target (∅ 160 mm × 600 mm) was used for synthesis. Although the change in discharge voltage with increasing p(O_2) is similar for both processes, the film growth rate using the rotatable target is 5 to 6 times higher than for the small planar targets. This results in an extension of the metallic region to higher p(O_2) for the rotatable target, since a more intense flux of Mo atoms in relation to oxygen is available for film growth. In both cases, at high p(O_2) the transition to the compound or poisoned mode occurs, which is characterized by a reduction in discharge voltage and growth rate (Figure 7.1) and the formation of films dominated by the MoO_3 phase. However, for the planar targets used in Ref. [90] sputtering and poisoning of the target surface takes place simultaneously in the racetrack, leading to an equilibrium state and consequently an extended transition zone between metallic and poisoned mode. In the case of a rotatable target, the sputtering and poisoning processes are widely decoupled since only a fraction of the target surface is exposed to the plasma at a given time. The formation of oxides on the target surface can therefore occur on target areas that are outside the respective current racetrack, whereas the removal of them can only occur during the time the target surface area is bombarded by ions from the magnetron discharge. When this time is insufficient to remove the formed oxides, target sputtering is done in the poisoned mode. The transition between metallic and poisoned mode for a rotatable target is therefore considerably sharper than for a planar target. In the current case, this transition occurred at $p(O_2)$ values between 66 and 78%, while it was reported for 48 - 90% in the lab-scale device with planar targets used in our previous work [90]. Further details about effects influencing composition and microstructure of MoO_x thin films can also be found in this previous report [90]. In the following, we will therefore focus the discussion on the evolution of the optical and electrical properties of the deposited MoO_x thin films using ITO as a benchmark, in order to evaluate the suitability of MoO_x films as a TCO material system.

The Mo-O system is characterized by the formation of two stable oxides with well-known properties. These are on the one hand MoO_2, which is electrically conductive with a dark non-transparent appearance, and, on the other hand, MoO_3, the highest oxidized MoO_x, which is insulating with a yellowish transparent appearance [5–8]. Between these two oxides and metallic Mo, microstructure and properties of MoO_x films can be tuned by varying the $p(O_2)$ in the process gas during sputter deposition in order to obtain the required chemical composition and oxidation states of Mo (Figures 7.1 and 7.4). The presence of different oxidation states correlates well with the evolution of the electrical properties, where the role of oxygen vacancies, as *n*-type dopants by adding donor states within the band gap, leads to a decreasing resistivity. A characteristic feature of those films with dominating MoO_3 phase and main oxidation state Mo^{6+} is their high electrical resistance. With decreasing $p(O_2)$ values, chemical composition and microstructure first remain largely unaltered, but a mixture of the oxidation states, mainly Mo^{5+}, Mo^{4+} and Mo^0, develops which is associated with good electrical conductivity. In particular, resistivity values below $1 \cdot 10^{-3}$ Ωcm, typical for a metal-like behaviour [8], can be achieved when the oxidation state Mo^0 is well developed, which is the case for the metallic dominated MoO_x films ($x \leq 12$ at.%), but also for those that were synthesized in the transition between metallic and poisoned mode ($35 \leq x \leq 75$ at.%) with amorphous or MoO_3 phase structure. Such resistivity values are comparable to those obtained for ITO, where values between $6.8 \cdot 10^{-5}$ and $1.1 \cdot 10^{-3}$ Ωcm are reported depending on the growth conditions [18,91–95].

In terms of optical properties, the deposited MoO_x films can be divided into three groups according to their reflectance, absorbance and transmittance at the most pronounced sensitivity region of the human eye at 550 nm (see Figure 7.5d) [89]. The metallic MoO_x films with the lowest oxygen content up to 12 at.% O show with up to 55% the highest reflectance of all films investigated within this work and at the same time a corresponding high absorbance of about 45%. This metal-like appearance can be understood by the dominating Mo^0 oxidation state in the films. The films with amorphous or MoO_3 phase structure but dominating oxidation states Mo^{4+} and Mo^{5+} reveal a pronounced absorbance with a maximum of about 80%. The initially high reflectance decreases to values below 20% for rising oxidation states. The transmittance, however, remains low until the Mo^{6+} state becomes dominating for those films reaching an oxygen content of 75 at.%. The highest transmittance with about 80% (see Figure 7.5d) was observed for the Mo^{6+} dominated film deposited in pure O_2 atmosphere and such a value is close to the transmittance values of ITO reported in literature, which are in the range from 85 to 95% [95,96].

The current study shows the potential of MoO_x films to be used as TCOs, but also reveals that further work is necessary to elucidate the combination of optical and electrical properties that is required for TCO materials. For the MoO_x films deposited within this work, high optical transmittance and good electrical conductivity can be achieved; however, for different stoichiometries within the Mo-O system and not for a particular chemical composition. In order to combine both properties within one MoO_x film, either the border between absorbing and transparent MoO_x films needs to be shifted to lower oxygen contents while maintaining the good electrical conductivity or conducting mechanisms for the MoO_x films with high transmittance need to be explored. It is apparent that achieving this goal solely within the system Mo-O is unlikely, even though the system is very versatile in general, and, therefore, doping or alloying of MoO_x films is necessary to enable their use as TCOs in display applications for electronic devices.

7.5 Conclusions

Within this work, molybdenum oxide thin films were synthesized by reactive dc magnetron sputtering using an industrial-scale in-line deposition plant. The used rotatable Mo target was operated in an O_2/Ar atmosphere, where the oxygen partial pressure was systematically varied. With oxygen partial pressure increasing from 0 to 100%, the film growth rate decreased from 350 to 50 nm/min. The synthesized films vary in composition, microstructure and properties between a metallic Mo-based solid solution, a MoO_2- and higher oxidized molybdenum oxides dominated phase composition and a MoO_3 dominated structure. The phase evolution is reflected by the optical properties of the films, which range from reflective via absorbent to transparent, and the electrical properties, which vary between electrically conductive through semi-conductive and insulating. This wide range of film characteristics demonstrates that microstructure and properties of the deposited molybdenum oxide thin films can be tuned by adjusting the O_2/Ar ratio in the process gas during deposition, opening wide perspectives for molybdenum oxide based thin films for optical and electronic devices.

8 NON-REACTIVE DC MAGNETRON SPUTTER DEPOSITION OF MoO_x THIN FILMS FROM CERAMIC MOLYBDENUM OXIDE TARGETS

8.1 Introduction

Thin films, especially oxide-based materials, for opto-electronics (e.g. solar cells, displays, electrochromic glasses) have gained increasing importance during the last decade. For such applications, film properties like excellent electrical conductivity and high optical transparency are required. Nowadays, such aligned properties are mainly realised by a certain group of metal oxides [1], the so-called transparent conducive oxides (TCO). The most frequently applied TCO materials are aluminium doped zinc oxide (AZO) [2,3] and tin doped indium oxide (ITO) [4]. In particular, ITO is widely and successfully used for industrial applications, but its major drawback is the high world market price of indium due to its limited availability. The demand for alternative TCO materials rises and moreover, to keep up with the rapid developments in the targeted high-tech sector, the material systems need to be easily adaptable to changing technological demands.

Alloying or doping as well as changing the stoichiometry can be used for tuning the properties of oxides. This work focuses on the binary Mo-O system as a potential alternative material system to ITO. The oxidation states of molybdenum oxides (MoO_x) strongly define their optical and electrical properties. They range from metallic-like electrical conductive behaviour and non-transparent appearance for the lowest oxidation state (MoO_2; Mo^{4+}) to electrically insulating behaviour and transparent appearance for the highest oxidation state (MoO_3; Mo^{6+}). Between these two thermodynamically stable oxides, several intermediate MoO_x like Magnéli phases with varying optical and electrical properties were reported [5–8]. While the lower oxidised MoO_x phases remain largely unexplored for thin film applications so far, MoO_3 films have proved to be successful in different industrial sectors like photochromic [9,10] and electrochromic glasses [9], gas sensors [11], and photovoltaics [12]. Such material systems are synthesised for example by sol-gel [18–20], printing [17], chemical vapour deposition [18,21,22] or, most commonly used, physical vapour deposition techniques with magnetron sputter deposition (MSD) in particular [18,23,24]. With the latter, oxide thin films are typically synthesised by a reactive MSD process, where a reactive gas (typically O_2) is added to the working gas during deposition [25]. Varying the partial pressure of the reactive gas leads to varying stoichiometry of the resulting films and therefore to versatile and tuneable properties [26].

The formation of chemical compounds between the reactive gas molecules adsorbed on the substrate and the impinging target atoms is responsible for film growth of such oxides. Simultaneously, compounds will be formed on the target surface, which affects the sputter behaviour towards lower sputter and growth rates, as a result of their usually lower conductivity. This behaviour is called target poisoning [27]. For large area coating processes, reactive MSD can be challenging due to a lack of homogeneously distributed reactive gas during deposition and consequently hardly controllable target poisoning; thus, films with locally varying thickness, compositions, microstructures and properties may be formed. Besides the investigation of a possible alternative to ITO, this work focuses on an alternative non-reactive MSD process. Thus, MoO_x films were synthesised non-reactively in pure Ar atmosphere from ceramic MoO_x targets with various compositions. Besides the investigation of microstructure-property relationships for the synthesised films, the correlation between synthesis conditions and film structure and properties was explored.

8.2 Experimental Details

The MoO_x films were grown by unbalanced dc MSD on (100)-oriented silicon (15 mm × 15 mm × 0.35 mm), soda lime glass (50 mm × 50 mm × 1 mm) and alkaline earth boro-aluminosilicate display glass (Corning Eagle XG, 50 mm × 50 mm × 0.7 mm) substrates. The used deposition system was a laboratory-scale AJA ATC-1800 UHV deposition device equipped with four circular planar targets (∅ 76 mm). Prior to the deposition, the substrates were cleaned in ultrasonic baths of acetone and ethanol and dried with hot air. After mounting the substrates on the rotating substrate holder (~30 rpm; target-substrate distance ~160 and ~90 mm for 150 and 450 W deposition power, respectively; all targets focused symmetrically to substrate holder), the deposition chamber was evacuated to a base pressure below $5 \cdot 10^{-5}$ Pa. A constant power of either 150 W or 450 W, was applied to the targets and the discharge voltage and current were recorded by the device's control software during deposition. The MoO_x films were grown non-reactively in pure Ar atmosphere at an average pressure of 0.5 Pa from two ceramic MoO_x targets (diagonally arranged, with the other two magnetrons not in use) of the same composition without external heating of the grounded substrate holder. The targets were prepared by powder metallurgical methods with compositions of $MoO_{2.5}$, $MoO_{2.6}$, $MoO_{2.7}$, and $MoO_{2.8}$. Films with a thickness of 1 - 1.5 µm for investigating film growth and microstructure as well as ~100 nm for analysing the optical and electronic properties were synthesised by adjusting the deposition time.

The morphology and topography of the films was characterised by cross-section as well as top-view secondary electron images taken with a Zeiss NTS Ultra-plus scanning electron microscope (SEM) with an acceleration voltage of 5 kV. The chemical composition of the films was measured by energy dispersive X-ray spectroscopy (EDS) with an Octane Plus silicon drift detector connected to the SEM.

Phase identification was done by three different methods. First, X-ray diffraction (XRD) measurements with a Bruker-AXS D8 Advance diffractometer equipped with an energy-dispersive Sol-X detector in grazing incidence mode were conducted using the following parameters: Cu-K_α radiation (wavelength: 0.154056 nm), fixed angle of incidence of 2° and a step of detector movement of 0.02° with an accumulation time of 1.2 s. As reference for phase identification the database of the International Centre for Diffraction Data (ICDD) was used [67]. Second, Raman spectroscopy measurements were done with a HORIBA Jobin Yvon LabRam-HR800 confocal spectrometer equipped with a Nd:YAG laser (wavelength: 532.2 nm, power: 3.5 mW at the measuring spot). Furthermore, a Theta Probe X-ray photoelectron spectroscopy (XPS) system from Thermofisher and the associated Avantage software package was used to support the results of XRD and Raman spectroscopy measurements. For all XPS measurements, the maximum spot size of the monochromatic Al-K_α X-ray beam (1486.6 eV, operated at a voltage of 15 kV and an emission current of 6.7 mA (100 W)) of 400 µm in diameter was used. The hemispherical analyser was operated in the constant analyser energy mode with constant pass energy of 50 eV (1.00 eV full width at half maximum on Ag $3d_{5/2}$). All measurements were conducted with an energy step size of 0.05 eV. A standard dual flood gun equipped to the XPS tool, which provides simultaneously a beam of low energy electrons (usually 2 eV) and a beam of low energy Ar ions, was used to neutralise the charge build-up on the investigated surfaces. Prior to the analysis, the ultra-high vacuum analysis chamber was held in the low pressure range of 10^{-7} Pa, while the pressure increased to the low 10^{-5} Pa range during measurements due to applied charge neutralisation. All samples were measured as received without any sample preparation and the binding energies were calibrated to the common C 1*s* peak (284.6 eV), which occurs at the sample surface due to adsorbed hydrocarbons.

A Perkin Elmer Lambda 950 photo-spectrometer was used to measure the reflectance and transmittance of the deposited films on soda lime glass substrates. The electrical properties were measured at room temperature in the van der Pauw geometry [82]. Direct gold wires were bonded with indium on the surface to contact the samples. The film thickness for the resistivity calculations was determined by a Veeco Dektak 150 Surface Profilometer.

8.3 Results and Discussion

In order to investigate the influence of the used deposition power on the microstructure as well as on optical and electrical properties, two series of MoO_x films were synthesised with powers of 150 and 450 W, respectively, applied to each target. Figure 8.1 illustrates the film growth rate for different deposition powers depending on the O/Mo target atomic ratio x. While the growth rate is with 14±1 nm/min nearly constant for 150 W, it is with 78±4 nm/min considerably higher for 450 W. The factor of 3 in deposition power between 150 and 450 W would give rise to an expected three times higher growth rate for the higher deposition power. However, the in fact significantly higher growth rate for 450 W, exceeding the factor of 3, can be understood by the reduced target-substrate distance of ~90 mm as compared to ~160 mm in the case of 150 W.

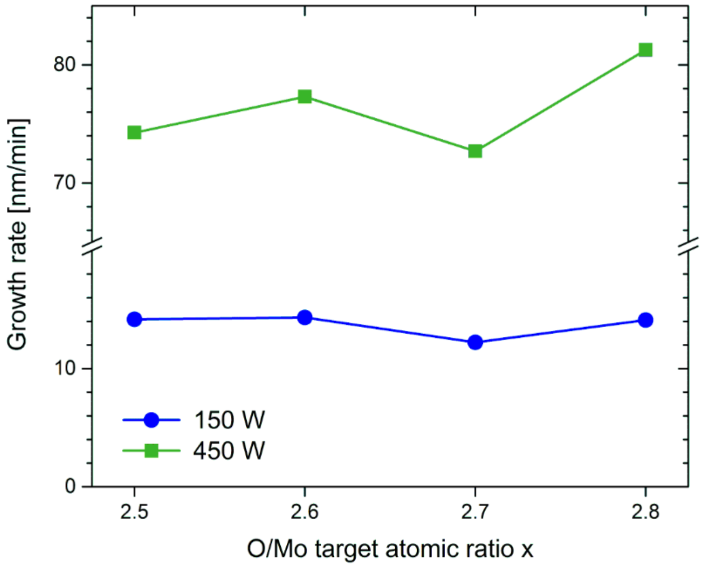

Figure 8.1: Film growth rate depending on the O/Mo target atomic ratio x for deposition powers of 150 and 450 W, respectively.

Figure 8.2 depicts the chemical composition of the films for different deposition powers depending on the O/Mo target atomic ratio x. Both film series exhibit the same trend of slightly increasing oxygen content for increasing O/Mo target atomic ratios with similar values for both deposition powers. In general, the measured O/Mo film ratio is by ~10 % lower than the target ratio, widely independent of the used deposition power. This oxygen loss might stem from the considerable mass difference of the film forming species (Mo, O) and the thus different scattering behaviour during the transport through the gas discharge, as it was observed for similar combinations of light and heavy elements in literature, e.g. TiW [97–104], MoSi [105,106], TiSi and WSi [105], WB [107], SiC [108], NbC [109], and TiB [110,111]. Element-specific scattering can be assumed to be more pronounced for the lighter oxygen compared to the heavy molybdenum atoms. This notion is fostered by *Neidhardt et al.* [112], who reported that the Ti/B atomic ratio in films sputter deposited using Ti-B targets increased linearly with increasing target-substrate distance with respect to the target composition. Experiments and simulations in Ref. [112] confirm the loss of the lighter B due to scattering, being in good agreement to the observed O loss in the synthesised MoO_x films. Figure 8.2 also indicates that the measured O content within the MoO_x films is slightly higher for the series grown at 450 W and the lower target-substrate distance, which confirms the element- and geometry-specific scattering suggested by *Neidhardt et al.* [112].

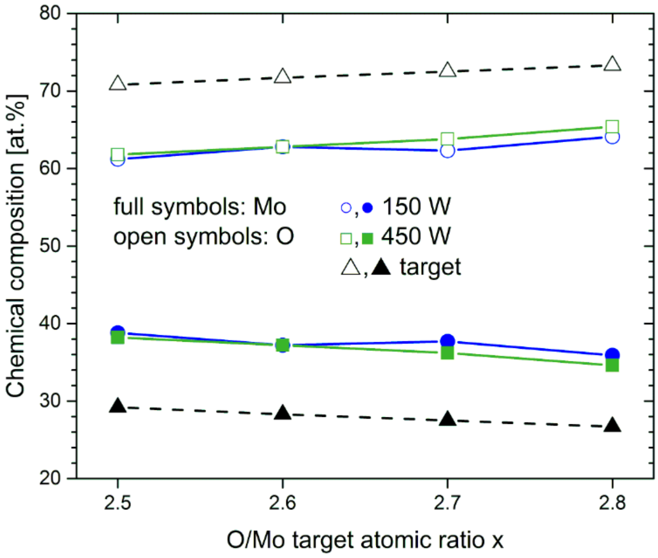

Figure 8.2: Chemical composition of the synthesised MoO_x films as a function of the O/Mo target atomic ratio x for deposition powers of 150 W (blue) and 450 W (green), respectively. The target composition (black) is included for comparison.

The bonding structure within the films was investigated by XPS. Representative core-level spectra are presented in Figure 8.3 for the film series grown at 150 W. All four films exhibit three oxidation states, i.e. Mo^{4+} (MoO_2), an intermediate one, widely attributed in literature to Mo^{5+} [38,83–85], and Mo^{6+} (MoO_3). The fraction of Mo^{4+} decreases with increasing O/Mo target atomic ratio x and corresponds to the increasing oxygen content measured within the films. The normalised O 1*s* spectra exhibit three different oxygen peaks, as shown in Figure 3b. The lower binding energy component is represented by the O-Mo bonding peak. The energy separation between this main component and the Mo $3d_{5/2}$ peaks are included between 297.81 and 298.04 eV for Mo^{6+}, between 298.84 and 299.19 eV for Mo^{5+}, and between 301.15 and 301.55 eV for Mo^{4+}. Since the spectra are not shifted due to charging effects, these values were used to identify the different Mo oxidation states. A second oxygen peak at higher binding energy, which can be attributed to chemisorbed -OH groups or to contributions from a defective oxide component inherent in these transition metal oxides surfaces [86,87], is present in all four films. At last, a third oxygen component can be attributed to adventitious oxygen from surface contamination.

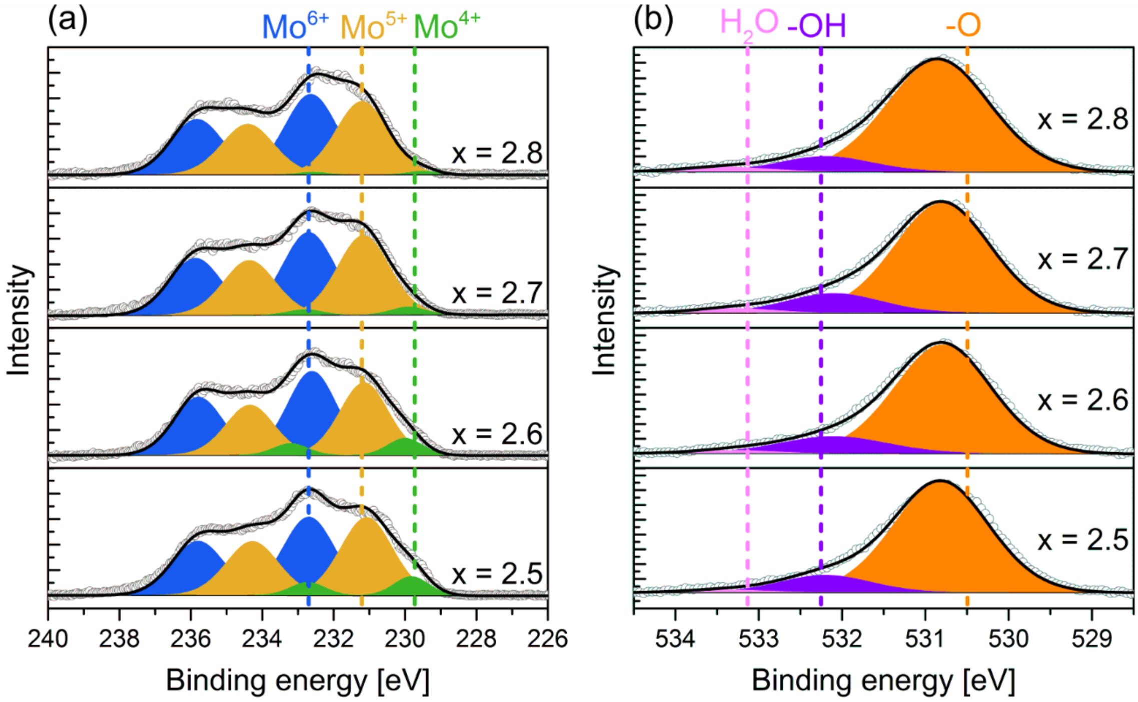

Figure 8.3: a) XPS Mo 3d and b) O 1s core-level spectra of the as-deposited MoO_x films as a function of the O/Mo target atomic ratio x for a deposition power of 150 W. The assignment of the reference peak positions follows Refs. [38,83–85].

Since the used deposition power has only a minor influence on the film composition (see Figure 8.2), the focus is laid in the following on those films deposited with the higher deposition power (450 W). Although the synthesised films exhibit a rather high thickness of at least 2 µm, they display a featureless morphology, as evidenced by the secondary electron SEM images in top-view and cross-section. The formation of this featureless morphology can be explained by the model suggested by *Barna and Adamik* [66]. There, the constant high flux of oxygen originating from the targets at considerably low substrate temperature fosters an efficient surface coverage of the formed nuclei. This surface coverage may block further growth by continuous re-nucleation leading to extremely fine-grained or even amorphous films. This interpretation is also corroborated by XRD, confirming the amorphous structure of the synthesised MoO_x films (Figure 8.5).

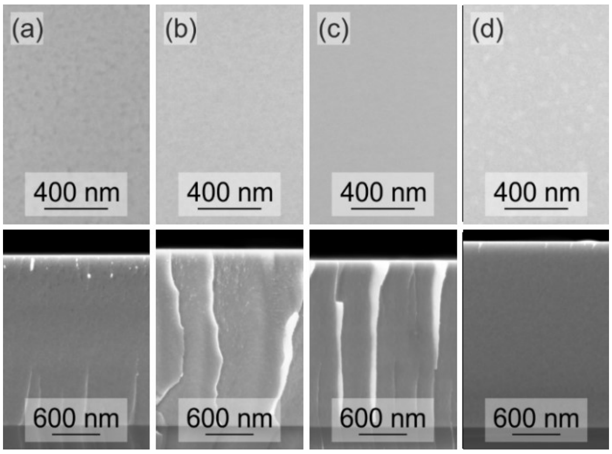

Figure 8.4: Top-view (upper row) and cross-section (lower row) secondary electron SEM images of the synthesised MoO_x films as a function of the O/Mo target atomic ratio x for a deposition power of 450 W: a) $MoO_{2.5}$, b) $MoO_{2.6}$, c) $MoO_{2.7}$, and d) $MoO_{2.8}$.

To confirm the chemical bond structure determined by XPS, Raman spectroscopy measurements were done and are summarised in Figure 8.6. The sequence of the films with increasing oxygen content exhibits an evolution in microstructure corresponding to the increase of the O/Mo target atomic ratio x. Phase fractions of Mo_4O_{11} and Mo_9O_{26} can be observed for all films investigated and are more pronounced for a higher O/Mo target atomic ratio x. This coincides with the decrease of the Mo^{4+} fraction observed by XPS.

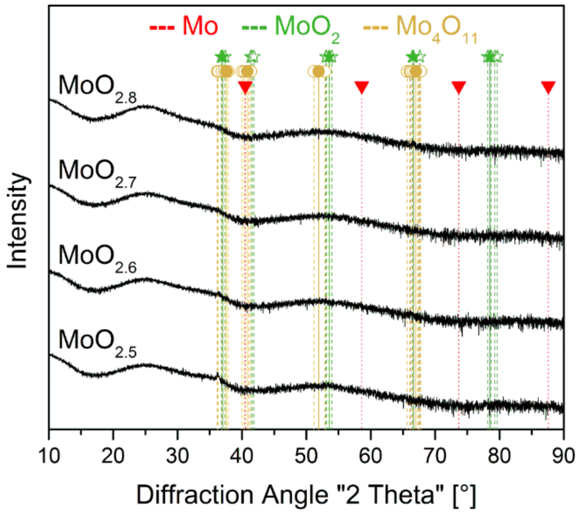

Figure 8.5: X-ray diffractograms of the synthesised MoO_x films as a function of the O/Mo target atomic ratio x for a deposition power of 150 W (substrate: soda lime glass). The reference peak positions are according to Ref. [67].

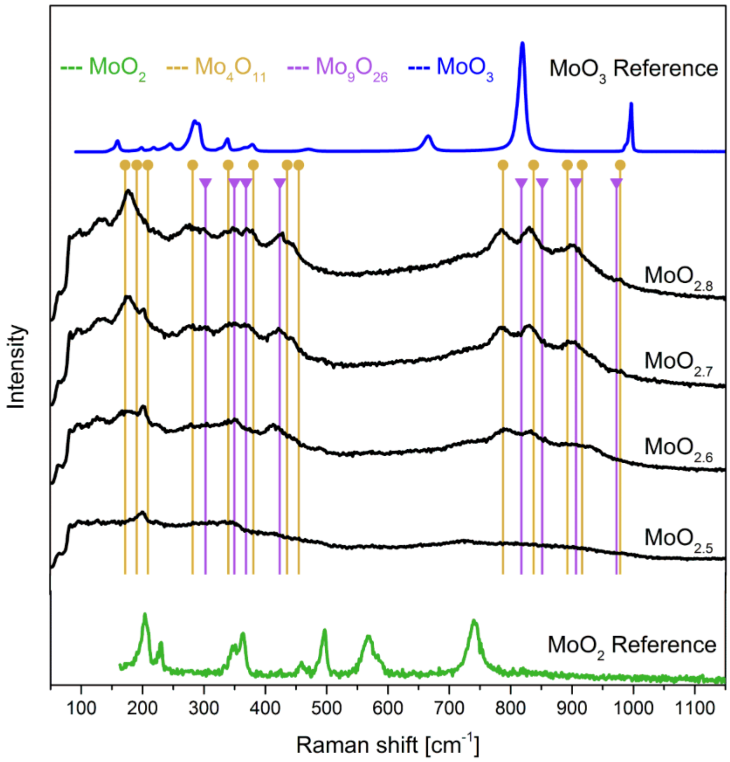

Figure 8.6: Raman spectra of the synthesised MoO_x films as a function of the O/Mo target atomic ratio x for a deposition power of 450 W (substrate: silicon). The reference spectra of MoO_2 and MoO_3 were taken from Ref. [68] and the reference peak positions of Mo_4O_{11} and Mo_9O_{26} from Ref. [38]. To enhance legibility, only the dominating peaks are indexed.

The synthesised MoO_x films were characterised with respect to their opto-electronic properties by photo-spectrometry and electrical resistivity measurements. The reflectance, absorbance and transmittance of the MoO_x films are summarised in Figure 8.7. Figure 8.7d provides an overview of the optical properties determined at a wavelength of 550 nm, i.e. at the most pronounced sensitivity region of the human eye [89]. Beside a low reflectance of 12±2% at 550 nm, the films exhibit absorbance values decreasing from 73 to 55% with decreasing Mo^{4+} fraction. In contrast, the transmittance increases from 14 up to 34%.

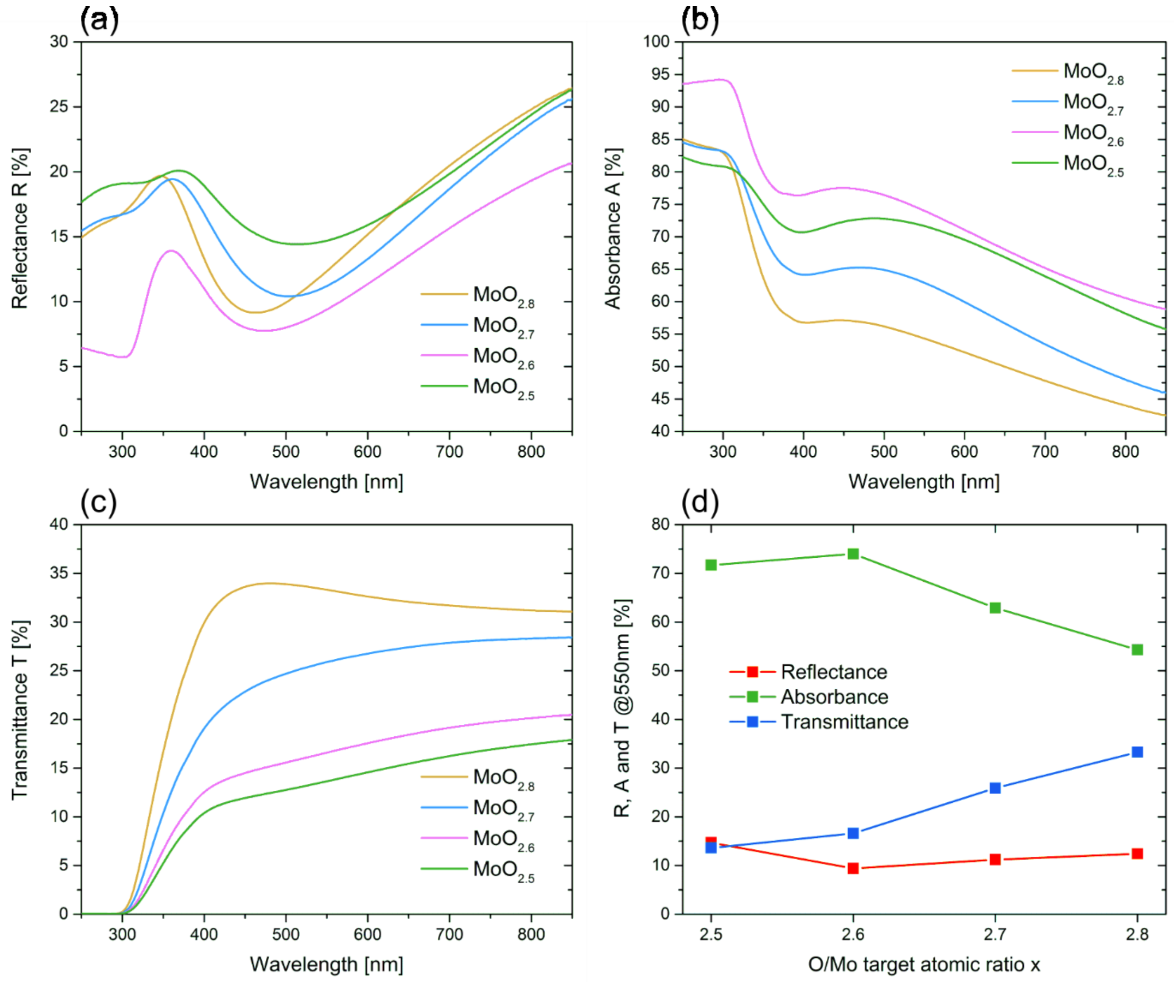

Figure 8.7: a) Reflectance R, b) absorbance A, and c) transmittance T of the synthesised MoO_x films as a function of the O/Mo target atomic ratio x for a deposition power of 450 W (film thickness: ~100 nm). d) Overview of the optical properties determined at the most pronounced sensitivity region of the human eye (~550 nm) [89].

Measurements of the electrical resistivity of the synthesised MoO_x films at room temperature (Figure 8.8) indicate a semiconducting behaviour, where the determined values are comparable to those reported in literature for intermediate MoO_x phases [6,8,39]. The resistivity increases by two orders of magnitude from 10^{-2} to 1 Ωcm.

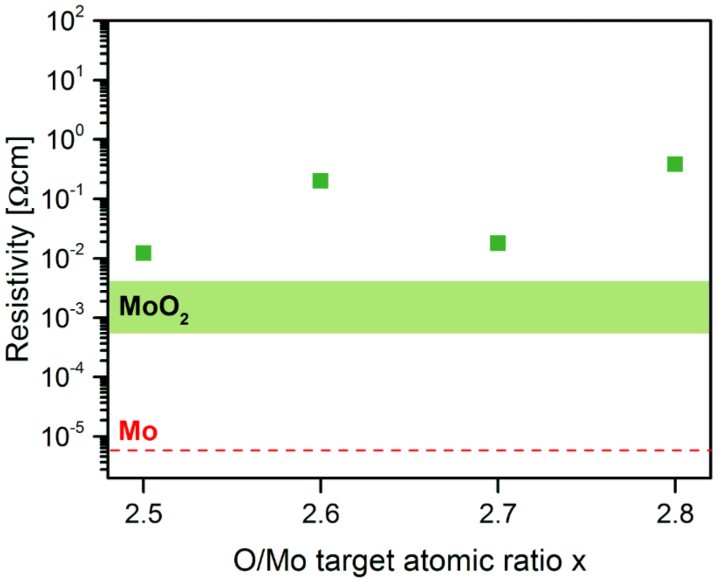

Figure 8.8: Electrical resistivity of the synthesised MoO_x films as a function of the O/Mo target atomic ratio x for a deposition power of 450 W. Reference values for metallic Mo and MoO_2 from literature are also included [8,38,83].

In the following, the determined values characterising the opto-electronic properties of the synthesised MoO_x films are compared to those of ITO, with the goal to illuminate their potential as an alternative TCO material. Literature values for ITO range from 85 to 95% for the transmittance and resistivity values vary between $6.8 \cdot 10^{-5}$ and $1.1 \cdot 10^{-3}$ Ωcm, depending on the growth conditions [91–94]. Since the transmittance of the herein synthesised MoO_x films is below 35% and the resistivity is higher than 10^{-2} Ωcm, these MoO_x films do not fulfil the requirements as ITO replacement. However, the synthesised MoO_x films could be used for other applications, e.g. as low-reflectance and electrically conductive films for bridge metallisation in touch sensors to enhance the visual performance or for solar cells [113–115]. There, reflectance should be below 10% and as the electrical current only has to pass thin films with thicknesses in the 50-200 nm range, there is no need for very low resistivity values [113–115]. Both requirements are satisfied for the synthesised MoO_x films, which makes them potential candidates for such low-reflectance films.

8.4 Conclusions

Within this work, molybdenum oxide thin films were synthesised by non-reactive dc magnetron sputter deposition using ceramic molybdenum oxide targets. Four different target compositions with O/Mo target atomic ratios ranging from $MoO_{2.5}$ to $MoO_{2.8}$ were used for two series of films synthesised with deposition powers of 150 and 450 W. The correlation between synthesis conditions and microstructure-property relationships was investigated. The films are dominated by Mo^{4+} (MoO_2), an intermediate oxide state Mo^{5+}, and Mo^{6+} (MoO_3), whereas the fraction of Mo^{4+} decreases with increasing O/Mo target atomic ratio. In general, all films exhibit a lower oxygen content than the target, most probably as a result of element-specific scattering during the transport of the sputtered species through the gas discharge during synthesis. The phase evolution is accompanied by increasing transmittance and decreasing absorbance, while the reflectance values are nearly constant. The resistivity values correspond to the semi-conductive range. While commonly molybdenum oxide films are synthesised by reactive dc magnetron sputter deposition from metal targets, the use of oxide targets offers an efficient and reliable process alternative and might thus enable their use in a wide range of opto-electronic applications.

9 SUMMARY AND CONCLUSIONS

Within this thesis, thin films within the binary Mo-O system were investigated with respect to their microstructure-property relationships. For this purpose, different MoO_x powders were investigated with respect to their powder characteristics and thermal stability for their suitability for sintering ceramic MoO_x sputter targets. In addition, a survey of the present understanding of the Mo-O system and the relevant MoO_x phases including their crystallographic structures and optical, electrical and mechanical properties was done. Moreover, MoO_x thin films were synthesised by different dc magnetron sputter deposition processes and correlations between synthesis conditions and microstructure-property relationships were investigated.

9.1 Reactive dc magnetron sputter deposition

MoO_x films were synthesised reactively in varying O_2/Ar atmospheres in a laboratory-scale dc sputter deposition system (equipped with circular planar Mo targets) as well as in an industrial-scale dc sputter deposition plant (equipped with a rotatable Mo target). Basically similar deposition conditions were used for both series - oxygen partial pressure increasing from 0 to 100%, constant power supplied to the target, grounded substrates, no external heating - with corresponding results. In general, for reactive sputtering the so-called target poisoning usually occurs for high partial pressures of reactive gas, where the film growth rate decreases due to target surface covering with less conductive compounds. Within this thesis it was observed that for MoO_x first the growth rate slightly increases with increasing oxygen partial pressure due to formation of still conductive oxide phases. With further increasing oxygen partial pressure and therefore the formation of insulating MoO_3, the growth rate decreases drastically. The synthesised films vary in composition, microstructure and properties between a metallic Mo-based solid solution, a MoO_2- and higher oxidised MoO_x dominated phase composition, and a MoO_3 dominated structure. The phase evolution is reflected by the optical properties of the films, which range from reflective via absorbing to transparent, and the electrical properties, which vary between electrically conductive through semi-conductive to insulating. This wide range of film characteristics demonstrates that microstructure-property relationships of MoO_x thin films can be tuned by adjusting the O_2/Ar ratio in the process gas during deposition. Moreover, the similar results obtained for both deposition series reveal a successful upscaling from laboratory- to industrial-scale deposition systems. This flexibility in microstructure, properties and synthesis process may evidence wide future perspectives for MoO_x-based films for opto-electronic applications.

9.2 Non-reactive dc magnetron sputter deposition

As an alternative synthesis process to MoO_x films sputtered reactively from a metallic Mo target, MoO_x films were additionally synthesised by non-reactive dc magnetron sputter deposition using ceramic MoO_x targets developed by powder-metallurgical methods. The used ceramic MoO_x targets with O/Mo target atomic ratios ranging from $MoO_{2.5}$ to $MoO_{2.8}$ were produced by spark plasma sintering. The powder characteristics (particle size, mixing conditions) as well as sintering parameters (temperature, pressure, time) were evaluated and optimized prior to using the targets for film synthesis. The correlation between synthesis conditions and microstructure-property relationships was investigated for two different deposition powers, i.e. 150 and 450 W, respectively. The films are dominated by Mo^{4+} (MoO_2), an intermediate oxide state Mo^{5+}, and Mo^{6+} (MoO_3), where the fraction of Mo^{4+} decreases with increasing O/Mo target atomic ratio. The evolution of microstructure and chemical composition is widely independent of the used deposition power. In general, all films exhibit a lower oxygen content than the target composition, most probably due to element-specific scattering during the transport of the sputtered species from the target to the substrate. The films exhibit a high optical absorbance and low reflectance combined with a semi-conductive behaviour. The use of ceramic MoO_x targets instead of metallic Mo targets for synthesising MoO_x films offers an efficient and reliable process alternative for thin film deposition and might thus enable their use in a wide range of opto-electronic applications.

9.3 Outlook

Within this thesis it could be shown that, on the one hand, the microstructure and properties of MoO_x films can be tuned by adjusting the oxygen partial pressure during deposition. On the other hand, non-reactive dc magnetron sputter deposition from ceramic MoO_x targets provides a stable process alternative to commonly used reactive sputter deposition processes, where difficulties arising from target poisoning could be avoided. A possible further development would be the combination of ceramic MoO_x targets with a reactive dc magnetron sputtering process to fine-adjust the films’ stoichiometry. First promising experiments within this thesis indicate that the desired microstructure and properties of the MoO_x films can be achieved by lower values of oxygen partial pressure when using a ceramic MoO_x target instead of a metallic Mo target for reactive sputtering. However, for possible applications a more precise adjustment of the chemical as well as phase composition is necessary. Moreover, the efficiency of thin film synthesis should be further improved by the development of cylindrical MoO_x targets, where new target processing routes (e.g. thermal spraying) have to be established. The combination of adjustable chemical structure and properties with flexible film synthesis processes makes the Mo-O system an interesting and promising material system for a wide range of optical and electronic devices.

10 REFERENCES

[1] **H.K. Pulker**, *Coatings on Glass*, Elsevier, Amsterdam, 2nd ed., 1999.

[2] **T. Minami**, *Present status of transparent conducting oxide thin-film development for indium-tin-oxide (ITO) substitutes*, Thin Solid Films 516 (17), pp. 5822–5828, 2008.

[3] **T. Minami**, *Substitution of transparent conducting oxide thin films for indium tin oxide transparent electrode applications*, Thin Solid Films 516 (7), pp. 1314–1321, 2008.

[4] **C.G. Granqvist, A. Hultaker**, *Transparent and conducting ITO films: new developments and applications*, Thin Solid Films 411, pp. 1–5, 2002.

[5] **L. Kihlborg**, *The structural chemistry of the higher molybdenum oxides*, Ark. För Kemi 21 (44), pp. 471–495, 1963.

[6] **L. Kihlborg**, *Studies on molybdenum oxides*, Acta Chem. Scand. 13 (5), pp. 954–962, 1959.

[7] **Y. Bando, Y. Kato, T. Takada**, *Crystal growth of molybdenum oxides by chemical transport*, Kyoto Univ. 54 (5), pp. 330–334, 1976.

[8] **H. Gruber, E. Krautz**, *Untersuchungen der elektrischen Leitfähigkeit und des Magnetowiderstandes im System Molybdän-Sauerstoff*, Phys. Status Solidi A 62 (2), pp. 615–624, 1980. (in German)

[9] **J. Scarminio, A. Lourenço, A. Gorenstein**, *Electrochromism and photochromism in amorphous molybdenum oxide films*, Thin Solid Films 302, pp. 66–70, 1997.

[10] **T. He, J. Yao**, *Photochromism of molybdenum oxide*, J. Photochem. Photobiol. C Photochem. Rev. 4 (2), pp. 125–143, 2003.

[11] **D. Mutschaull, K. Holzner, E. Obermeier**, *Sputtered molybdenum oxide thin films for NH3 detection*, Sensors Actuators B Chem. 36 (1–3), pp. 320–324, 1996.

[12] **Y.-C. Tseng, A.U. Mane, J.W. Elam, S.B. Darling**, *Ultrathin molybdenum oxide anode buffer layer for organic photovoltaic cells formed using atomic layer deposition*, Sol. Energy Mater. Sol. Cells 99, pp. 235–239, 2012.

[13] **X. Hu, W. Zhang, X. Liu, Y. Mei, Y. Huang**, *Nanostructured Mo-based electrode materials for electrochemical energy storage*, Chem. Soc. Rev., 2015.

[14] **C. Battaglia, X. Yin, M. Zheng, I.D. Sharp, T.L. Chen, S. Mcdonell, C. Carraro, R. Maboudian, R.M. Wallace, A. Javey**, *Hole selective MoOx contact for silicon solar cells*, Nano Lett., 2014.

[15] **J. Bullock, D. Yan, A. Cuevas, Y. Wan, C. Samundsett**, *n- and p-type silicon solar cells with molybdenum oxide hole contacts*, Energy Procedia 77, pp. 446–450, 2015.

[16] **M. Vasilopoulou, L.C. Palilis, D.G. Georgiadou, P. Argitis, S. Kennou, L. Sygellou, I. Kostis, G. Papadimitropoulos, N. Konofaos, A.A. Iliadis, D. Davazoglou**, *Reduced molybdenum oxide as an efficient electron injection layer in polymer light-emitting diodes*, Appl. Phys. Lett. 98, pp. 123301, 2011.

[17] **B. Bessais, N. Mliki, R. Bennaceur**, *Technological, structural and morphological aspects of screen-printed ITO used in ITO/Si type structure*, Semicond. Sci. Technol. 8, pp. 116–121, 1993.

[18] **R.B.H. Tahar, T. Ban, Y. Ohya, Y. Takahashi**, *Tin doped indium oxide thin films: Electrical properties*, J. Appl. Phys. 83 (5), pp. 2631–2645, 1998.

[19] **K. Daoudi, B. Canut, M.G. Blanchin, C.S. Sandu, V.S. Teodorescu, J.A. Roger**, *Tin-doped indium oxide thin films deposited by sol-gel dip-coating technique*, Mater. Sci. Eng. C 21, pp. 313–317, 2002.

[20] **N.J. Arfsten**, *Sol-gel derived transparent IR-reflecting ITO semiconductor coatings and future applications*, J. Non. Cryst. Solids 63, pp. 243–249, 1984.

[21] **J. Kane, H.P. Schweizer**, *Chemical vapor deposition of transparent electrically conducting layers of indium oxide dopet with tin*, Thin Solid Films 29, pp. 155–163, 1975.

[22] **R.G. Gordon**, *Preparation and properties of transparent conductors*, Mat. Res. Soc. Symp. Proc. 426, pp. 419–429, 1996.

[23] **P.M. Martin**, *Handbook of Deposition Technologies for Films and Coatings*, Elsevier, Oxford, Burlington, 3rd ed., 2010.

[24] **R.P. Howson, I. Safi, G.W. Hall, N. Danson**, *Sputtering of indium-tin oxide*, Nucl. Instruments Methods Phys. Res. B 121, pp. 96–101, 1997.

[25] **D. Depla, S. Mahieu**, *Reactive Sputter Deposition*, Springer, Berlin, Heidelberg, New York, 2008.

[26] **R.A. Haefer**, *Oberflächen- und Dünnschicht-Technologie - Teil I Beschichtungen von Oberflächen*, Springer, Berlin, Heidelberg, 1987. (in German)

[27] **W. Westwood**, *Sputter Deposition*, AVS, New York, 2003.

[28] **L.L.Y. Chang, B. Phillips**, *Phase Relations in Refractory Metal-Oxygen Systems*, J. Am. Ceram. Soc. 52 (10), pp. 527–533, 1969.

[29] **C. Zhang, M.C. Gao, Y. Yang, F. Zhang**, *Thermodynamic modeling and first-principles calculations of the Mo–O system*, CALPHAD 45, pp. 178–187, 2014.

[30] **H. Okamoto**, *Phase Diagrams for Binary Alloys, Desk Handbook*, ASM International, 2000.

[31] **N. Schönberg**, *On the Existence of a Metallic Molybdenum Oxide*, Acta Chem. Scand. 8 (4), pp. 617–619, 1954.

[32] **T. Dutta**, *Nanostructured transparent conducting oxides for device applications*, Doctoral Thesis, North Carolina State University, USA, 2011.

[33] **A. Magnéli**, *Structure of the* ReO_3*-type with Recurrent Dislocations of Atoms: "Homologous Series" of Molybdenum and Tungsten Oxides*, Acta Cryst. 6, pp. 495, 1953.

[34] **P.F. Carcia, E.M. McCarron**, *Synthesis and Properties of Thin Film Polymorphs of Molybdenum Trioxide*, Thin Solid Films 155 (1), pp. 53–63, 1987.

[35] **G. Andersson, A. Magnéli**, *On the Crystal Structure of Molybdenum Trioxide*, Acta Chem. Scand. 4, pp. 793–797, 1950.

[36] **C.V. Ramana, V.V. Atuchin, V.G. Kesler, V. a. Kochubey, L.D. Pokrovsky, V. Shutthanandan, et al.**, *Growth and surface characterization of sputter-deposited molybdenum oxide thin films*, Appl. Surf. Sci. 253 (12), pp. 5368–5374, 2007.

[37] **P.A. Cox**, *Transition Metal Oxides - An Introduction to their Electronic Structure and Properties*, Clarendon Press, Oxford, 1992.

[38] **A. Blume**, *Synthese und strukturelle Untersuchungen von Molybdän-, Vanadium- und Wolframoxiden als Referenzverbindungen für die heterogene Katalyse*, Doctoral Thesis, Technische Universität Berlin, Germany, 2004. (in German)

[39] **T. Ekström, M. Nygren**, *Ternary Phases with the* Mo_5O_{14} *Type of Structure - I. A Study of the Molybdenum-Vanadium-Oxygen System*, Acta Chem. Scand. 26 (5), pp. 1827–1835, 1972.

[40] **O. Kubaschewski, E.L. Evans, C.B. Alcock**, *Metallurgical thermochemistry*, Pergamon Press, Oxford, 4th ed., 1967.

[41] **L. Kihlborg**, *Crystal structure studies on* Mo_5O_{14}*, A Compound Exhibiting Two-Dimensional Disorder*, Ark. För Kemi 21 (40), pp. 427–437, 1963.

[42] **Gmelin**, *Gmelin Handbuch der Anorganischen Chemie - Erg. Bd. B 1*, Springer, Berlin, Heidelberg, New York, 1975. (in German)

[43] **M.N. Rahaman**, *Ceramic Processing and Sintering*, Marcel Dekker, Inc., New York, 2nd ed., 2003.

[44] **R.L. Coble**, *Sintering Crystalline Solids. I. Intermediate and Final State Diffusion Models*, J. Appl. Phys. 32, 1961.

[45] **H. Salmang, H. Scholze**, *Keramik*, Springer, Berlin, Heidelberg, New York, 7th ed., pp. 313–380, 2007. (in German)

[46] **Z.A. Munir, U. Anselmi-Tamburini, M. Ohyanagi**, *The effect of electric field and pressure on the synthesis and consolidation of materials: A review of the spark plasma sintering method*, J. Mater. Sci. 41, pp. 763–777, 2006.

[47] **Z.A. Munir, D.V. Quach**, *Electric Current Activation of Sintering: A Review of the Pulsed Electric Current Sintering Process*, J. Am. Ceram. Soc. 94 (1), pp. 1–19, 2011.

[48] **J.E. Garay**, *Current-Activated, Pressure-Assisted Densification of Materials*, Annu. Rev. Mater. Res. 40, pp. 445–468, 2010.

[49] **R. Orrù, R. Licheri, A.M. Locci, A. Cincotti, G. Cao**, *Consolidation/synthesis of materials by electric current activated/assisted sintering*, Mater. Sci. Eng. R 63, pp. 127–287, 2009.

[50] **E.A. Olevsky, L. Froyen**, *Impact of Thermal Diffusion on Densification During SPS*, J. Am. Ceram. Soc. 92 (S1), pp. 122–132, 2009.

[51] **B. Ertug**, *Sintering Applications*, InTech, Rijeka, 2013.

[52] **W. Chen, U. Anselmi-Tamburini, J.E. Garay, J.R. Groza, Z.A. Munir**, *Fundamental investigation on the spark plasma sintering/synthesis process - I. Effect of dc pulsing on reactivity*, Mater. Sci. Eng. A 394, pp. 132–138, 2005.

[53] **O. Guillon, J. Gonzalez-Julian, B. Dargatz, T. Kessel, G. Schierning, J. Räthel, M. Herrmann**, *Field-Assisted Sintering Technology/ Spark Plasma Sintering: Mechanisms , Materials , and Technology Developments*, Adv. Eng. Mater. 16 (7), pp. 830–849, 2014.

[54] **K. Vanmeensel, A. Laptev, O. Van der Biest, J. Vleugels**, *The influence of percolation during pulsed electric current sintering of ZrO_2–TiN powder compacts with varying TiN content*, Acta Mater. 55, pp. 1801–1811, 2007.

[55] **S. Munoz, U. Anselmi-Tamburini**, *Temperature and stress fields evolution during spark plasma sintering processes*, J. Mater. Sci. 45, pp. 6528–6539, 2010.

[56] **T.B. Holland, U. Anselmi-Tamburini, D.V. Quach, T.B. Tran, A.K. Mukherjee**, *Effects of local Joule heating during the field assisted sintering of ionic ceramics*, J. Eur. Ceram. Soc. 32, pp. 3667–3674, 2012.

[57] **L.F. McHugh, P. Kumar, D. Meendering, R. Wu, G. Wotting, R. Nicholson**, *Method of making MoO_2 powders, products made from MoO_2 powders, deposition of MoO_2 thin films, and methods of using such materials*, US2006/0165572 A1, 2006.

[58] **D.M. Mattox**, *Handbook of physical vapor deposition (PVD) processing*, Noyes Publication, Westwood, NJ, 1st ed., 1998.

[59] **F. Rovere**, *Theoretical and experimental assessment of Cr-Al-Y-N as protective coating for γ-TiAl based alloys*, Doctoral Thesis, Rheinisch-Westfälische Technische Hochschule, Aachen, 2009.

[60] **M. Ohring**, *Materials Science of Thin Films*, Academic Press, San Diego, 2nd ed., 2002.

[61] **R. Parsons**, *Sputter Deposition Processes*, in: J.L. Vossen, W. Kern (Eds.), Thin Film Processes II, Academic Press, Inc., Boston, pp. 177–208, 1991.

[62] **J. Musil, P. Baroch, J. Vlcek, K.H. Nam, J.G. Han**, *Reactive magnetron sputtering of thin films: present status and trends*, Thin Solid Films 475, pp. 208–218, 2005.

[63] **M. Mühlbacher**, *High-resolution characterization of TiN diffusion barrier layers, Licentiate Thesis No. 1720*, Linköping University, 2015.

[64] **B.A. Movchan, A.V. Demchishin**, *Study of the structure and properties of thick vacuum condensates of Nickel, Titanium, Tungsten, Aluminium Oxide and Zirconium Dioxide*, Phys. Met. Met. 28 (4), pp. 83–90, 1969.

[65] **J.A. Thornton**, *Influence of apparatus geometry and deposition conditions on the structure and topography of thick sputtered coatings*, J. Vac. Sci. Technol. 11 (4), 1974.

[66] **P.B. Barna, M. Adamik**, *Fundamental structure forming phenomena of polycrystalline films and the structure zone models*, Thin Solid Films 317, pp. 27–33, 1998.

[67] **International Centre for Diffraction Data**, Card 00-042-1120 for bcc-Mo, Card 00-032-0671 for m-MoO_2, Card 01-089-6725 for o-Mo_4O_{11}, Card 00-012-0753 for tri-Mo_9O_{26}, and Card 00-076-1003 for o-MoO_3, 2007.

[68] **http://rruff.info**, October, 2015.

[69] **W. Schatt, K.P. Wieters, B. Kieback**, *Pulvermetallurgie*, Springer, Berlin, Heidelberg, 2nd ed., 2007. (in German)

[70] **H.C. Starck Inc.**, *Method of making MoO_2 Powders, Products made from MoO_2 Powders, Deposition of MoO_2 Thin Films, and Mehtods of using such Materials*, WO 2005/040044 A2, 2005.

[71] **H. Holleck**, *Material selection of hard coatings*, J. Vac. Sci. Technol. A 4 (6), pp. 2661–2669, 1986.

[72] **A. Fujishima, T.N. Rao, D.A. Tryk**, *Titanium dioxide photocatalysis*, J. Photochem. Photobiol. C Photochem. Rev. 1, pp. 1–21, 2000.

[73] **http://www.idealvac.com/files/manuals/Leybold-ITR90-Gauge-Specs-Data-Sheet01.pdf**, February, 2016.

[74] **Compact FullRangeTM Gauge Manual PKR 251**, Pfeiffer Vacuum, 2008.

[75] **C. Saringer, M. Tkadletz, C. Mitterer**, *Restrictions of stress measurements using the curvature method by thermally induced plastic deformation of silicon substrates*, Surf. Coatings Technol. 274, pp. 68–75, 2015.

[76] **G.G. Stoney**, *The tension of metallic films deposited by electrolysis*, Proc. R. Soc. London Series A, pp. 172–175, 1909.

[77] **W.D. Nix**, *Mechanical properties of thin films*, Metall. Trans. A 20 (11), pp. 2217–2245, 1989.

[78] **P.D. Desai, T.K. Chu, H.M. James, C.Y. Ho**, *Electrical resistivity of selected elements*, J. Phys. Chem. Ref. Data 13 (4), pp. 1069–1096, 1984.

[79] **S.H. Mohamed, S. Venkataraj**, *Thermal stability of amorphous molybdenum trioxide films prepared at different oxygen partial pressures by reactive DC magnetron sputtering*, Vacuum 81 (5), pp. 636–643, 2007.

[80] **T. Jörg, M.J. Cordill, R. Franz, O. Glushko, J. Winkler, C. Mitterer**, *The electro-mechanical behavior of sputter-deposited Mo thin films on flexible substrates*, Thin Solid Films 606, pp. 45–50, 2016.

[81] **MKS Baratron Type 627D Manual**, 2013.

[82] **L.J. van der Pauw**, *A method of measuring specific resistivity and Hall effect of discs of arbitrary shape*, Philips Res. Rep. 13, pp. 1–9, 1958.

[83] **W. Gruenert, A.Y. Stakheev, R. Feldhaus, K. Anders, E.S. Shpiro, K.M. Minachev**, *Analysis of Mo(3d) XPS spectra of supported Mo catalysts: An alternative approach*, J. Phys. Chem. 95 (3), pp. 1323–1328, 1991.

[84] **V. Bhosle, A. Tiwari, J. Narayan**, *Epitaxial growth and properties of MoO_x ($2<x<2.75$) films*, J. Appl. Phys. 97 (8), pp. 83539, 2005.

[85] **M. Rouhani, Y.L. Foo, J. Hobley, J. Pan, G.S. Subrammanian, X. Yu, et al.**, *Photochromism of amorphous molybdenum oxide films with different initial Mo^{5+} relative concentrations*, Appl. Surf. Sci. 273, pp. 150–158, 2013.

[86] **M.T. Greiner, L. Chai, M.G. Helander, W. Tang, Z. Lu**, *Transition metal oxide work functions: The influence of cation oxidation state and oxygen vacancies*, Adv. Funct. Mater., pp. 1–12, 2012.

[87] **M.C. Biesinger, B.P. Payne, L.W.M. Lau, R.S.C. Smart**, *X-ray photoelectron spectroscopic chemical state quantification of mixed nickel metal, oxide and hydroxide systems*, Surf. Interface Anal., pp. 324–332, 2009.

[88] **M.C. Biesinger, B.P. Payne, A.P. Grosvenor, L.W.M. Lau, A.R. Gerson, R.ST.C. Smart**, *Resolving surface chemical states in XPS analysis of first row transition metals, oxides and hydroxides: Cr, Mn, Fe, Co and Ni*, Appl. Surf. Sci. 257, pp. 2717–2730, 2011.

[89] **T. Goodman**, *Handbook of Visual Display Technology*, Springer, Berlin, Heidelberg, New York, 1st ed., 2012.

[90] **J.M. Pachlhofer, C. Jachs, R. Franz, E. Franzke, H. Köstenbauer, J. Winkler, C. Mitterer**, *Structure evolution in reactively sputtered molybdenum oxide thin films*, Vaccum 131, pp. 246–251, 2016.

[91] **S. Ray, R. Banerjee, N. Basu, A.K. Batabyal, A.K. Barua**, *Properties of tin doped indium oxide thin films prepared by magnetron sputtering*, J. Appl. Phys. 54 (6), pp. 3497–3501, 1983.

[92] **Y. Shigesato, S. Takaki, T. Haranou**, *Crystallinity and electrical properties of tin-doped indium oxide films deposited by DC magnetron sputtering*, Appl. Surf. Sci. 48/49, pp. 269–275, 1991.

[93] **S. Ishibashi, Y. Higuchi, Y. Ota, K. Nakamura**, *Low resistivity indium-tin oxide transparent conductive films. I. Effect of introducing H_2O gas or H_2 gas during direct current magnetron sputtering*, J. Vac. Sci. Technol. A 8 (3), pp. 1399–1402, 1990.

[94] **R. Kleinhempel, G. Kaune, M. Herrmann, H. Kupfer, W. Hoyer, F. Richter**, *Properties of ITO films prepared by reactive magnetron sputtering*, Microchim Acta 156, pp. 61–67, 2007.

[95] **T. Karasawa, Y. Miyata**, *Electrical and optical properties of indium tin oxide thin films deposited on unheated substrates by d. c. reactive sputtering*, Thin Solid Films, 223 pp. 135–139, 1993.

[96] **D.B. Fraser, H.D. Cook**, *Highly conductive, transparent films of sputtered $In_{2-x}Sn_xO_{3-y}$*, J. Electrochem. Soc. 119 (10), pp. 1368–1374, 1972.

[97] **A.G. Dirks, R.A.M. Wolters, A.J.M. Nellissen**, *On the microstructure-property relationship of W-Ti-(N) diffusion barriers*, Thin Solid Films 193–194, pp. 201–210, 1990.

[98] **S.M. Rossnagel, I. Yang, J.J. Cuomo**, *Compositional changes during magnetron sputtering of alloys*, Thin Solid Films 199, pp. 59–69, 1991.

[99] **D.B. Bergstrom, F. Tian, I. Petrov, J. Moser, J.E. Greene**, *Origin of compositional variations in sputterdeposited Ti x W1-x diffusion barrier layers*, Appl. Phys. Lett. 67, pp. 3102, 1995.

[100] **B.R. Rogers, T.S. Cale, Y.K. Chang**, *Simulation and experimental study of reemission during sputter deposition of Ti-W films*, J. Vac. Sci. Technol. A Vacuum, Surfaces, Film. 14, pp. 1142, 1996.

[101] **B.R. Rogers, C.J. Tracy, T.S. Cale**, *Compositional variation in sputtered Ti-W films due to reemission*, J. Vac. Sci. Technol. B 12, pp. 2980, 1994.

[102] **H. Ramarotafika, G. Lemperiere**, *Influence of a d.c. substrate bias on the resistivity, composition, crystallite size and microstrain of WTi and WTi-N films*, Thin Solid Films 266, pp. 267–273, 1995.

[103] **L.B. Jonsson, C. Hedlund, I.V. Katardjiev, S. Berg**, *Compositional variations of sputter deposited Ti/W barrier layers on substrates with pronounced surface topography*, Thin Solid Films 348, pp. 227–232, 1999.

[104] **L.R. Shaginyan, M. Mišina, S. Kadlec, L. Jastrabı, A. Macková, V. Peřina**, *Mechanism of the film composition formation during magnetron sputtering of WTi*, J. Vac. Sci. Technol. A Vacuum, Surfaces, Film 19, pp. 2554, 2001.

[105] **Y. Murakami, T. Shingyoji**, *Compositional difference between films and targets in sputtering of refractory metal silicides*, J. Vac. Sci. Technol. A Vacuum, Surfaces, Film 8, pp. 851, 1990.

[106] **T. Yamazaki, N. Ikda, H. Tawara, M. Sato**, *Investigation of composition uniformity of $MoSi_x$ sputtering films based on measurement of angular distribution of sputtered atoms*, Thin Solid Films 235, pp. 71–75, 1993.

[107] **J. Willer, S. Pompl, D. Ristow**, *Sputter-deposited WB_x films*, Thin Solid Films 188, pp. 157–163, 1990.

[108] **R.A. Simao, A.K. Costa, C.A. Achete, S.S. Camargo Jr.**, *Magnetron sputtering SiC films investigated by AFM*, Thin Solid Films 377–378, pp. 490–494, 2000.

[109] **M.Y. Liao, Y. Gotoh, H. Tsuji, J. Ishikawa**, *Compound-target sputtering for niobium carbide thin-film deposition*, J. Vac. Sci. Technol. B 22, pp. L24, 2004.

[110] **F. Kunc, J. Musil, P.H. Mayrhofer, C. Mitterer**, *Low-stress superhard Ti-B films prepared by magnetron sputtering*, Surf. Coatings Technol. 174–175, pp. 744–753, 2003.

[111] **C. Mitterer**, *Borides in Thin Film Technology*, J. Solid State Chem. 133, pp. 279–291, 1997.

[112] **J. Neidhardt, S. Mráz, J.M. Schneider, E. Strub, W. Bohne, B. Liedke, W. Möller, C. Mitterer**, *Experiment and simulation of the compositional evolution of Ti–B thin films deposited by sputtering of a compound target*, J. Appl. Phys. 104 (63304), 2008.

[113] **H. Köstenbauer, D. Lorenz, J. Winkler, W. Theiss**, *Optimization of Molybdenum Oxides for Low-Reflectance Thin Films using Numerical Simulation*, SID DIGEST, pp. 1741–1743, 2015.

[114] **H. Köstenbauer, D. Lorenz, J. Winkler, B. Tseng, G. Jakopic**, *Molybdenum Oxides for Low-Reflectance Thin Films in Touch Applications*, IDMC Proceedings (PH-01), 2013.

[115] **V.M. Aroutiounian, K. Martirosyan, P. Soukiassian**, *Low reflectance of diamond-like carbon/porous silicon double layer antireflection coating for silicon solar cells*, J. Phys. D. Appl. Phys. 37, pp. L25–L28, 2004.

11 LIST OF PUBLICATIONS

“Thermal stability of MoO_2 and MoO_3 powders”

Julia M. Pachlhofer, Robert Franz, Enrico Franzke, Jörg Winkler, Christian Mitterer; *Unpublished due to confidential issues*

“Structure evolution in reactively sputtered molybdenum oxide thin films”

Julia M. Pachlhofer, Christoph Jachs, Robert Franz, Enrico Franzke, Harald Köstenbauer, Jörg Winkler, Christian Mitterer; *Vacuum 131 (2016) 246-251*.

“Industrial-scale sputter deposition of MoO_x thin films: microstructure evolution and properties”

Julia M. Pachlhofer, Aitana Tarazaga Martín-Luengo, Robert Franz, Enrico Franzke, Harald Köstenbauer, Jörg Winkler, Alberta Bonanni, Christian Mitterer; *Accepted for JVSTA*

“Non-reactive dc magnetron sputter deposition of MoO_x thin films from ceramic molybdenum oxide targets”

Julia M. Pachlhofer, Aitana Tarazaga Martín-Luengo, Robert Franz, Enrico Franzke, Harald Köstenbauer, Jörg Winkler, Alberta Bonanni, Christian Mitterer; *In Final Preparation*